NOTE TO USERS

University of Alberta

ANALYSIS OF NON-STATIONARY SURFACE AIR TEMPERATURE AND A DROUGHT INDEX

by

Tingting Shu

A thesis submitted to the Faculty of Graduate Studies and Research
in partial fulfillment of the requirements for the degree of

Doctor of Philosophy
in
Applied Mathematics

Department of Mathematical & Statistical Sciences

Edmonton, Alberta
Fall, 2007

Your file Votre référence
ISBN: 978-0-494-33066-1
Our file Notre référence
ISBN: 978-0-494-33066-1

Dedication

This thesis is dedicated to my parents

Abstract

In this thesis, advanced techniques developed in time series analysis and econometrics are used to derive new results on climatic change detection.

The empirical mode decomposition (EMD) is used to obtain non-stationary annual cycles (NAC) from daily and monthly surface air temperature data (SAT). The NAC is a better filter for the annual cycle than the thirty-year-mean annual cycle (TAC). The strength of the EMD annual cycles at the ten selected stations in North America increases with the latitude of the station's location because of the variation in receiving the energy from solar radiation, and is weak for stations near the ocean because of the effect of the heat capacity of the large water body.

The local trigonometric function is a compact representation for the NAC from daily SATs. The climate change is found not only in the mean temperature, but also in the amplitude and phase of the NAC. The climatic noises driving the anomaly of NAC are shown to be anti-persistent for time scales of over three months. This result indicates the possible presence of negative feedback from the earth's climate system.

The dynamic factor analysis approach is applied to investigate the source of climate change directly from the observed annual and seasonal SAT data in the contiguous United States over the period 1900-2003. A strong inter-decadal oscillation related to the inter-decadal scale of the North Atlantic oscillation is obtained in the winter and summer seasonal data. A stochastic trend related to anthropogenically-induced change is obtained after the inter-decadal oscillations are removed. The results show that the warming observed during the first part of the twentieth century had different origins in different parts of the US region.

The area integrated standardized precipitation index (ASPI) is used to quantify the rainfall deficiency in the Southern Africa region. The temporal and spatial patterns of ASPI and the gridded drought magnitudes show that both short-term and long-term droughts have intensified and rainfall deficits at all time scales have increased considerably after 1980, contributing to the widespread famines in the region. The areas most vulnerable to droughts are identified.

Acknowledgement

This thesis is a result of my research during my Ph.D. study. Many people helped me during my pursuit of the Ph.D. degree. My supervisor, Professor Samuel S.P. Shen, provided academic guidance, encouragement, and financial support during my study and research. I am deeply grateful to his generosity, patience, and understanding in guiding me through all the difficulties and hard times. He is a mentor in not only academics but also life. We learned to be devoted, responsible, and appreciative person from him. I would like to express my gratitude to Dr. Hee-seok Oh who was my co-supervisor for a year. He helped me understand data mining using statistical method and supported me to visit Geophysical Statistics Project in the National Center for Atmospheric Research (NCAR) in Boulder, Colorado, where I met a group of enthusiastic scientists and broadened my horizon. Dr. Douglas Nychka of NCAR, Zhaohua Wu of Center for Ocean-Land-Atmoshphere Studies, and Norden E. Huang of NASA provided insightful guidance and thoughts about Hilbert-Huang method. Dr. Davison Mwale of the Civil Engineering department in the University of Alberta shared ideas and enthusiasm of research and collaborated in some researches. I am also grateful to Dr. Bruce Sutherland who never hesitates to encourage me throughout the writing of the thesis and took time to revise it.

I would like to give my heartfelt thanks to my father and late mother whom I wish could live to see my graduation. A special thanks goes to my husband, Dr. Yunfei Chen, who always hold my hands in times of joy and sorrow.

Table of Contents

List of Tables

List of Figures

List of Acronyms

AIC	Akaike information criterion
AR	Autoregressive
ARIMA	Autoregressive integrated moving average
ASPI	Area integrated Standardized Precipitation index
BIC	Bayesian information criterion
DFA	Detrended fluctuation analysis
EMD	Empirical mode decomposition
ENSO	El Niño-Southern oscillation
EOF	Empirical orthogonal function
GDCN	Global Daily Climatology Network
GFDL	Geophysical Fluid Dynamics Laboratory
GHCN	Global Historical Climatology Network
HHT	Hilbert-Huang transform
HP	Hodrick-Prescott
HT	Hilbert transform
IMF	Intrinsic mode function
NAC	Non-stationary annual cycle
NCEP	National Centers for Environmental Prediction
PC	Principal component
PDI	Palmer drought index
SAT	Surface air temperature data
SD	Standard deviation

SPI	Standardized Precipitation index
SST	Sea surface temperature
TAC	Thirty-year-mean annual cycle
WT	Wavelet transform

Chapter 1
Introduction

During the past century changes in various climate variables have been observed, among which the temperature and precipitation changes affect natural and human systems directly. The detection and attribution of climatic change in global scale observed annual surface air temperature data has achieved great success in the past decade. Folland et al. (2001) concluded, "The best estimate of global surface temperature change is a 0.6°C increase since the late 19th century with a 95% confidence interval of 0.4 to 0.8°C" based on the linear trend in the average global SATs (see p. 101). Mitchell et al. (2001) showed that natural forcings might have contributed to the observed warming in the first half of the 20th century, while the warming over the last 50 years is mainly due to anthropogenic greenhouse gases. Folland et al. (2001) pointed out that although the global trend in the severe drought statistics was small for 1900 to 1995, increases occurred in dry areas in southern Africa.

Most of the previous studies of climate change are based on temperature data at monthly, annual or longer temporal scales (Folland et al., 2001; Mitchell et al., 2001). However, the nonlinear and non-stationary nature of climate processes call for the use of climate data at short time scales, such as a daily scale. The Global Daily Climatology Network (GDCN) version 1 temperature dataset was released in July 2002. This dataset

breaks new ground in the global climate database. No consistent global daily dataset existed prior to the GDCN. Compared to annual data, daily temperature data contains much richer dynamic climate properties, but includes much more noise from the local environment. The study on the daily temperature data calls for a new data-processing and analyzing methodology. This motivated the study in this thesis.

The statistical detection of trends has been confined to the average global or hemispheric time series, or the averages at large latitude belts. To incorporate spatial patterns of climate responses to the anthropogenical and natural forcings, climate model simulations are used. Although the current climate models provide satisfactory simulations over large scales, the climate simulations at subcontinental and regional scales vary greatly from model to model.

Global climate changes have caused many regional adverse natural consequences, including drought. The persistent drought in Africa in the last half-century has attracted great scientific attention. For most of this region, food productivity depends on the intra-seasonal variability of rainfall. The predominant crop in this region is maize, whose high water demand makes southern Africa particularly vulnerable to the changes in inter-annual and intra-seasonal rainfall. Drought monitoring in Africa is of particular importance in mitigating climate risks in agricultural production. The spatially integrated information is important in explaining the dynamical links between the African drought and global circulation. This issue motivated the study of an integrated probabilistic index for monitoring the African drought.

This thesis focused on the aforementioned three topics, which includes the statistical analysis of the non-stationary properties of daily temperature data, a data-driven method for assessing climate changes in the contiguous U.S. region, and the analysis of rainfall deficits and droughts over southern Africa by using an area integrated standardized precipitation index.

1.1 Non-stationary annual cycle and empirical mode decomposition

Conventionally, surface temperature data are modeled as a fixed annual cycle over all years plus the deviation from this cycle. The annual cycle of climate data describes the climate's expected regular oscillation from the winter cold to the summer heat and back to the winter cold. When studying monthly and daily observations, this cycle is treated as fixed from year to year. However, due to the rapid change in the climate in the last century, we speculate that the annual cycle may have been altered and that the statistical properties of the residual from a fixed annual cycle may be significantly different from those of the varying annual cycle. The rapid climate change in the last 150 years indicates that the climate process at an observational station or over a region is not a fixed annual cycle plus a stationary anomaly (i.e., a departure); rather it is a varying annual cycle plus a new anomaly which is closer to be stationary than the conventionally defined anomaly. Therefore, this non-stationary annual cycle becomes a fundamental problem in climate research.

Although the concept has not been used in climate research, the time-evolving cycle

in data has been used in the study of econometric time series (Harvey, 1985, and 1989). Macroeconometric time series such as those for common stock prices exhibit cyclical fluctuations. Band-pass filters from the frequency domain are often used to isolate the fluctuations from the slow-varying components. The use of the Hodrick-Prescott (HP) low-pass filter is a popular trend-extraction technique. The HP filter is the solution for the minimization of the variation in the cycle component penalized by the acceleration of the long-term trend component. A number of trend-cycle decomposition techniques popular in the study of econometric time series were used to decompose the annual mean Northern Hemispheric average SAT anomaly time series into a trend and a cycle (Mills, 2006). The results showed that the low-pass filters did not adapt to data well.

We apply the newly developed empirical mode decomposition (EMD) method to the daily SATs (Huang et al., 1998, 1999, and 2003). The EMD method has been successfully used in many analyses of non-stationary and nonlinear data, ranging from extracting the solar cycle signal from stratospheric data, to examining the volatility in the market (Coughlin and Tung, 2004; Huang et al., 2003; Loh et al., 2001; Xu et al., 2004). The various applications for data processing in different areas show that the EMD method is adaptive to data and highly efficient at identifying embedded structures.

In our applications, the EMD method is applied to the observed daily SATs at ten selected stations in North America from the GDCN dataset. The non-stationary annual cycle (NAC) can be separated as an intrinsic mode function generated in the EMD sifting process. The NAC has a mean period equal to a year, and the amplitude varies from year

to year. Both the Hilbert and Fourier spectra of the NAC are examined to validate the power density at the frequency of a cycle per year. The Hilbert and Fourier spectra of the NAC and the residual from NAC are examined. The EMD method is also applied to the Niño 3.4 sea surface temperature to extract the NAC.

1.2 Statistical analysis of daily SAT data

Climate change detection has been focused mainly on the annual or monthly mean temperature data. To test the significance of a trend in the climate data, a popular model in the statistical analysis approach is the linear trend model:

$$y_t = \beta_0 + \beta_1 t + u_t,\ t = 1,2,\cdots T.$$

The linear trend represents the systematic change in the climate time series, whereas the residual u_t represents the natural variability. A simple model for u_t is the ARMA model. The fractionally integrated model (Bloomfield and Nychka, 1992; Fomby and Vogelsang, 2002; Gil-Alana, 2003) and the non-stationary model (Zhen and Basher, 1999) for natural variability have also been used to detect linear trends in annual SATs.

Due to the high temporal resolution, the daily SATs contain rich information about the dynamics of the climate for time scales ranging from days to decades, and can be used to discern the energy exchange between large and small spatial scales due to nonlinear dynamic climate processes. The strong dependence of the daily temperature in consecutive days is common sense. Large-scale circulation can affect the temperature for years. The anthropogenically forced change may alter the pattern of the annual cycle.

Extracting the fixed annual cycle may produce spurious long-range dependence (Lewis and Ray, 1997). The periodic variation of the variance, i.e., the heteroskedasticity property, of the noise in the daily temperature data has been noted by Campell and Diebold (2005). The long-range dependence or anti-persistency property of the temperature time series is related to the positive or negative feedback from the Earth's climate system (Kärner, 2002). For this purpose, the detrended fluctuation analysis (DFA) has been shown to be an excellent tool to provide indicators of dependency and the degree of stationarity (Hu et al., 2001).

While the EMD NAC generates a pleasingly smooth, non-stationary annual cycle, the parametric method has the advantage of providing plausible physical explanations. Although the annual cycle is not strictly sinusoidal, the trigonometric function gives a compact description of the NAC through the time-varying phase and amplitude. In this thesis, we model the NAC by using the piecewise trigonometric functions of with periods of 365 and 365/2 days. The amplitude and phase of the piecewise trigonometric functions vary from year to year. Thus, it can be determined whether the climate change affects the NAC's amplitude or phase. The statistical property of the anomaly from the non-stationary annual cycle can be explored by using DFA. Through such analysis, we can identify at which time scale the climate change signal affects the temperature data.

1.3 Stochastic trends in surface temperature data in the contiguous US region

Recent studies on climate change detection have focused on two main topics: the statistical time series for assessing climate changes and the optimal detection for identifying climate change signals in data and thus attributing the cause of the change. Using the time series approach, Folland et al. (2001) noted that the changes in the average global surface temperature occurred mainly in two periods, from about 1910 to 1945, and from 1976 to the present, and that the warming rate in the second period has been higher than that in the first period, indicating that the climate change has not been constant over time. Nonlinear trend, in the form of parametric (Zhen and Basher, 1999; Mills, 2006) or non-parametric trends (Harvey and Mills, 2003; Craigmile, et al., 2004; Mills, 2006), has also been used in a number of studies. However, due to its univariate nature, the time series method has limited applications in the attribution of regional climate change, forecasting, and policy-making.

The optimal detection approach is the main approach used in detecting and attributing climate change. The multivariate regression method has been adapted for climate change detection and attribution (Mitchell et al. 2001; North and Wu, 1995). This method uses the model-simulated climate responses to the external forcings as regressors. This approach accounts for the spatial as well as the temporal variations. The simulations of the global mean annual SAT response to anthropogenic forcings and the natural

forcings with a coupled ocean-atmosphere climate model agree with the observed data and the climate warming in the last 50 years is likely due to greenhouse gases (Mitchell et al., 2001).

Since then, the optimal fingerprinting approach has been applied to the detection and attribution of climate change on continental scales (Stott, 2003; Zwiers and Zhang, 2003). Model-simulated climate noise and climate responses to the external forcings have also been used in climate change detection and attribution in some regional climate indices (Karoly, et al., 2003; Karoly and Braganza, 2005; Karoly and Wu, 2005). However, the model-simulated climate noise and climate change signals in sub-continental and regional scales should be used cautiously. Mitchell (2001) pointed out that the control simulations before 2001 were only long enough to estimate the internal variability over the global scale. Giorgi et al. (2001) noted that the Atmosphere-Ocean General Circulation Models display highly variable bias from region to region and among models at the regional scale. Karoly et al. (2003) noticed that the time series of the low-pass filtered ensemble mean temperature anomaly in North American from model runs do not agree with the observed warming from 1900-1949. Knutson et al. (2006) also found discrepancies in the historical climate simulations of the Geophysical Fluid Dynamics Laboratory (GFDL) global climate models and the observed temperature data in the southeast United States region. Therefore, in the sub-continental to regional scale climate change attribution, it is desirable to use an approach that discriminates between the anthropogenically forced signal and the naturally forced signal without the aid of climate models.

To explore the source of the climate changes in the contiguous United States region over the twentieth century, we need to identify the signals associated with different spatial-temporal patterns, which distinguish the sources of climate change from the observed data (Folland et al., 2001). To date, this topic has not been sufficiently studied. Schneider and Held (2001) are the only researchers who have attempted to study in this direction. They isolated a spatial-temporal pattern over the 20^{th} century, which is similar to the model-simulated greenhouse gas and sulphate aerosol fingerprints in the January and July surface temperatures. However, all other patterns they obtained were unstable and depended on the parameters of the algorithm.

Stock and Watson (1988) proposed the principal components approach to extract stationary common factors in large-scale dynamic factor analysis. This approach was shown to be applicable to the non-stationary factors as well (Bai, 2004). The dynamic analysis of large cross-sections aims to decompose the variables into common components and a purely sectoral component. This approach provides relatively few indexes to model the long-term co-movement of many variables and to synthesize information in a large-dimension factor model. The resulting indices can be used to construct the forecasts of the time series. The estimated dynamic factors have been shown to be consistent, and the forecasts based on the small number of indexes are asymptotically efficient (Stock and Watson, 1999, and 2002; Bai, 2004; Bai and Ng, 2004).

In our study, the principal components approach is used to investigate the long-term

climate change in the contiguous United States over the period 1900-2003. The gridded Global Historical Climatology Network annual and seasonal surface temperature data are used in this study. Due to the large local variations, the grid box data are first preprocessed by using a structural model. Then dynamic factor analysis is applied to the resulting stochastic trend to generate the major non-stationary factors and the associated spatial patterns. The nature of the non-stationary factors is analyzed through their spatial and temporal properties. The advantage of this approach is that it is robust to parameter perturbations in estimating the stochastic trends and to the change of the grids. As well, this analysis involves only observed data.

1.4 Standardized precipitation index analysis in Africa

The famines from 1990-2005 in the southern Africa region were disastrous and threatened millions of people. Although the atmospheric variations cannot be altered, monitoring the rainfall variability is important so that adaptations can be made in planting crops. The standardized precipitation index (SPI) (McKee et al., 1993) has been successfully used in various parts of the world to monitor droughts.

In this thesis, the area integrated standardized precipitation index (ASPI) is used to quantify the rainfall deficiency and to identify the areas most vulnerable to droughts. The threshold rainfall and the rainfall deficit are defined to provide a direct interpretation of the drought facts. The temporal and spatial patterns of the ASPI and the empirical orthogonal functions of gridded drought magnitudes are also studied to learn the effects

of the short-term and long-term droughts. The results also identify the areas in this region that are most vulnerable to droughts. The incremental adaptation of agriculture practices such as changes in crops or crop varieties is recommended for those areas.

1.5 Thesis outline

This thesis is structured as follows. Chapter 2 uses the EMD method to extract the non-stationary annual cycle. The detailed sifting algorithm is presented. The properties of the NACs of daily temperature data and their residues over ten stations are examined.

In Chapter 3, the NAC is modeled by non-stationary trigonometric fitting and compared to the NAC generated by the EMD method. The climate change associated with the NAC is analyzed. The statistical properties of the residue from this NAC are also studied.

Chapter 4 studies the climate change in the contiguous US region by using factor analysis. This method does not depend on the model-simulated climate change signal and extracts the signals and the associated spatial patterns from the observed data.

Chapter 5 quantifies the rainfall deficiency and identifies the areas most vulnerable to droughts in the southern Africa region by using the area integrated standardized precipitation index (ASPI).

Chapter 6 presents the conclusions, summarizes the major results, and lists suggestions for future studies.

Chapter 2

HHT Analysis of the Non-stationary Annual Cycle of Daily Surface Air Temperature Data

2.1 Introduction

Conventionally, when studying climate change by using surface air temperature (SAT) data, one analyzes the anomaly data, which are the departures of the observed SAT from its normal value, called the "climate normal" or "climatology." The climatology of a station is often defined as the thirty-year mean of the station's data for each month. The 30-year period progresses as time passes. Currently, 1961-1990 is commonly used as the climatology period, whereas 1951-1980 was used in the 1980s and the early 1990s. Thus, the January climatology is the simple mean of the January temperatures from 1961-1990. This climatology from January to December is the expected monthly temperature throughout a year and is the so-called "annual cycle", or "seasonal cycle." Thus, the annual cycle of the climate data describes the expected climate's regular oscillation from the winter cold to the summer heat and back to the winter cold. This fixed cycle, marked by the spring, summer, fall, and winter seasons, reflects the relative positions between the sun and the Earth, the heat capacity of the Earth's surface (land or ocean), and some topographic characteristics. The commonly

used thirty-year-mean annual cycle, referred to as the TAC hereafter, has a temporal resolution of a month. The thirty-year mean of the SAT of a fixed day in a year, say October 6, can be very different from each other when one considers the 30-year means of 1951-1980 and 1961-1990. Thus, when the 30-year-mean approach is used for calculations, an annual cycle of daily resolution is not normally considered. The monthly TAC also varies when using different periods of 30 years, but the variation is much smaller compared to that of the daily TAC.

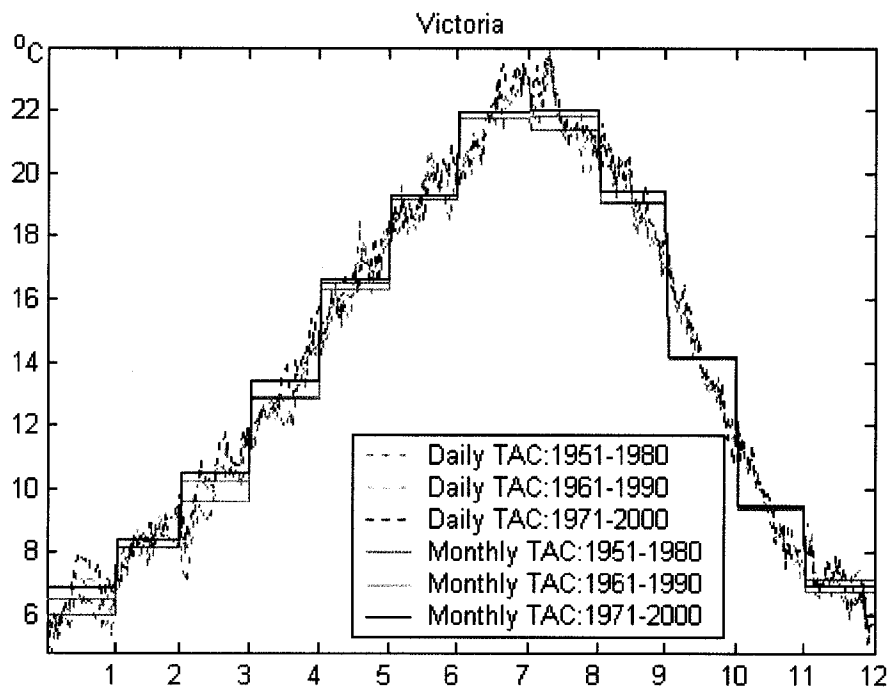

Figure 2.1. Daily and monthly TAC derived from the daily maximum surface air temperature data at the Victoria station, Canada.

Figure 2.1 shows the daily and monthly TAC of the maximum daily surface air temperature of the Victoria station, Canada. The results were calculated by using three different climatology periods: 1951-1980, 1961-1990, and 1971-2000. The figure clearly indicates a large variation of the daily climatology and a relatively smaller variation of the monthly climatology. However, the variation of the monthly climatology is still noticeable, particularly in the months of January, March and April.

Among the periodic or quasi-periodic signals of climate, the annual cycle is often the strongest one in the temporal climate data, particularly for the SAT and precipitation in the mid- or high-latitudes. This fact can be intuitively understood but may not be always easy to quantify. The Fourier spectrum of a station's data for the SAT shows a distinctive peak at a cycle per year (Figure 2.2(b)). The other peaks, such as those at the bi-annual and interannual cycles, are several orders smaller than that of the annual cycle in Victoria, Canada. However, due to the motions of the atmosphere and ocean, the annual cycle is far from being this simple. The TAC definition of monthly annual cycle has become a standard way to derive climate anomalies in climate data processing, but the daily climatology is not well defined in terms of the 30-year-mean. Nonetheless, the daily resolution data are useful in assessing climatic change due to the nonlinear interaction in the Earth's climate system. This interaction can result in energy transfer from high frequency oscillations (daily oscillations) to low frequency oscillations (inter-decadal oscillations). Thus, the daily anomalies should be considered similar to those in climate modeling studies. To obtain the daily anomalies, one has to use a well-defined

climatology. Due to the large variations of the 30-year-mean of the daily data and the step-function behavior of the monthly TAC, alternative methods are required to define the daily climatology, or, in general, to define the climatology at the resolution of a given data set, whether daily, weekly or monthly. Time-frequency analysis is the right tool for this purpose. Thus, the window-Fourier-transform, the wavelet analysis, and the Hilbert-Huang transform (HHT) can be used. The empirical mode decomposition (EMD) in the HHT procedure can lead to an intrinsic mode function that has a mean period of a year and carries some nonlinear and non-stationary signals of a climate system (Gloersen and Huang, 2003). In this chapter, the nonlinear and non-stationary annual cycle, referred to as the NAC, is analyzed in both time and frequency domains, and it is compared with the TAC whenever appropriate.

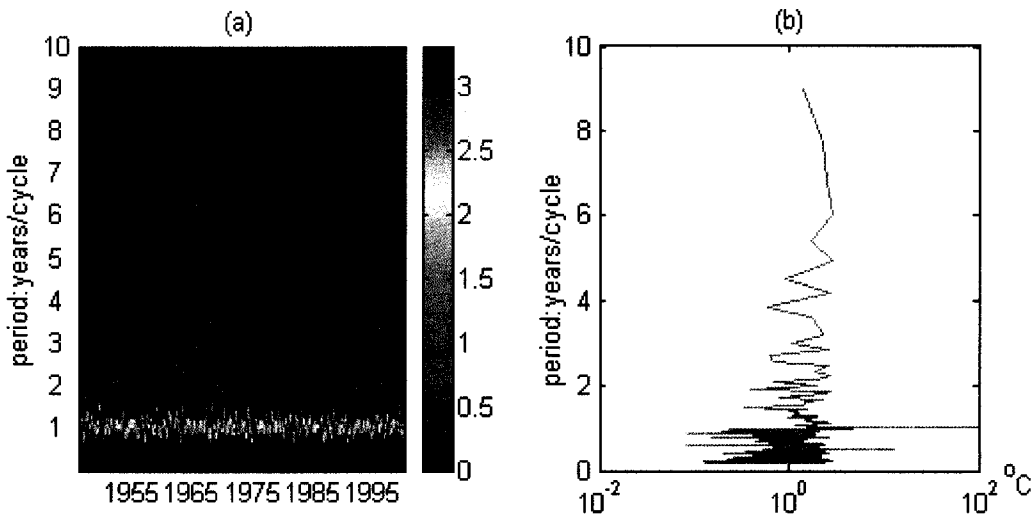

Figure 2.2. (a) Hilbert spectrum of the monthly maximum SAT data at the Victoria station, Canada. The unit of the color scales is [°C]. (b) Fourier spectrum of the same data.

In a TAC, the nonlinear interactions of different components of a climate system are largely ignored, and the anomalies derived from the TAC climatology still contain some apparent signal of the annual cycle. In other words, the TAC cannot completely filter out the annual signal from the climate data. Due to the nonlinear nature of the climate system, the spectral power of the climate data minus the TAC is not monotonic at the one cycle per year, but is distributed in a frequency interval containing the annual cycle of one cycle per year. Thus, when the annual cycle in the residue of data minus the TAC is strong, the calculations of the linear trends of the seasonal or monthly climate changes can be affected because the non-monotonic "annual cycles" in the anomaly data are not synchronized to have peaks and valleys at the same month or season. Thus, the anomalies with respect to the TAC can lead to much uncertainty in a linear trend that is being used to measure the local, monthly climatic changes.

In contrast, the NAC reflects not only the periodic variation of the solar irradiance but also the nonlinear and non-stationary processes of atmospheric motions. Since the NAC is obtained through a sifting process, the sum of the last a few intrinsic mode functions (IMF) can be regarded as the nonlinear and non-stationary trend. The nonlinear trend assessment of the monthly local climatic changes is more robust and useful for attribution studies of climatic changes.

Why do we want to remove the annual cycle? Although removing it is not important to the linear trend when a data stream is sufficiently long, the removal of this cycle becomes necessary when the data stream is shorter than 30 or 20 years. For a short

stream of data, if we want to get a long-term linear trend for the regional or global average SAT, the seasonal variation will influence the trend because only the departures from the "climate normal" in a cold area, such as Alberta, and a hot area, such as Arizona, can be compared in the spatial average. The annual cycle defined by the TAC assumes that the climate system can settle down into a "normal" pattern in a sufficiently long time period, say, 30 years. This assumption is a good approximation for many applications, yet when nonlinearity and non-stationarity have to be carefully considered, the assumption becomes problematic, since even in a low dynamic nonlinear chaotic system, such as the Lorenz attractor, the signal will not ever repeat itself. When the annual cycle is believed to be an intrinsic property of a climate system, an adaptive approach, rather than a priori functional method, needs to be used to find the annual cycle. Furthermore, a successful removal-operation of annual cycles should satisfy the following criteria: (i) the anomaly data should have no spectral power peaks around the period of a year, and (ii) the annual cycle should carry some physically meaningful signal, such as El Niño. Criterion (i) reflects the variation of the solar irradiance, and criterion (ii) reflects some major interactions between the dynamic components of a climate system driven by the solar heating. The conventionally defined annual cycle, the TAC, which is appropriate for a linear system, cannot even satisfy the criterion (i), much less (ii). We chose to use the EMD approach to extract the non-stationary annual cycle, i.e., the NAC. However, the NAC suffers from uncertainties due to different sifting parameters, while the TAC suffers from uncertainties due to different periods of 30 years.

T his chapter is organized as follows. Section 2.2 describes the EMD method used in this research, including the end-point conditions, spectral representation, intermittence test, and stopping criterion. Section 2.3 describes the daily and monthly data used in the analysis. Section 2.4 conducts the time analysis of the NAC and analyzes the NAC's robustness with respect to the length of the data stream, sifting parameters, and end-point algorithms. Section 2.5 performs the frequency analysis for both the NAC and the TAC. Section 2.6 contains conclusions and discussions.

2.2 Analysis method and computational algorithms

The analysis method used here follows mainly that of Huang et al. (1998), referred to as H98 hereafter, which is a time domain analysis using the EMD, and a frequency domain analysis using the Hilbert and Fourier spectra. However, both the time and frequency analyses of Huang et al. (1998, 1999, and 2003) are flexible in the computing details. Thus, we will specify our computing details to help readers repeat our results.

The key problem in time-frequency analysis is to find the instantaneous frequency of a time series. Several ways are available to find the instantaneous frequency, including the wavelet transform (WT) and Hilbert transform (HT) (Mallat, 1998; Boashash, 1992a). The popular WT spectrum does not have a good resolution for nonlinear processes and, hence, cannot effectively discern the nonlinear signals. The EMD pre-processed signals allow high-resolution Hilbert-spectra even for nonlinear signals. However, the HT often cannot be directly applied to a time series. For example, the HT was applied to the

analysis of the nonlinear vibration motions (Feldman, 1997), but the instantaneous frequency could not be found from the original time series. The possible problems were with the phase functions, which were non-differentiable, or had unbounded derivatives, or were non-physical. H98 showed examples of these. The problem, thus, becomes how to find a differentiable and physically meaningful phase function so that the instantaneous frequencies are well defined, and their implications can be explained for the system where the data come from. Huang and his colleagues established their empirical mode decomposition-Hilbert spectral analysis (EMD-HSA), i.e., the HHT, based upon the belief that a physically meaningful mode should be self-coherent, namely, either quasi-periodic and quasi-symmetric, or quasi-monotonic. Mathematically, phase functions and their derivatives can be defined for these types of functions by using the Hilbert transform (HT). The quasi-periodic and quasi-symmetric functions, or quasi-monotonic functions are the IMFs, which satisfy the following two conditions:

(i) In the temporal domain of data, the number of extrema and the number of zero-crossings must either be equal or differ at most by one.

(ii) At any point, the mean value of the envelope defined by the local maxima and the envelope defined by the local minima is zero.

With these requirements, the IMF oscillates in a narrow frequency band, a reflection of quasi-periodicity and nonlinearity. Of course, the non-constant frequency means non-stationarity. When an IMF $c(t)$ is found, its HT, $H\{c(t)\}$, can be defined as follows:

$$H\{c\} = \int_{-\infty}^{\infty} \frac{1}{\pi(t-\tau)} c(\tau) d\tau .$$

Then

$$c(t) + iH\{c(t)\} = a[t]\exp[i\omega(t)]$$

is well defined for a given t. This equation yields a frequency $\omega(t)$ and an amplitude $a(t)$. The triplet (t, ω, a) forms the Hilbert spectral power described in Huang et al. (1998). The procedures for finding an IMF $c(t)$ can be found in Huang (2005). However, the conditions of the end points, stopping criterion and intermittence are still flexible up to certain subjective decisions. The details of our algorithm are described as follows.

The envelopes of local maxima and minima require the extrapolation of the original time series outside the two temporal end points: the first point and the last point of the time series. However, usually no physical laws can be easily used to make the extrapolation. Various spline extrapolation methods have been developed. We used two extrapolation methods to deal with the end effect: the signal extension approach developed by Wu and Huang (2004) and the extrema-prediction approach. The signal-extension approach includes two steps: the signal extension step and the signal-damping step. In the first step, the targeted time series f_i, $i = 1, \cdots, N$ is extended by using the anti-symmetric extension at both ends with respect to the first and the last data points. In the second step, the extended signal is damped to the running mean or the fitted trends by using a polynomial fit towards both ends at linear rates. One can also use a one-step signal extension approach: a simple reflection extension. As well, many other signal-

extension methods can be used. The physical nature of a problem is helpful in determining which methods are appropriate for the problem.

The extrema-prediction approach predicts the two extrema before the first and after the last extrema at each of the iterations in the IMF calculation. The extended extrema are calculated by using the mirror image of the data about the first and last extrema. Assume the first data point is $(0, x_0)$, and the first two extrema are (t_1, x_1) and (t_2, x_2), where $0<t_1<t_2$. The predicted extrema are $t_{p1} = \min(0, 2t_1 - t_2)$, $x_{p1} = x_2$ if $2t_1 - t_2 < 0$; otherwise, $x_{p1} = x_0$, and $t_{p2} = t_{p1} - (t_2 - t_1)$, $x_{p2} = x_1$. The predicted extrema on the last-data-point side are determined similarly. Again, infinitely many extrema-prediction approaches can be used, and the nature of a problem helps to choose which ones are appropriate. For example, Coughlin and Tung (2004) extended the signal by adding a characteristic wave at each end of the sifted data stream.

The stopping criterion determining when the EMD sifting stops for an IMF mode is another important component for the sifting process. A stopping criterion through the standard deviation (SD) is proposed in H98. The sifting process for an IMF is stopped if this SD value is between 0.2 and 0.3. However, this SD value depends on the length of the time series. An alternative stopping criterion is that the number of zero crossings and extrema remains the same for N successive sifting steps (Huang et al., 1999, 2003). The choice of N is subjective, and many trials have to be made to find the best N suitable for a certain time series. The stopping criterion used here is that the sifting process stops when

$$SD = \frac{\sum_{i=1}^{N} m_i^2}{\sum_{i=1}^{N} h_i^2} < 0.00001,$$

where $\{h_i\}_{i=1,\cdots,N}$ are the data of the step of being stopped, and $\{m_i\}_{i=1,\cdots,N}$ are the mean of the envelope of maxima and that of the mimima of the data $\{h_i\}_{i=1,\cdots,N}$.

Mode mixture, a phenomenon involving different time scales mixed in a single IMF component, often occurs in a practical sifting process. The intermittency test is used to separate the intrinsic mode in the sifting process to prevent the modes from mixing. The intermittence criterion adopted in this study is the number *M* selected as the limit to the distances between each pair of the three successive maxima. If these distances are both greater than *M*, the points between the two zero crossings among the three extrema are assigned as zero. The value of *M* ranges between 120 and 150 for the station SAT anomaly data in this research.

Our HT is computed by using the Fourier transform (Marple, 1999). The signal $x(t)$ and its HT form an analytic signal $z(t) = x(t) + iHT\{x(t)\}$. The *N*-point Hilbert spectrum $Z(m)$ of the discrete analytic signal $z(t)$ is computed by

$$Z(m) = \begin{cases} 2X(m), & \text{for } 0 < m < \dfrac{N}{2} \\ X(m), & \text{for m} = 0, \dfrac{\text{N}}{2} \\ 0, & \text{for } \dfrac{\text{N}}{2} < \text{m} < \text{N} \end{cases},$$

where $X(m)$ is the Fourier transform of $x(t)$. The discrete-time analytic signal $z[n]$ is then computed by using the N-point inverse discrete transform from $Z(m)$, and the imaginary part of $z[n]$ is $HT\{x(t)\}$.

The amplitude and phase of $z(t)$ are, respectively,

$$a(t) = \left[x^2(t) + HT^2\{x(t)\}\right]^{1/2} \text{ and } \theta(t) = \arctan\left(\frac{HT\{x(t)\}}{x(t)}\right).$$

The instantaneous frequency of a continuous signal $x(t)$ is defined as (Boashash, 1992a)

$$\omega(t) = \frac{1}{2\pi}\frac{d\theta(t)}{dt}.$$

Computationally, for the discrete-time analytic signal $z[n]$, we can compute the amplitude $a[n]$ and the angle $\theta[n]$. The discrete-time instantaneous frequency $\omega[n]$ is computed by using the central difference scheme

$$\omega[n] = \frac{1}{2\pi}\frac{\theta[n+1]-\theta[n-1]}{2T},$$

where T is the time interval (Boashash, 1992b). Thus, a given time n corresponds to a frequency $\omega[n]$ and an amplitude $a[n]$. On the (n,ω) plane, each point corresponds to an amplitude that is a function of both time n and frequency ω. But the time and frequency are not independent; rather, they are related by a function $\omega[n]$. The triplet $(n,\omega[n],a[n])$ determines a point in the three-dimensional space (n,ω,a). For a given n, one can find a point $\omega[n]$, hence a point on the (n,ω) plane. From this point, one can then find the corresponding amplitude $a[n]$. Also one can find this $a[n]$ for all IMFs and hence for many amplitudes on the (n,ω) plane. These amplitudes form the discrete Hilbert-spectra. They are then smoothed by a 9-point-grid moving-average on the (n,ω) plane to yield a

series of smooth ridges in the three-dimensional space (n,ω,a) , and each ridge corresponds to an IMF. See Figures 2. 2(a) and 2.4(b) for two examples of Hilbert spectra. For more examples, see Huang et al. (1998).

2.3 Data

The dataset used in this study is the daily maximum surface air temperature data at 10 land stations of different latitude in USA and Canada in the time interval between January 1, 1946 and December 31, 2000. The data are from the Global Daily Climatology Network (GDCN) dataset of the US National Climatic Data Center (NCDC). The GDCN (v1.0), released in 2002, is a global data set and contains different records of 32857 locations around the world but covers mainly the northern hemisphere. The earliest and the latest dates of observation are March 1, 1840 and November 30, 2001, respectively, and most stations have missing records. All of the GDCN data have gone through an extensive set of quality-control procedures by using simple datum checks and the statistical analysis of sets of observations to locate and identify potential outliers and/or erroneous data. However, the station data have not been homogenized. To demonstrate the NAC properties, we selected 10 stations in the United States and Canada that have few missing data and are distributed at four different latitude levels and from the coast to inland. Among the ten stations, three are distributed around the latitude zone 32.47° N, three around 41.15° N, three around 48.65° N, and one on 62.47° N. Among these stations, San Diego, Medford, and Victoria are close to the Pacific. They have few

missing data in the 55 years from January 1, 1946 to December 31, 2000. Since the number of missing data is small compared to the length of the entire data, the missing data are interpolated by using cubic spline fitting. The inventory of the ten stations is shown in Table 2.1.

Table 2.1. Inventory of the ten stations used in this study.

Station name	Location	Number of missing data
Roscoe, Texas	32.45°N, 100.53°W	38
Shreveport, Louisiana	32.47°N, 93.82°W	1
San Diego, California	32.73°N, 117.17°W	43
Elko, Nevada	40.83°N, 115.78°W	7
Cheyenne, Wyoming	41.15°N, 104.8°W	4
Medford, Oregon	42.38°N, 122.87°W	12
Priest River, Idaho	48.35°N, 116.83°W	3
Victoria, B.C.	48.65°N, 123.43°W	4
Regina, Saskatchewan	50.43°N, 104.67°W	2
Yellowknife, NWT	62.47°N, 114.43°W	7

The land stations at different latitudes were chosen to show the increase of the strength of the annual cycle as the latitude gets higher. It is also important to determine the annual cycle for the equatorial area where the incoming solar irradiance does not vary according to seasons. While no clear annual cycle is apparent on the equator, the climatology and climate anomalies are routinely computed for the sea surface temperature (SST) data in both climate research and forecasting. To investigate the annual cycle of the equatorial area, we processed the SST data, not the SST anomaly data, over the Niño 3.4 region (5° N-5° S, 120° -170° W) from January 1950 to March 2003. The data were from the National Centers for Environmental Prediction (NCEP)

data repository. The El Niño and La Niña events defined by Trenberth (1997) were used to compare the El Niño-Southern oscillation (ENSO) signal carried by the NAC.

2.4 Time analysis

2.4.1 Examples of TAC and NAC

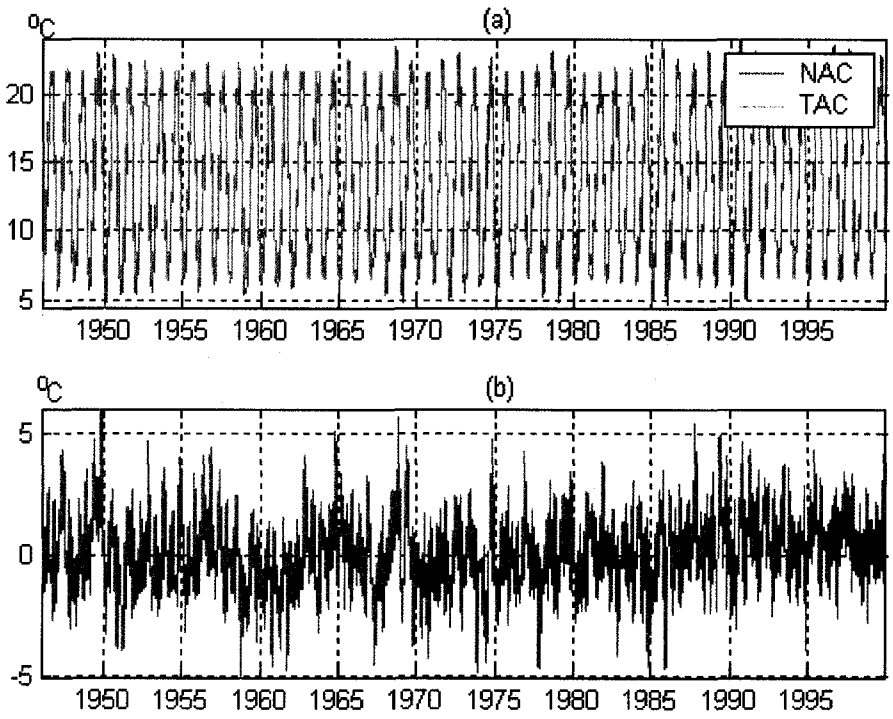

Figure 2.3. (a) NAC (blue) and TAC (red) cycles of the Victoria station, Canada, and (b) the difference between the NAC and TAC.

Figure 2.3 shows an example of the NAC and TAC of the daily maximum temperature of the Victoria station. The time resolution for Figure 2.3(a) is in months. The NAC was originally in the daily resolution, but was converted into the monthly

resolution by taking the monthly means. The TAC is a strictly periodic cycle, and the NAC is quasi-periodic, varying in both amplitude and period. The NAC is automatically synchronized with the TAC by using the EMD method. Their highs and lows appear at the same time. The result is quite surprising since the EMD itself does not force a specific period.

The amplitudes of the NAC's and TAC's highs and lows are different, causing the difference between the NAC and TAC. The magnitude of the difference can be as large as 5 degrees, but no apparent drift of the differences away from zero occurs.

The IMFs of the Niño 3.4 data are shown in Figure 2.4. The first IMF is the NAC, and the second IMF corresponds to the biennial cycle. The third to fifth IMFs are the three- to seven-year cycles. The sixth IMF is the decadal cycle. The seventh IMF is the multi-decadal cycle. The last one is a warming trend. The strength of the NAC was found to have been enhanced during three strong La Niña events in 1955-1956, 1970-1971, and 1974-1975, and weakened during most El Niño events before 1990. Similar results have been found by using the wavelet transform (Wang, 1994; Wang and Wang, 1996). The influence of the ENSO on the annual cycle appears to have changed after 1990. The prolonged El Niño events from 1991 to 1995 did not change the amplitude of the NAC, but the NAC still appeared to be strong during the latest La Niña period from 1998 to 2000. The smaller amplitude of the NAC in the second panel of Figure 2.4(a) corresponds to the smaller amplitude of the lowest smoothed bright line around the frequency of 1 cycle/year in Figure 2.4(b).

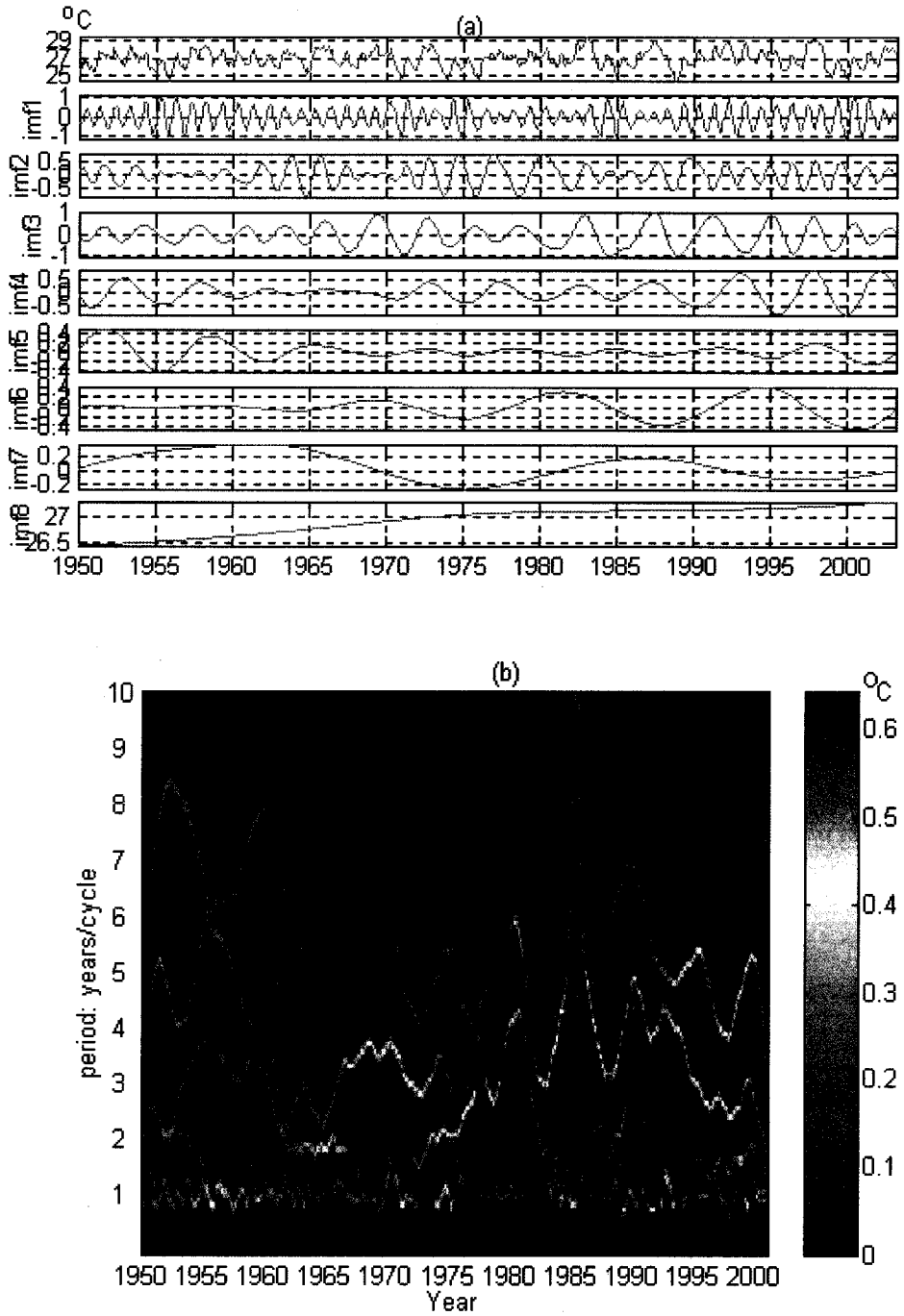

Figure 2.4. (a) The Niño 3.4 data and their IMFs. The first panel is the Niño 3.4 SST data, the second panel is the NAC, and the others are the higher IMFs. (b) Hilbert spectrum of the Niño 3.4 data according to all the IMFs.

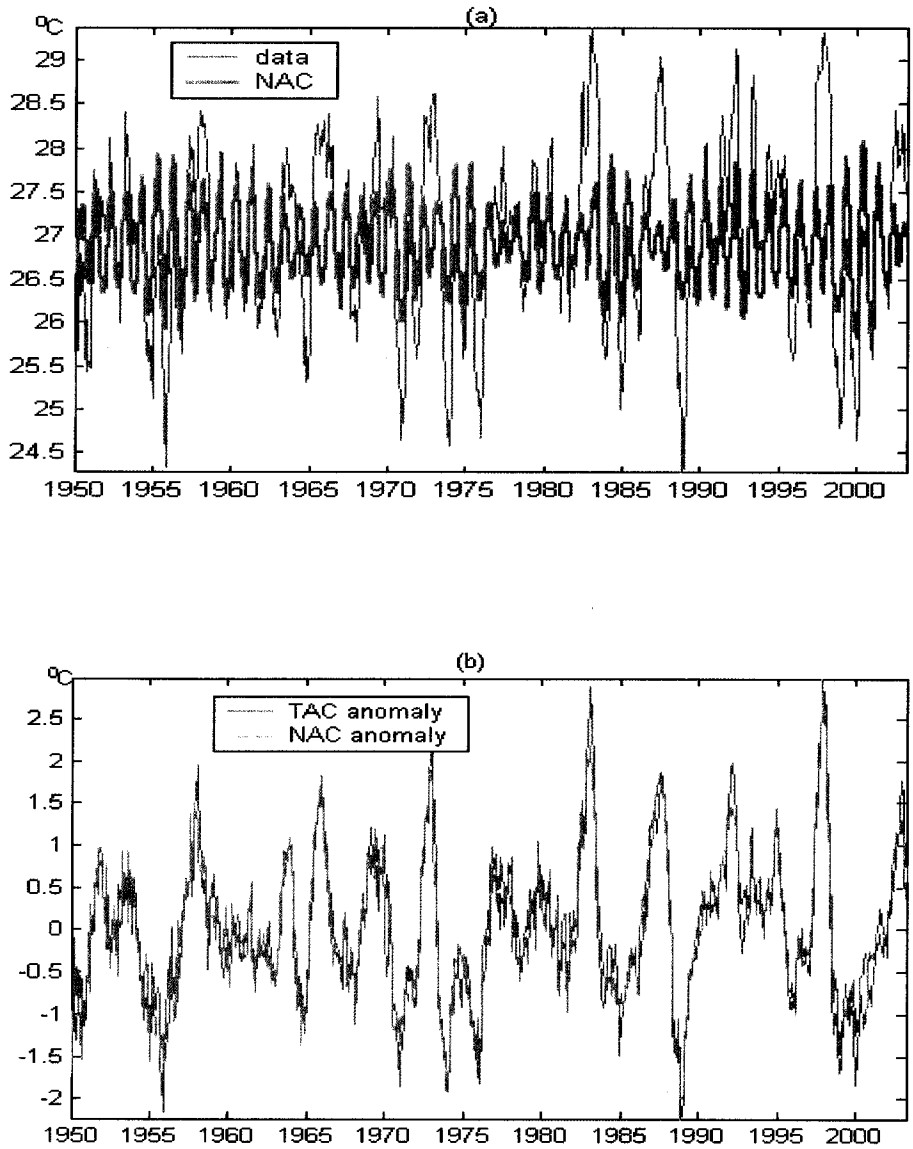

Figure 2.5 (a) The Niño 3.4 SST data (blue) and the NAC (red line). Here, the mean of the Niño 3.4 SST data is added to the NAC to compare it with the Niño 3.4 SST data. (b) The anomaly of the TAC (blue) and that of the NAC (red). Here, the mean of the Niño 3.4 SST data is subtracted from the NAC anomaly to compare it with the TAC anomaly.

To provide a clear illustration of the Niño 3.4 SST data, its NAC, and the anomalies from the NAC and TAC anomalies, we display them in Figure 2.5. It is quite surprising that the EMD-derived NAC is quasi-periodic and oscillates in the frequency of 1 cycle/year, because the incoming solar radiation does not have an apparent annual cycle. Of course, the NAC's amplitude is small with a high-low difference within 2 degrees. We also calculated the TAC and the anomalies with respect to the NAC and TAC. The anomalies are almost the same. The TAC anomalies have been commonly used to define El Niño events (Trenberth, 1997). The comparison of the NAC and TAC anomalies seems to suggest that the NAC anomalies can also be used to define El Niño events. If so, the definition of the El Niño events is more natural and the nonlinearity of the ENSO dynamics is explicitly reflected in the statistical computing of the ENSO index. However, this conclusion needs further justification, and the EMD method for describing the ENSO dynamics requires a more thorough investigation.

2.4.2 Temporal resolution of data

The NAC is in an annual time scale and is expected to be independent of the daily or monthly data resolution. This expectation is confirmed by analyzing the daily and monthly data of the ten stations. We have performed sifting processing on the daily and monthly SAT data. The resulting daily NAC is averaged in each month, and the difference between the mean daily NAC and the monthly NAC is small. Figure 2.6(a) shows the IMFs derived from the daily maximal temperature of the Victoria station. The

imf11 is the NAC, which is compared with the NAC derived from the monthly data (imf1 in Figure 2.6(b)). The difference, shown in Figure 2.6(c), oscillates around zero and has no apparent drift to the positive or negative side. Occasionally, the magnitude of the difference reaches 2 degrees. This large difference may be caused by some abnormal nonlinear interaction of the climate components. However, the exact cause is yet to be understood.

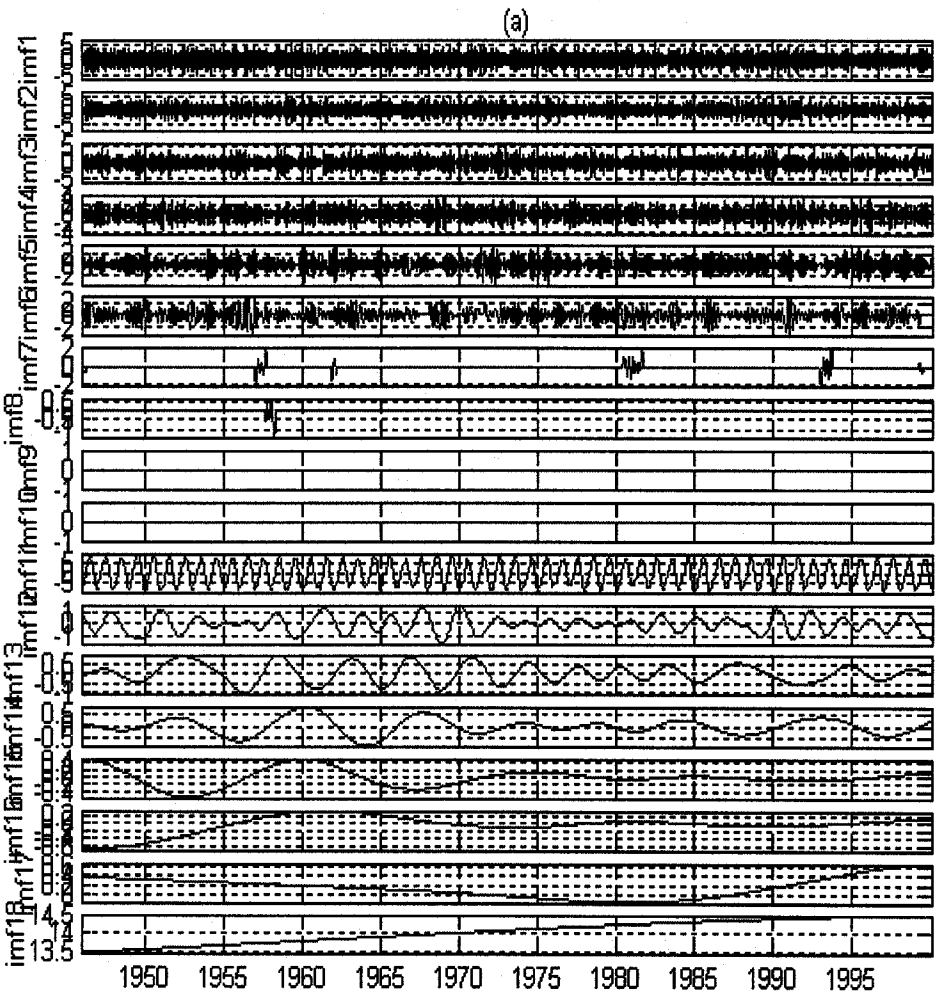

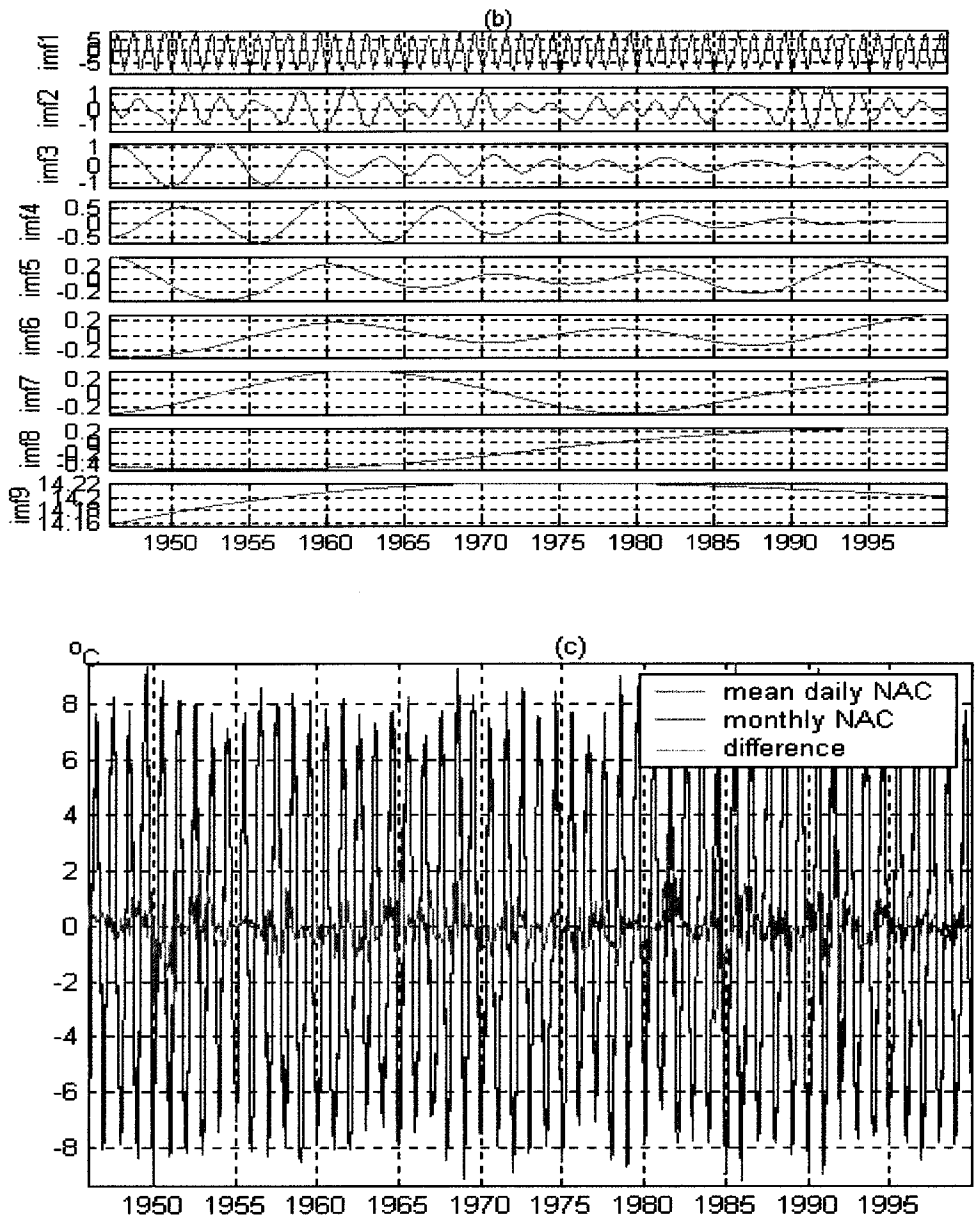

Figure 2.6. (a) IMFs from Victoria station obtained by using the daily data, (b) IMFs from Victoria station obtained by using the monthly data, and (c) the monthly mean NAC from the daily data (blue line), the NAC from the monthly data (green line), and the difference (red line) of the mean NAC from the daily data and the NAC from the monthly data.

The above result does not mean that the daily resolution data are not important. On the contrary, they are very important in reflecting the nonlinear interactions of the climate components in different time scales, but the interactions are reflected in the anomalies derived from the NAC.

2.4.3 Robustness of the EMD method

Another important aspect concerning our confidence in the NAC results is the robustness of the IMFs. Two questions are involved: (i) can the EMD lead to the separation of a given signal in a dataset, and (ii) are the EMD-derived IMFs insensitive to the length of data streams, perturbation of the end conditions, intermittency test, and stopping criterion. Huang et al. (2003) addressed some aspect of this problem. More examples are given below.

2.4.3.1 EMD separation of a known signal in a synthetic dataset

A dataset of 7,300 ($=365\times 20$) data points, uniformly spaced in time t, has three signal components and a noise component and is expressed by the following formula:

$$s[n]=-5\cos\left(\frac{2\pi n}{365}\right)+\cos\left(\frac{2\pi n}{365\times 5}\right)+(0.000001\times n)^2+0.0001\times n+w[n],$$

where $\{w[n]\}$ is a sequence of white noise with mean zero and variance $\sigma_w^{\,2}=1.5^2$, and $n=1,\cdots,365\times 20$ (Figure 2.7(a)). The dataset mimics 20 years, excluding February 29 in a leap year, of climate data of two periodic components at the frequency of 1 cycle/year and 1/5 cycles/year, a quadratic trend, and a white noise. The annual cycle is much

stronger than the five-year cycle. The nonlinear trend is very weak. This signal is contaminated by white noise $\{w[n]\}$. The signal extension approach was applied to mitigate the end effect. The sifting results show the IMFs representing dyadically-filtered white noise (Flandrin et al., 2004; Wu and Huang, 2004), the annual cycle component, and the low-frequency components, and the last two IMFs are trends (Figure 2.7(b)). We used the sum of the low-frequency components to reconstruct the five-year-cycle component in the signal and the sum of the last two IMFs to reconstruct the trend component. The results show, as expected, that the EMD can accurately recover the strong annual component. The recovery of the weak 5-year cycle is also very good except in the neighborhood of the end points. The end-point effects are carried to the trend recovery The EMD-derived trends from 0 to 2,300 and from 4,500 to 7,300 are apparently deviating from the original trend (see Figure 2.7(c)). These results call for further revisions on the end point conditions.

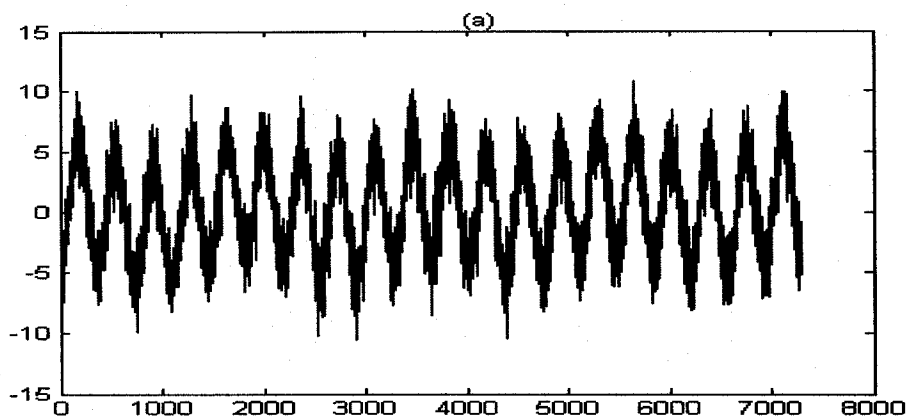

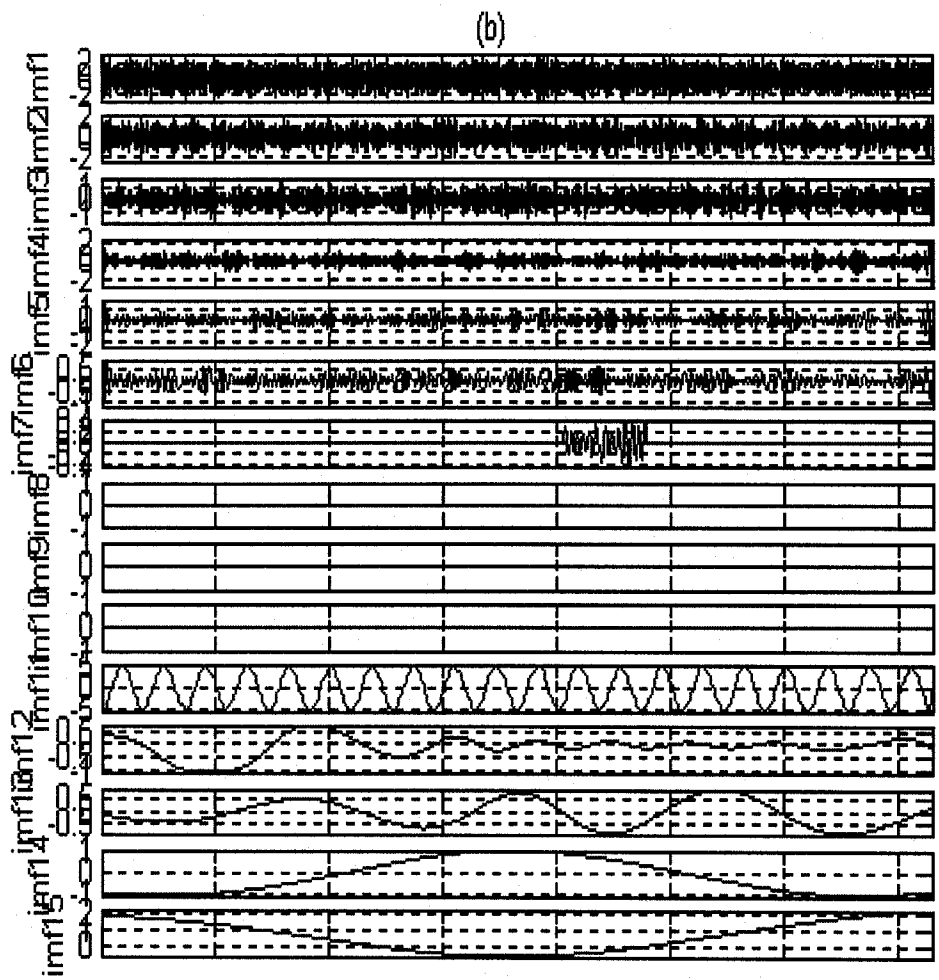

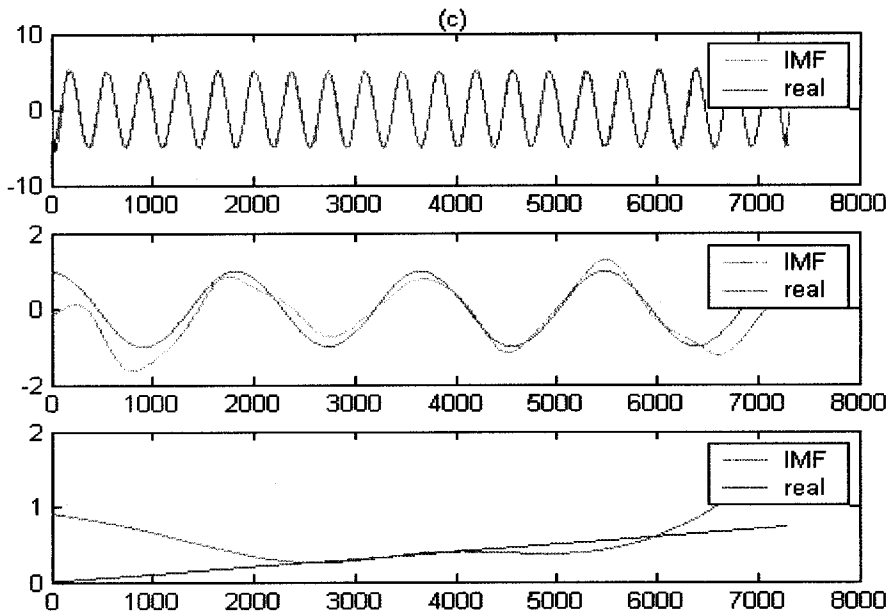

Figure 2.7. (a) Synthesized data $s[n]$. (b) IMFs of $s[n]$ from the sifting process. (c) Comparisons of the IMFs with the three signal components.

2.4.3.2 Robustness with respect to data length

The full dataset of the daily maximum temperature data at Victoria station are from January 1, 1946 to December 31, 2000. In order to test the IMF's robustness with respect to the data length, we took a partial set of the data from January 1, 1946 to December 31, 1999 and calculated the IMFs. The NACs derived from the full dataset and the partial dataset are basically the same (Figure 2.8).

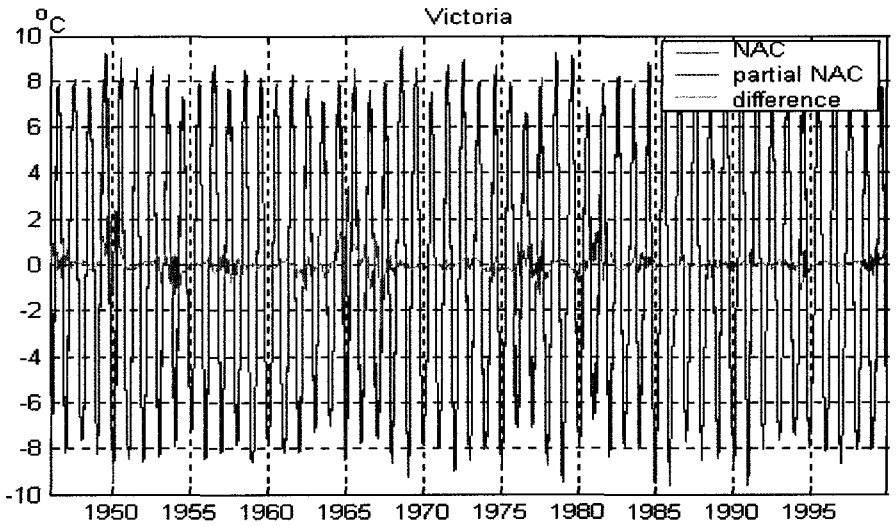

Figure 2.8. The NAC of the daily maximum SAT from January 1, 1946 to December 31, 2000 (blue line), and that of the SAT from January 1, 1946 to December 31, 1999 at the Victoria Station (green line), and the difference between the two NACs (red line).

2.4.3.3 Robustness with respect to end conditions

We used three end conditions in the EMD method: the signal extension approach using anti-symmetric extension, the signal extension approach using reflection extension, and the extrema-prediction approach. The results shown in Figure 2.9 imply that the NAC does not change much with respect to end point conditions, and, hence, that the NAC is robust with respect to these end-condition perturbations. Of course, the end conditions have to be reasonable. One can expect very different NACs if the end conditions are arbitrarily set.

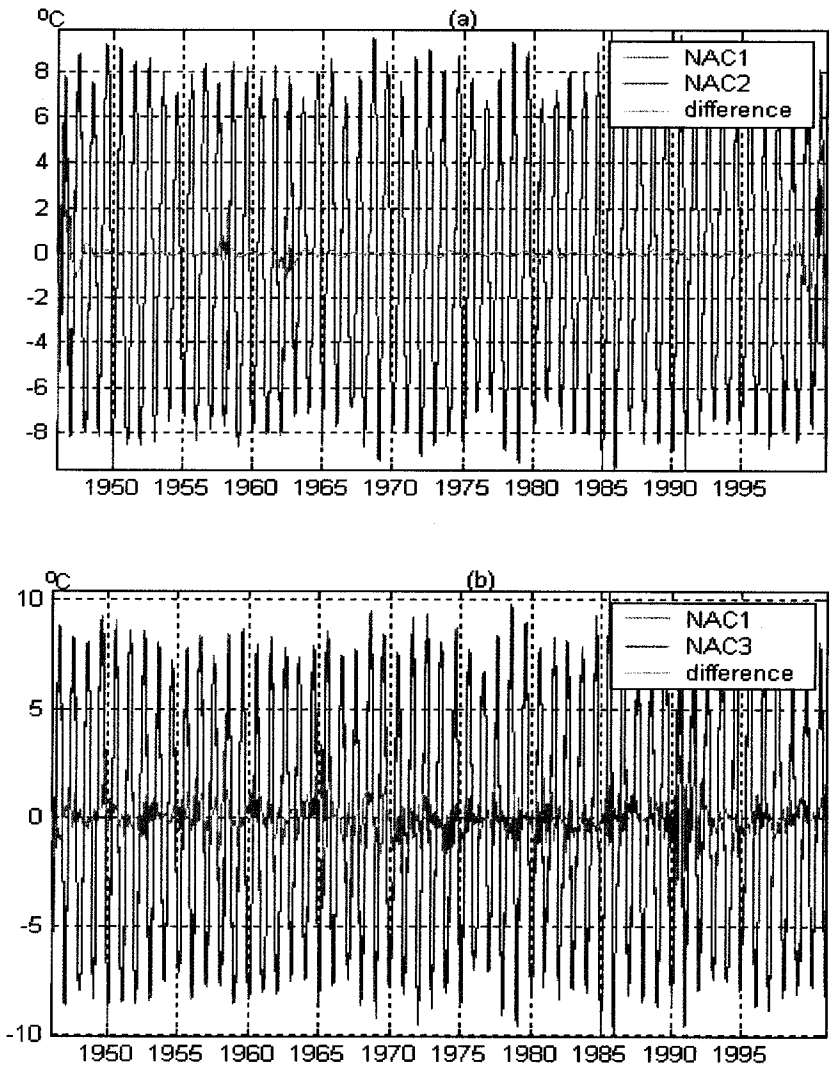

Figure 2.9. (a) The NAC from the signal extension approach by using the reflection extension as end conditions (blue line), the NAC from the signal extension approach by using anti-symmetric extension (green line), and their difference (red line). (b) The NAC from the signal extension approach by using reflection extension (blue line), the NAC from the extrema-prediction approach (green line), and their difference (red line).

2.5 Frequency analysis

2.5.1 Hilbert Spectra of NAC

After performing the sifting process and intermittency test, the NAC was obtained for each station's data series. The NAC for the daily maximum temperature contains no mode mixture. The intermittency parameter M is 150 -180 days in the sifting process of the daily temperature of the ten stations. The daily data have high-frequency oscillations before the NAC IMF. After the NAC IMF, the remaining IMFs manifest the biennial cycle with periods from 1.5 to 2.5 years, the inter-annual cycle with periods from 4 to 6 years, the decadal cycle with periods from 7 to 10 years, the multi-decadal cycle with a period greater than 15 years, and a trend, respectively.

To assess the effect of solar radiation and the heat capacity of the Earth's surface materials on the strength of the NAC, the marginal Hilbert spectra (i.e., the temporal integration of the Hilbert spectra) for the data of the ten stations are compared in four groups: three groups of stations located at the similar latitudes but with variable distances from large water bodies, and one group of stations located at inlands and very different latitudes (Figure 2.10). The results in Figure 2.10 indicate the following. First, at the same latitude, the NAC strengths are comparable, but the San Diego station, Medford station, and Victoria station have less NAC spectrum power than the other stations located at about the same latitude (Figures 2.10 (a)-(c)). This finding reflects the effect of the heat capacity of the large water bodies: the larger the heat capacity, the weaker the annual cycle. Second, at different latitudes, the NAC's strength increases with latitude

(Figure 2.10(d)) because the higher the latitudes of the stations, the larger the seasonal variation in receiving the energy from solar radiation.

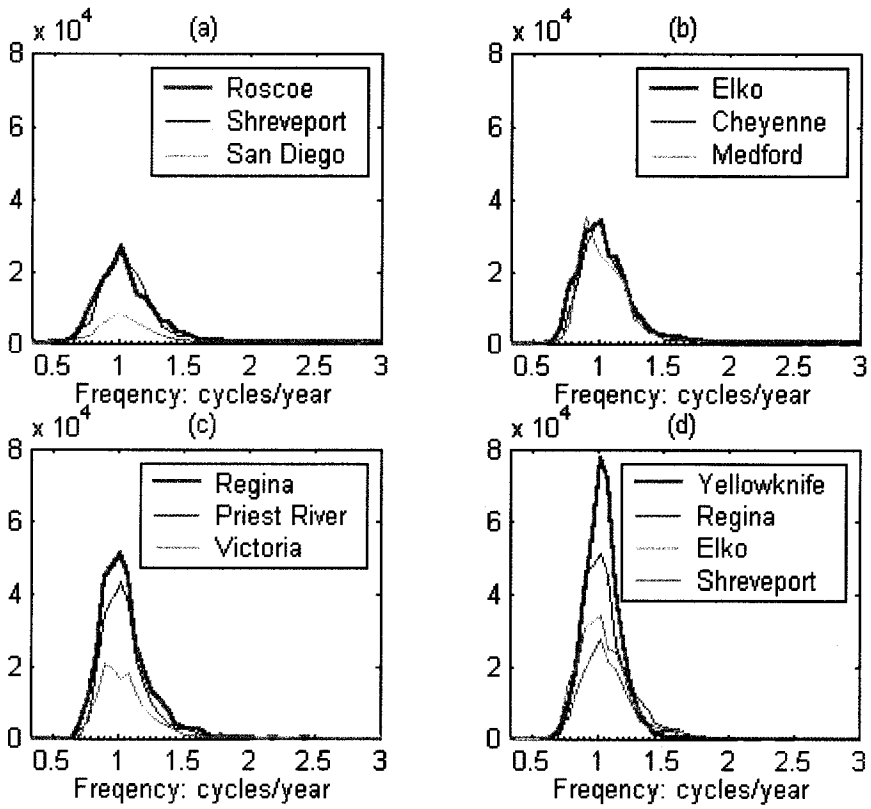

Figure 2.10. The marginal Hilbert spectra of the NAC for the daily maximum temperature at ten North America land stations. (a) Roscoe and Shreveport, San Diego. These three stations are located around the latitude zone 32.47° N. (b) Elko, Cheyenne, and Medford. These three stations are located around the latitude zone 41.15° N. (c) Regina, Priest River, and Victoria. These three stations are located around the latitude zone 48.65° N. (d) Yellowknife (the north-most), Regina, Cheyenne and Roscoe (the south-most). The ordinate's unit is [°C][Year/365].

2.5.2 Variances of anomalies with respect to the NAC and TAC

We compared the variances of anomalies with respect to the NAC and TAC at all stations. The results show that the mean monthly variances of the NAC anomalies are smaller than those of the TAC in most months. The overall variances of the NAC anomalies are smaller than those of the TAC anomalies (Figures 2.11). These results suggest that the EMD can separate the intrinsic modes of the SAT data better than the TAC filtering.

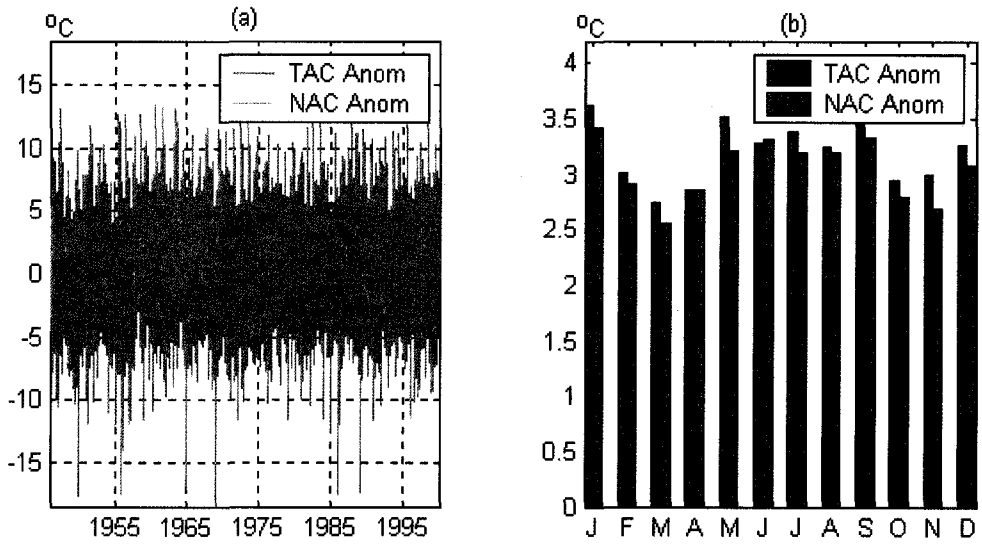

Figure 2.11. The anomalies of the TAC and NAC of the daily maximum SAT data at the Victoria station (left) and the mean deviation of the anomalies for each month (right).

2.5.3 Spectral power of the anomalies with respect to the NAC and TAC

After the removal of the TAC, one expects that the annual cycle will have been filtered out from a station's temperature data since the data's Fourier transform shows a

strong peak at the frequency of 1 cycle/year. However, one can detect some non-trivial spectral power in the frequency neighborhood of 1 cycle/year. A good filter for the annual cycle should remove not only the monotonic spectral power of 1 cycle/year, but also the spectral power in its neighborhood. The NAC can be such a filter, which filters out the annual cycle more cleanly than the TAC. The main reason is the nonlinearity in the climate system, whose spectra are not discrete but continuous. Thus, the anomalies about the TAC contain more spectral power around the annual cycle than those about the NAC. Figure 2.12 shows the Fourier spectra of the daily maximal SAT's NAC and TAC and the corresponding anomalies for four stations. Each station has two panels: the first one is for the TAC and NAC, and the second is for the NAC and TAC anomalies. The spectral power of the TAC anomalies is always larger than that of the NAC anomalies around the frequency of 1 cycle/year. Thus, strictly speaking, the NAC is a better filter for the annual cycle than the TAC. Of course, the ordinates of the first and second panels are of different sizes. The spectral power in the anomalies is much smaller than that of the original data around the frequency of 1 cycle/year. However, due to the climate system's nonlinearity, the anomalies are very important and can transform non-negligible energy that produces an abnormal climate, such as that caused by El Niño.

The second panels of Figures 2.12(a)-(d) indicate the relevant positions of the NAC and TAC anomalies' spectral lines: the TAC anomaly's spectra are above the NAC anomaly's spectra. To demonstrate the relative position quantitatively, we integrated the spectral power of both anomalies around the frequency of 1 cycle/year. The results for

the interval [0.9, 1.1] cycles/year are shown in Table 2.2. In general, the spectral power of the NAC anomalies in this interval is less than ½ of that of the TAC anomalies. Table 2.2 also includes the ratios of the TAC spectral power to the NAC spectral power. It is expected that these ratios would be less than 1.0. Among the ten stations considered, nine fulfill this expectation. The exception is the Medford station (42.38°N, 122.87°W), Oregon, United States, where the ratio is 1.02. A nearby station, Cottage Grove (42.72°N, 123.05°W), Oregon was considered to check this abnormal case. The ratio is 0.97. Thus, in general, we can conclude that the ratios of the TAC spectral power to the NAC spectral power around the frequency of 1 cycle/year are less than 1.0.

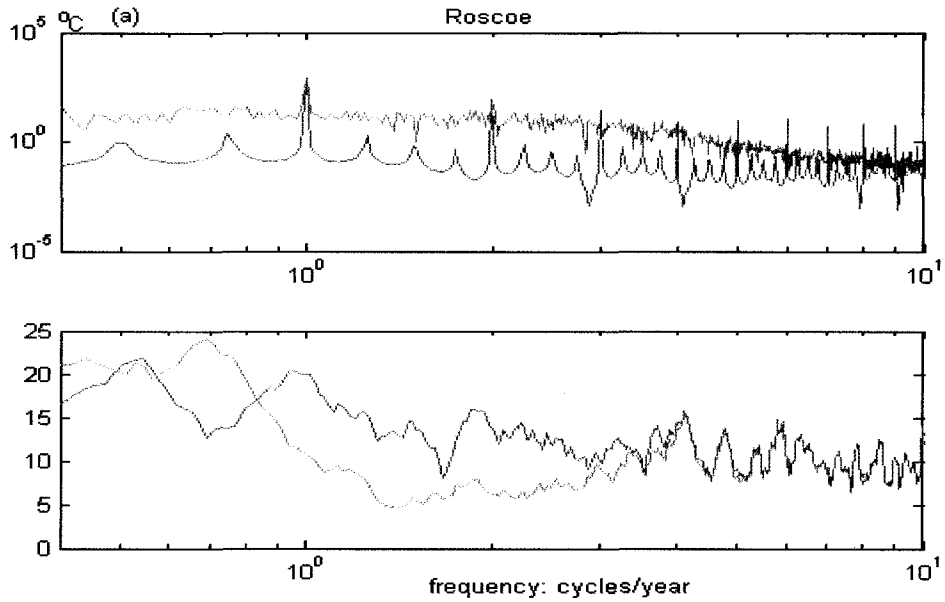

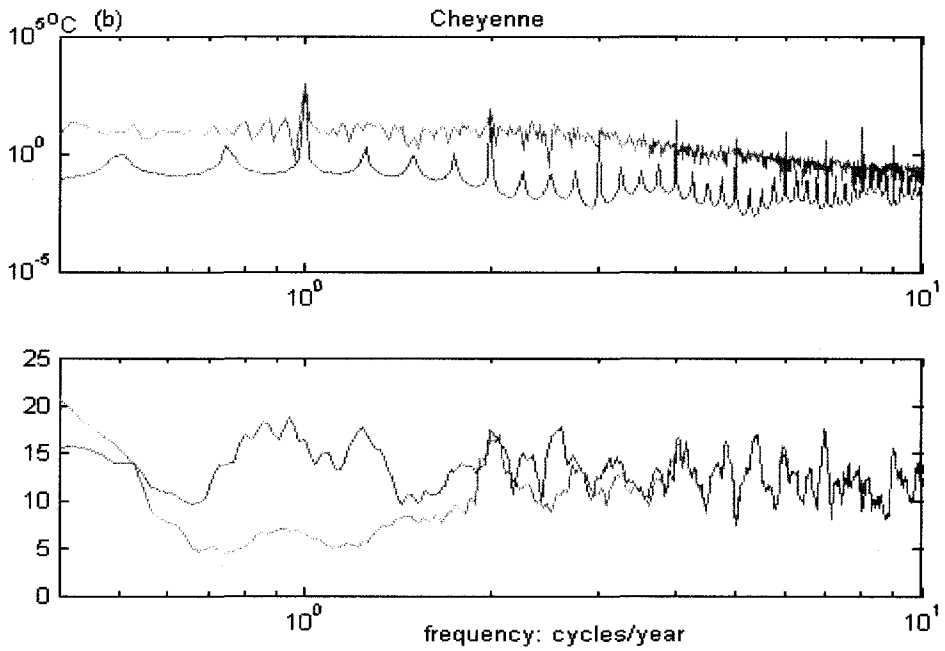

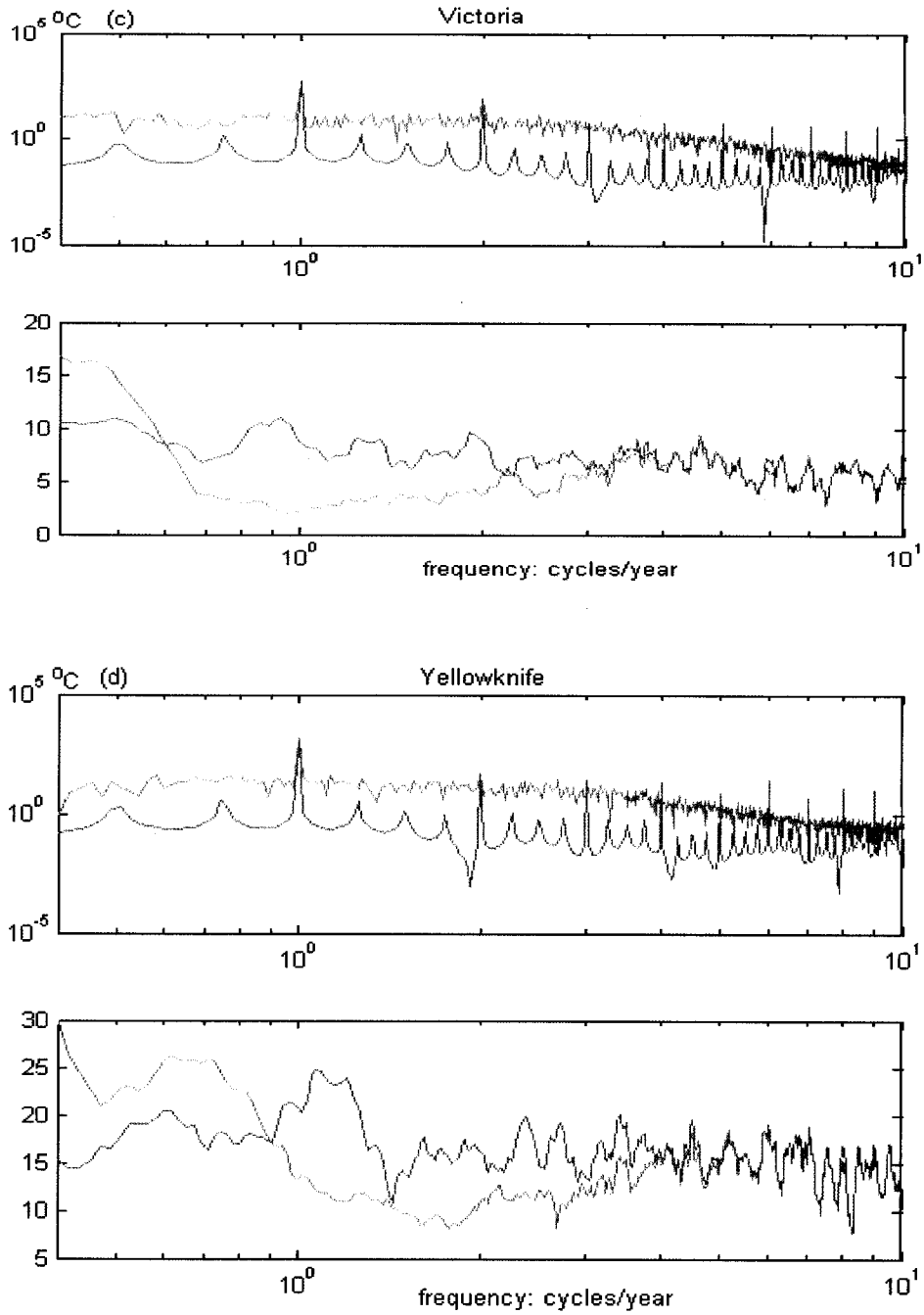

Figure 2.12. Fourier Spectra of the NAC (red) and the TAC (upper panels), and those of the anomaly data of the NAC and the TAC (lower panels) at stations (a) Roscoe, (b) Cheyenne, (c) Victoria , and (d) Yellowknife. The Fourier spectra of the anomaly data are smoothed by a 10-point moving average.

Table 2.2. The ratio of the energy around 1cycle/year of anomaly data with respect to the TAC and the NAC and that of the annual cycles at all stations

Station	$\frac{\int_{0.9}^{1.1}\lvert Anom_{TAC}\rvert^2 d\omega}{\int_{0.9}^{1.1}\lvert Anom_{NAC}\rvert^2 d\omega}$	$\frac{\int_{0.9}^{1.1}\lvert TAC\rvert^2 d\omega}{\int_{0.9}^{1.1}\lvert NAC\rvert^2 d\omega}$
Roscoe	3.6	0.93
Shreveport	6.2	0.96
San Diego	4.1	0.95
Elko	8.0	0.99
Cheyenne	5.6	0.98
Medford	1.4	1.02
Priest River	8.5	0.99
Victoria	18.7	0.94
Regina	17.3	0.96
Yellowknife	2.3	0.98

2.6 Conclusions and discussion

We have used the EMD method to derive the nonlinear non-stationary annual cycle for both the SAT by using land stations in North America and the SST in the Niño 3.4 region. The non-stationary annual cycle (NAC) has been compared with the commonly used thirty-year-mean annual cycle (TAC). The NAC allows daily resolution and is robust with respect to the length of a data stream and the end conditions of the EMD method. The EMD procedure used in the paper can accurately separate the annual cycle in a synthetic dataset composed of multiple harmonics, a nonlinear trend, and white noise. A comparison of the NAC and TAC in spectral space indicates that the NAC is a better filter for the annual cycle than the TAC.

Many problems involving annual cycles are worth investigation. A few are listed here.

(i) Can one use the NAC anomalies of the Niño 3.4 SST data or the buoy data in the same area to define the El Niño events?

(ii) If the NAC anomalies are calculated from the 5-degree-by-5-degree grid boxes for the NCAR/NCEP Reanalysis data, and the empirical orthogonal functions (EOFs) are computed from these anomalies, then are the ENSO patterns distributed in the same way as those calculated from the commonly used TAC anomalies?

(iii) Discrete wavelet analysis can also yield modes of different scales. Is there a systematic method to compare the modes derived from the EMD, wavelet analysis, and even some dynamical models?

Chapter 3

Statistical Analysis of Daily SAT Data

3.1 Introduction

Most climate change detection and attribution studies are based on the temperature data at monthly, annual, and even decadal scales (Folland et al., 2001; Mitchell et al., 2001). Daily surface air temperature (SAT) data are rarely used, mainly because no systematic mathematical methods exist to deal with the strong nonlinearity and non-stationarity embedded in the data of daily scales systematically. However, daily data are very important for studying the energy exchange between long and short spatial and temporal scales in nonlinear climate processes. These data are also important in the study of extreme climate events, such as extreme temperatures over Canada, Europe, and other regions, by using daily SAT data (Folland et al., 2001).

Persistency is the resistance to change, contrary to catastrophe. The persistency of weather during a short time period is obvious: a warm day is likely to be followed by another warm day, and a cold day is likely to be followed by another cold day. The persistence is also reflected in annual cycles. The annual cycle is the dominant recurring feature in SAT: the temperature drops every fall and warms every spring in the Northern hemisphere, although the cooling and warming do not occur at exactly the same time and with the same amplitude every year.

The daily or monthly SAT is often modeled as a fixed annual cycle, which does not vary from year to year, plus an anomaly. The daily-resolution annual cycle is usually calculated either as the long-term mean value for each given calendar day or as a sinusoidal function with a period of 365 days fitted from data. The residuals, i.e. departures, from this fixed annual cycle are anomalies. The temperature anomaly series are then analyzed to assess climate changes. Are there any statistically significant linear trends? Are the series trend-stationary, non-stationary, long-term dependent, or anti-persistent? The anomalies from the fixed annual cycles in daily SAT data have been modeled as trends plus a long-memory noise. By using this model to test for linear trends in daily SATs, the trend coefficients were found to be positive but insignificant in all cases and hence did not provide conclusive evidence of climate change (Gil-Alana, 2006).

The feedback processes in the climate system act to offset (by providing negative feedback) or to amplify (by providing positive feedback) the change. Examples of positive feedback include the effect of ice. Ice melts when the atmosphere gets warmer. Thus, less incoming solar radiation gets reflected, and more energy is absorbed by the Earth. In consequence, the atmosphere gets warmer. Water vapor and carbon dioxide are also examples of positive feedback mechanisms. On the other hand, the clouds can be a negative feedback mechanism. The increase of temperature leads to more clouds, which reflect coming solar radiation and thus cool the Earth. In general, the climate system is stable if negative feedback dominates.

The statistical property of long-memory or anti-persistency in temperature time

series is related to the positive or negative feedback from the Earth's climate system (Kärner, 2002). A long-memory process exhibits a geometrically decreasing correlation between distant samples and tends to preserve the increasing or decreasing trend in the future. The anti-persistent process, on the contrary, is dominated by high-frequency oscillations and tends to prevent the trajectory from blowing up. Previous studies of daily SAT data found long-memory dependence and nonlinearity in daily SAT anomaly time series (Eichner et al., 2003; Király and Jánosi, 2002, and 2005). Kärner (2002) studied satellite-based global daily tropospheric and stratospheric temperature anomalies and found the anti-persistence property occurred over scales longer than 2 months in daily increments in the tropospheric anomaly temperature, while the autoregressive integrated moving average model was preferred for the stratospheric anomaly temperature. Kärner (2005) found very weak long-memory in daily SAT anomalies at five stations and dominating negative feedback for the time interval of 32 to 4096 days, and concluded that the Earth's climate system is better balanced than that suggested by simulations using climate models. Steady long-range dependence extending from 20 days up to 2000 days has been found in daily SAT anomaly time series at Australian stations (Király and Jánosi, 2005).

The above studies are all based on the daily temperature anomalies around the fixed annual cycle. However, the attempt to capture the cyclic effects with fixed parameters may be futile. Figure 3.1(a) shows the mean values of each calendar day during the 5-year periods from 1946 to 1950 and from 1996 to 2000 at the Yellowknife station. The

mean temperature from 1996 to 2000 was apparently warmer in winter than that of 50

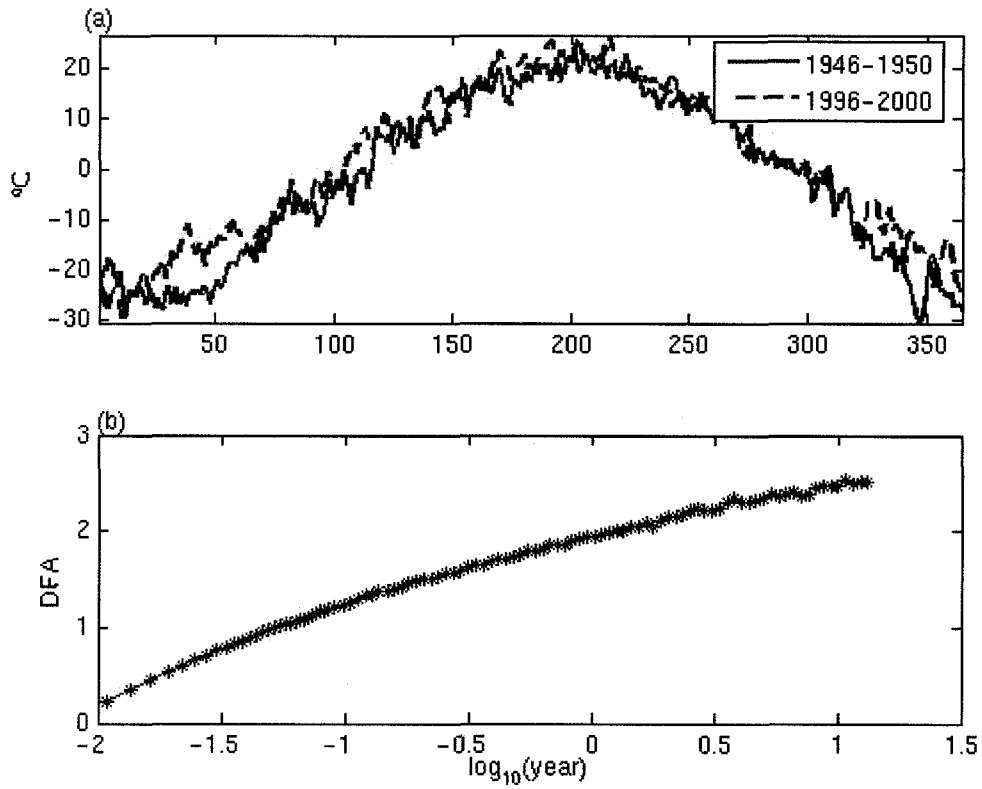

Figure 3.1. (a) The mean value of each calendar year from 1946 to 1950 and from 1996 to 2000 at Yellowknife station. (b) Detrended fluctuation analysis (DFA) of daily surface anomaly temperature data at Yellowknife station after a fixed trigometric annual cycle is removed from the SAT data.

years ago. Therefore, using a fixed annual cycle for the entire time series can produce a slowly varying component in the anomaly data. Figure 3.1(b) is an example of the detrended fluctuation analysis (DFA) of daily surface anomaly temperature data from the fixed annual cycle at the Yellowknife station. Given the change of the annual cycle during

the past century, spurious long-range dependency may be induced by the non-linear shifting of mean levels (Lewis and Ray, 1997).

Shen et al. (2005) studied the non-stationary annual cycle of daily surface temperature data filtered through the empirical mode decomposition (EMD) method. The resulting annual cycle was found to be not strictly sinusoidal and to vary from year to year with shifting amplitude and phase. This non-stationary annual cycle has the advantage of separating more power in the annual frequency. However, the issue of whether the non-stationary annual cycle contains information about climate change and the statistical properties of the residual after extracting this annual cycle was not studied. In this section of the thesis, we study the implications of the non-stationary annual cycle for climate change: the non-stationary annual cycle should reflect the effect of the long-term climate change, and the residual after extracting this cycle should contain plausible information of feedback from the climate system.

This chapter is organized as follows. Section 3.2 describes the daily and monthly surface temperature data at the 10 stations, which are almost the same as those in Shen et al., (2005). Section 3.3 presents the model for the non-stationary annual cycle and the non-linear time series model for the residual time series. The DFA method is an important tool in analyzing the long-memory property of time series and is also described in section 3.3. The resulting annual cycles are examined for possible climate change, and the anomalies to the fixed annual cycle, the EMD annual cycle, and the new non-stationary annual cycle are analyzed by using the DFA method for the long-range dependency or the

anti-persistency property. The results are presented in section 3.4. The conclusions are presented in section 3.5.

3.2 Data

The dataset used in this study is the daily maximum surface air temperature data at 10 land stations of different latitudes in the USA and Canada from the Global Daily Climatology Network (GDCN v1.0) dataset of the US National Climatic Data Center (NCDC). Since meteorological winter roughly begins on December 1 over much of the continental United States, we define a "year" as lasting from December 1st to November 30th of the following year. The GDCN covers a very long time period, but we use only the data from December 1, 1945 to November 30, 2000. The name and location information of the stations are listed in Table 3.1. The very small number of missing data in this dataset are interpolated by using cubic spline fitting in the temporal domain. More details of the data can be found in Shen et al., (2005).

Table 3.1. Inventory of the ten stations used in this study.

Station name	Location
Roscoe, Texas	32.45°N, 100.53°W
Shreveport, Louisiana	32.47°N, 93.82°W
San Diego, California	32.73°N, 117.17°W
Elko, Nevada	40.83°N, 115.78°W
Cheyenne, Wyoming	41.15°N, 104.8°W
Medford, Oregon	42.38°N, 122.87°W
Priest River, Idaho	48.35°N, 116.83°W
Victoria, B.C.	48.65°N, 123.43°W
Regina, Saskatchewan	50.43°N, 104.67°W
Yellowknife, NWT	62.47°N, 114.43°W

3.3 Method

Before proceeding to the non-stationary annual cycle, it will be useful to examine the fixed SAT annual cycle modeled by trigonometric functions. Figure 3.2(a) shows the daily surface temperature data at the Yellowknife station from December 1, 1945 to November 30, 1950. The seasonality is apparent in this time series, with a high temperature in summer and a low temperature in winter, and it is usually modeled in time series analysis by using a standard dummy variable approach or a set of trigonometric functions at seasonal frequencies (Harvey, 1989). The modeling of the annual cycle by the average of the mean value of the each calendar day for a 30-year period in meteorological practice is, in essence, the dummy variable approach. By using the trigonometric function approach, the seasonal effect at time t can be written as

$$AC_t = \mu_0 + \sum_{j=1}^{P} \left(\gamma_j \cos(2\pi jt/365) + \tilde{\gamma}_j \sin(2\pi jt/365) \right).$$

If $P = [365/2]$, the trigonometric function modeling of the annual cycle is equivalent to the dummy variable approach. However, since the seasonal patterns vary smoothly over the year, it is reasonable to drop the high-frequency components. Campbell and Diebold (2005) used $P = 3$ to model the daily average temperature data. We found that $P = 2$ provides satisfying results for modeling the seasonal variation in our data. Therefore, the trigonometric function approximation provides a compact representation of the annual cycle component. The fixed annual cycle can be estimated by using the ordinary least-squares method.

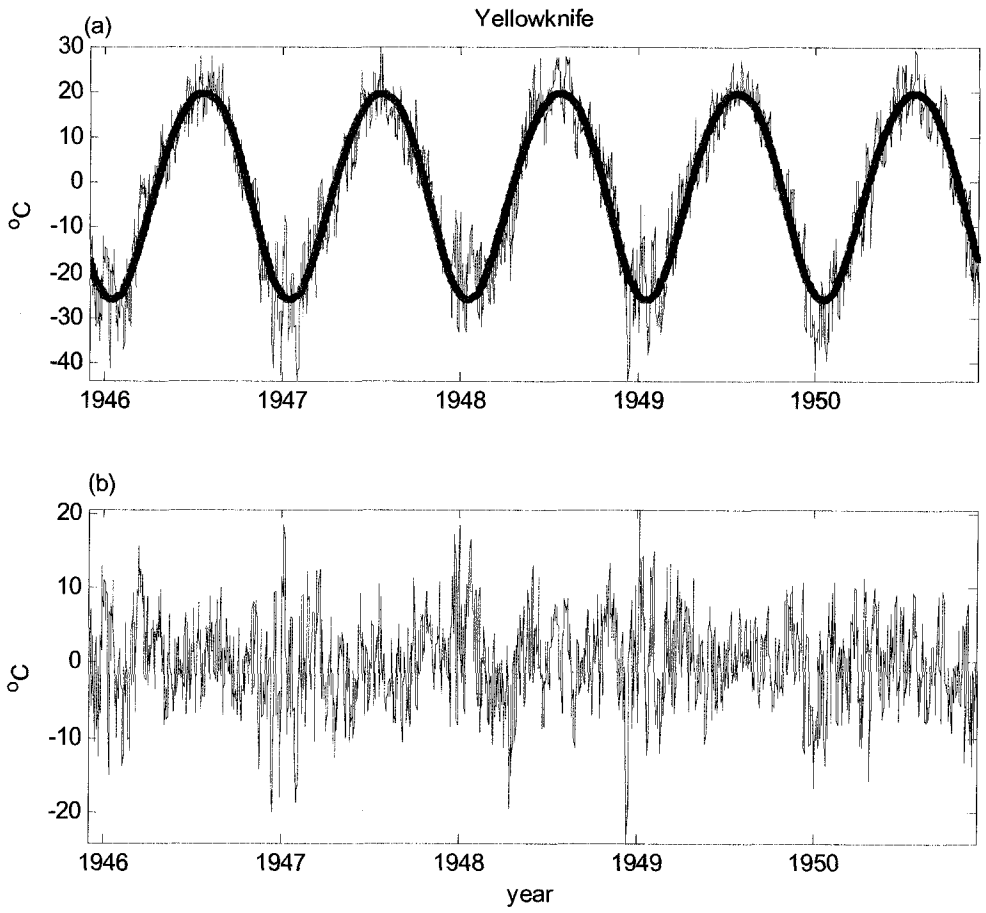

Figure 3.2. (a) The daily surface temperature data at Yellowknife station from December1, 1945 to November 30, 1950 (thin line) and the fixed annual cycle fitted using sinusoidal function including the first two periods. (b) The residual from this fixed annual cycle. The residual is clearly heteroskedastic with larger variation in winter and smaller variation in summer.

The fitted fixed annual cycle in the five-year daily temperature data at the Yellowknife station is shown in Figure 3.2(a), and the residual is shown in Figure 3.2(b). The residual clearly displays a heteroskedastic property with a larger variation in winter

and a smaller variation in summer. The residual's autocorrelation also shows strong correlations in the period of about three days. In summary, the time series that models daily SAT data should include an annual cycle to represent the strong seasonal cycle, and the residual from the annual cycle should include strong short-term correlations and the nonlinear dependence property throughout the season.

3.3.1 Non-stationary Annual cycle

As Figure 3.1(a) shows, the fixed annual cycle for the entire time-span in daily surface temperature data is not a good representation of the seasonal variation. We fit an annual cycle of the form

$$AC_{y,t} = \mu_y + \sum_{j=1}^{2}\left(\gamma_{y,j}\cos(2\pi jt/days) + \tilde{\gamma}_{y,j}\sin(2\pi jt/days)\right), \qquad (1)$$

where *days* can be 366 for a leap year or 365 otherwise, and $y = \lfloor t/days \rfloor$ is the corresponding year of time t measured in days. Therefore, the coefficients $\{\mu_y, \gamma_{y,1}, \tilde{\gamma}_{y,1}, , \gamma_{y,2}, \tilde{\gamma}_{y,2}\}$ vary with the year y. In this study, $y = 1946, \cdots, 2000$. The coefficient μ_y represents the shift of the mean temperature. The amplitude

$$\alpha_y = \sqrt{\gamma_{y,1}^{\ 2} + \tilde{\gamma}_{y,1}^{\ 2}} \qquad (2)$$

and the phase

$$\theta_y = \tan^{-1}\left(\frac{\gamma_{y,1}}{\tilde{\gamma}_{y,1}}\right) \qquad (3)$$

of the dominating annual frequency (i.e., $j = 1$) are examined for changes over time, where $\theta_y \in (-\pi, \pi]$. We are interested in a physically meaningful phase expression in units of days,

$$P_y = \theta_y \times days / 2\pi .$$

The mean temperature μ_y has been extensively studied in climate change detection (Folland et al., 2001), but the changes of amplitude and phase in annual cycles of the observed data have not received much attention. The larger the amplitude α_y, the larger the difference in temperature between summer and winter. Consequently, the climate tends to be more variable. A larger phase P_y, given the fixed amplitude and mean in the annual cycle, means the shift of the sine function to the left and thus indicates an earlier spring season. An example of a non-stationary annual cycle for the daily SATs at the Yellowknife station from December 1, 1945 to November 30, 1950 is shown in Figure 3.3. This non-stationary annual cycle varies with time and reflects the warm winter in 1948 and the cold winter in 1950.

The piecewise non-stationary annual cycle allows for discontinuity. Like the polynomial splines, a continuous non-stationary annual cycle can be defined by imposing the following continuity condition at the knots, which can be defined at December 1st of each year in our study. The continuity condition of the first order is

$$AC_{y-1,T_y} = AC_{y,T_y},$$

where T_y is the knot at year y. In addition, the smooth non-stationary annual cycle can be defined by imposing the continuity of the derivatives at the knots:

$$AC_{y-1,days}' = AC_{y,1}'.$$

However, in our experiment with daily SAT data at the ten stations, the piecewise annual cycle has the smallest mean squared difference to the EMD annual cycle and it

gives the smallest variation in the residual. Also, the results of the detection of climate change by using the piecewise annual cycle and the continuous non-stationary annual cycle are not of much difference. The smooth non-stationary annual cycle appears to be over-smoothed and cannot reflect the change of amplitude and phase from year to year. Therefore, we use the piecewise non-stationary annual cycle in the following study. The daily SATs are modeled as

$$T_{y,t} = AC_{y,t} + Anom_{y,t},$$

where $Anom_{y,t}$ is the residual after extracting the non-stationary annual cycle from the daily SATs.

The non-stationary annual cycle can also be applied to monthly data. Conventionally, monthly temperature data have been analyzed after removing the fixed annual cycle. A non-stationary annual cycle of the form

$$AC_{y,t} = \mu_y + \sum_{j=1}^{2}\left(\gamma_{y,j}\cos(2\pi jt/12) + \tilde{\gamma}_{y,j}\sin(2\pi jt/12)\right)$$

can be estimated from the monthly data where the period of the cycle is 12 months. This annual cycle of monthly data allows the level, amplitude and phase to change from year to year.

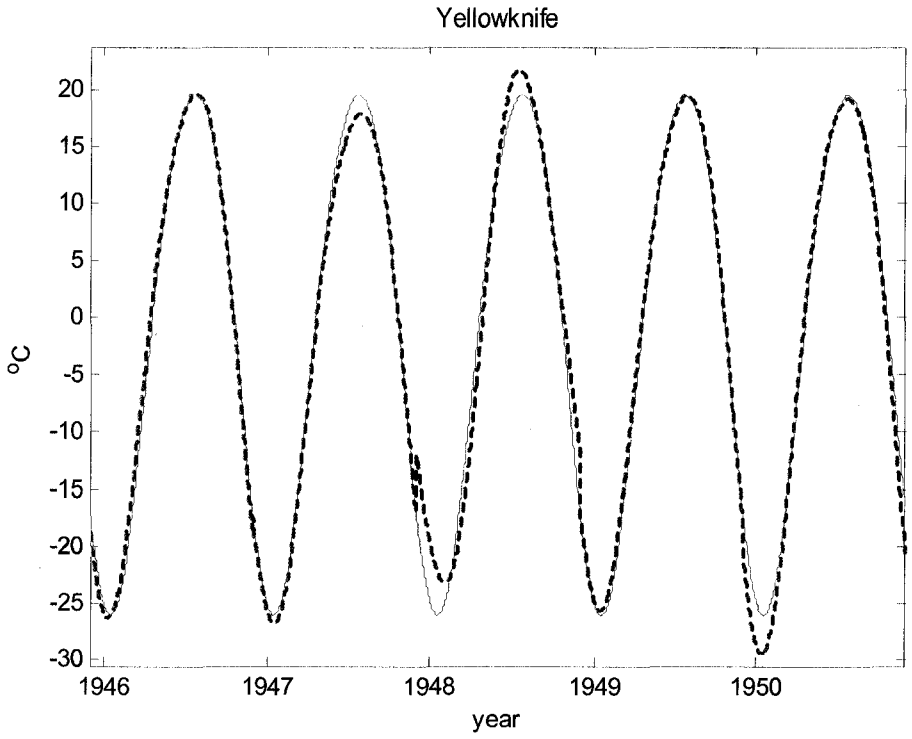

Figure 3.3. The non-stationary annual cycle for daily SATs at Yellowknife station from December 1, 1945 to November 30, 1950 (dashed line) and the fixed annual cycle (solid line).

3.3.2 Nonlinear time series model of temperature anomaly

To study the time series property of the anomaly from the non-stationary annual cycle, we plot its sample autocorrelation and partial correlation in Figure 3.4 by using the daily SAT at the Yellowknife station. Autoregressive (AR) model is used to model the short-range dependence in the anomaly data. The sample autocorrelation function and the partial autocorrelation function indicate that the AR(3) model is sufficient for modeling short-range dependence in the data (Figs. 3.4 a and b). The strong seasonal volatility

variation is evident in the correlograms of the squared residual (Figure 3.4 c) and

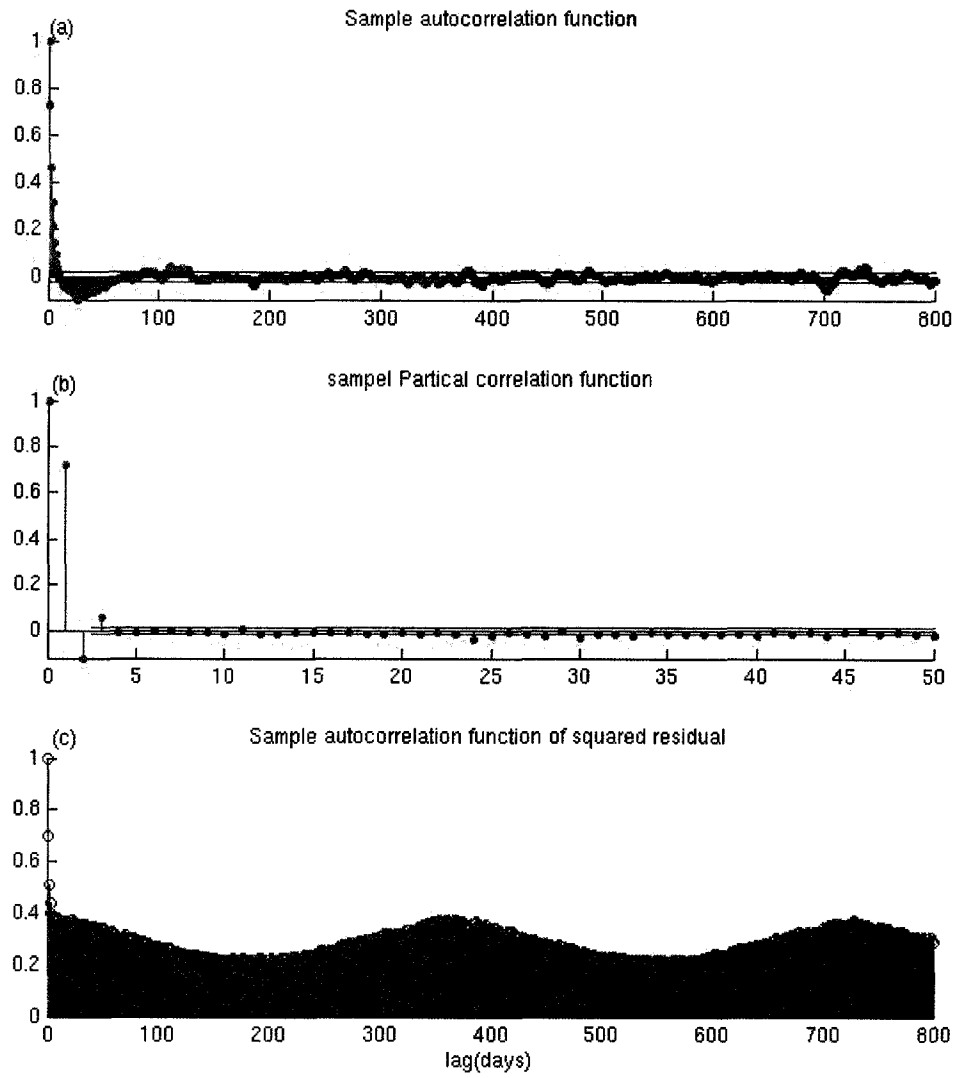

Figure 3.4. (a) The sample auto-correlation of the residual from the non-stationary annual cycle for daily SATs at Yellowknife station from December 1, 1945 to November 30, 1950 with 95% confidence interval for white noise. (b) The sample partial-correlation of the same residual with 95% confidence interval for white noise. (c) The sample auto-correlation of the squared residual.

indicates the need to incorporate heteroskedasticity into the model.

In light of the AR model and the residual heteroskedasticity, we use the model

$$Anom_{y,t} = \sum_{l=1}^{3} \rho_l Anom_{y,t-l} + \sigma_t \varepsilon_t, \tag{4}$$

where

$$\sigma_t{}^2 = \sigma_0{}^2 + \sum_{q=1}^{Q} \left(\gamma_q \cos(2\pi qt / period) + \tilde{\gamma}_q \sin(2\pi qt / period) \right),$$

and

$$\varepsilon_t \sim N(0,1),$$

where *period* is 366 for a leap year and 365 otherwise for the daily data, and 12 for the case using the monthly data. We use $Q = 2$ in our analysis, which is sufficient for the daily SATs at all the station we studied, as the high-frequency terms do not have a significant effect.

This model can be estimated by using maximum likelihood estimation. Here, we use an asymptotically efficient, two-step approach (Engle, 1982). First, the coefficients in the AR(3) part are estimated by using ordinary least squares. Second, the variation σ_t is estimated by regressing the squared residuals from Step 1 on trigonometric terms. The square root of the inverse can be used to construct a new estimator of the AR(3) part in the first step. The iteration stops when the likelihood function for the data converges. The autocorrelation functions of the estimated residual do not exceed the 95% confidence interval of white noise, and that of the squared residual does not have a seasonal variation

$f(\lambda) \sim k\lambda^{-2d}$ as $\lambda \to 0$, where $-0.5 < d \leq 0.5$. This concept bridges the gap between a non-stationary process and a stationary process with short-range dependency. If $0 < d \leq 0.5$, the fractional noise is stationary with long memory. Physically, the long-memory process keeps the tendency of the deviation from the past but still reverts to the mean in the distant future. If $-0.5 < d < 0$, the process is dominated by high-frequency noise and tends to prevent the tendency of the deviation from the past. Such a phenomenon is called "anti-persistency". The value of d can be extended to the range of between 0.5 and 1; the process becomes more non-stationary but still reverts to the mean. When d equals 1, the process becomes non-stationary; i.e., the mean level and the variances of the process become unbounded. Therefore, the order d of the fractional process can be used to characterize the stationarity of the process. In the time domain, the fractional differencing operator, given at $(1-L)^d$, where $-0.5 < d \leq 0.5$ and L is the backshift operator, has been used to model this phenomenon (Hosking, 1981).

Methods for estimating the order of the fractional process d have been developed rapidly over the past decade. Previous studies show that the order of persistency can be different in long and short time scales in daily temperature data (Kärner, 2002 and 2005). The scale breakdown in the dependency exponents between 10 to 30 days in the daily SAT anomaly data is observed in many analyses (Kärner, 2005; Király and Jánosi, 2005). Considering the complicated source of persistency of time scales from days to years, the same level of long-range dependency is unlikely to exist from days to multi-decadal scales. We need to study the change of dependency with time scales. For this purpose,

rescale-range analysis (also known as R/S analysis) and the detrended fluctuation analysis (DFA) can be used. The performance of DFA has been shown to be superior to R/S analysis (Hu et al., 2001). We use DFA analysis in this study.

Following the work of Peng et al. (1995), the DFA method has been applied to many research fields such as bioinformatics, economics, and meteorology. The property of the persistency or anti-persistency of the daily temperature anomaly data at stations in Europe and Australia has been studied by using DFA analysis (Lewis and Ray, 1997; Kärner, 2002; Király and Jánosi, 2005). The results show significant long-memory properties in the daily temperature anomaly from the fixed annual cycle.

The correlation properties of a time series at different scales can be estimated by using DFA (Hu et al., 2001). Consider a noisy time series $u(t)$, t=1,...,T. The steps of DFA are summarized as follows.

1. Integrate the time series $u(t)$ into a new series $y(t)$:

$$y(t) = \sum_{i=1}^{t} [u(i) - < u >],$$

where $< u >$ is the mean of the time series. The integration has the advantage of exaggerating the non-stationary of the original data and reduces the noise level.

2. The integrated time series $y(t)$ is divided into time intervals of equal size n. In each box, a local linear trend is subtracted from the series $y(t)$, and the detrended series is denoted by $Y(t)$.

3. For a given box size n, we calculate the root mean squared fluctuation function

$$F(n) = \sqrt{\frac{1}{T}\sum_{i=1}^{T} Y(i)^2} .$$

This three-step procedure is repeated for different box sizes n. The existence of a power-law relation between $F(n)$ and the box size indicates the presence of power-law dependency in the original data. To be specific, if $F(n) \sim n^{\alpha}$, where α is called "the DFA exponent", such a process has a power-law autocorrelation $C(\tau) \sim \tau^{-2(1-\alpha)}$ (Talker and Weber, 2000). Moreover, the relation between the order of the fractional process, d, and the DFA exponent, α, is

$$d + 1/2 = \alpha .$$

Consequently, the long-memory process is characterized by a DFA exponent $\alpha > 0.5$, and the antipersistent process has $\alpha < 0.5$.

In order to illustrate the behavior of the DFA coefficients $F(n)$ with time step n, four simple models of time series are used. The total length of the simulation is T=20089 days, the same length as that of our daily SAT data. Since the statistics break down for very large segments, we plot the DFA exponents at time scales from 4 days to 4801 days. The first one, corresponding to the fractional difference noise with d=0.15, or $\alpha = 0.65$, is simulated using the discrete Fourier algorithm (Wood and Chan, 1994). The choice of the order of fractional difference is consistent with the d close to 0.15 for the daily SAT anomaly at continental stations. Figure 3.6 (a) shows the simulated long-memory signal, and the log10(α) is plotted against the log10(*year*). The linear relation between the log of

the DFA exponent and the log of the number of years is a classical example of mono-scaling. The linear fit of the $\log10(\alpha)$ against the $\log10(year)$ gives the slope $\alpha = 0.64$.

The second example is long memory noise with a superposed linear trend:

$$y_t = 2.987 \times 10^{-5} \times t + \varepsilon_t,$$

where ε_t is the same long-memory noise as that in the first example. The slope of the linear trend corresponds to the increase of 0.6° during the period of our study. The expected crossover effect did not occur in the DFA exponents during the time scales we analyzed since the slope of the linear trend is too small compared to the noise component (Figure 3.6 (b)). Therefore, the slow-varying long-term climate change may not be detected at time scales from 4 days to 4801 days. This finding might explain why many previous studies did not find evidence of climate change during this temporal scale (Kärner, 2002 and 2005).

The third example is a cosine wave and a random component,

$$y_t = 5\cos(2\pi t / 365) + \varepsilon_t,$$

where $\varepsilon_t \sim N(0,1)$. The crossover phenomenon of the DFA exponents at one year is consistent with the period of 365 days, and the strong anti-persistency of scales longer than one year is forced by the strong cyclic components (Figure 3.6 (c)).

The last example is the cosine wave with nonlinear noise. The variance of the noise around the trough is two times as large as that of other segments. The behavior of the DFA exponent is the same as those of the third example. This finding indicates that the nonlinearity of the noise components does not affect the DFA analysis (Figure 3.6 (d)).

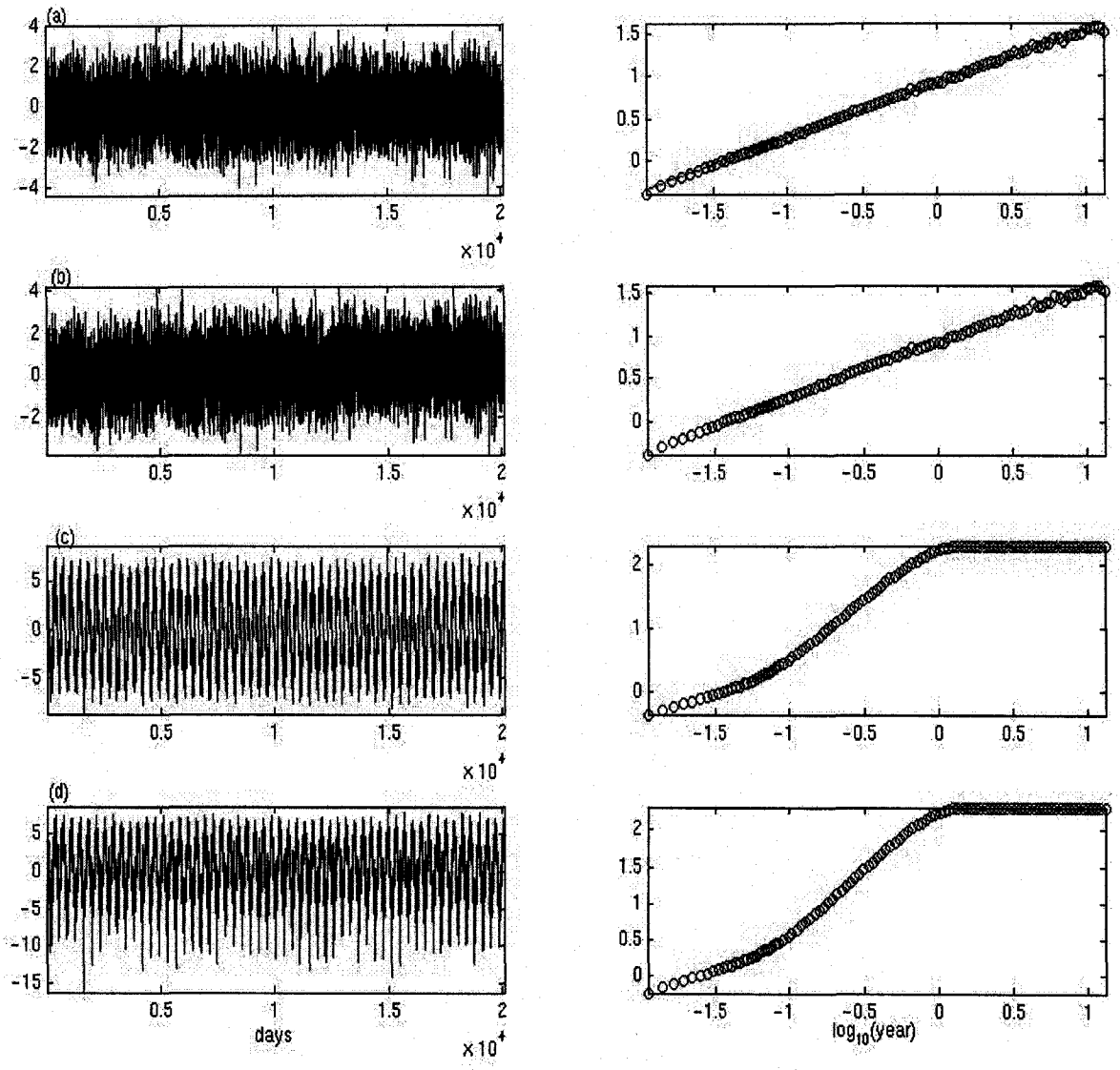

Figure 3.6. (a) Fractional difference noise with d=0.15 (left panel), and log10(DFA exponent) v.s. log10(*year*) (right panel). (b) Long memory noise with superposed linear trend (15 (left panel) and the corresponding DFA analysis (right panel). (c) Cosine wave with a random noise (left panel) and the corresponding DFA analysis (right panel). (d) Cosine wave with a nonlinear random noise (left panel) and the corresponding DFA analysis (right panel).

In general, the presence of a trend and a cycle in noisy signals can be indicated by the breakdown of the linear relation between the logarithms of the DFA exponent and that of the time scales. The characteristics of the crossovers depend on the slope of the linear trend and the cycle's amplitude and period. Also, crossovers can arise from a change in the correlation properties at different time scales.

3.4 Results

3.4.1 Detecting climate change in non-stationary annual cycle

We now proceed to examine the impact of climate change on the non-stationary annual cycle. The linear trend in the mean temperature μ_y, the amplitude of the annual cycle α_y, and the phase θ_y of the dominating annual frequency are examined for changes over time. An example of linear trends in the mean temperature, the amplitude of the annual cycles, and the phase of the annual cycle of the non-stationary annual cycle of daily temperature data at the Yellowknife station is shown in Figure 3.7. The mean temperature increases with the rate of 3.89 °C/century at this station. The negative trend in the amplitude of the annual cycle indicates the reduced variability of the annual cycle due to faster increasing winter temperatures than summer temperatures (Folland et al., 2006). The phase of the annual cycle also displays a significant positive trend at this station. This result suggests that the warm season at this location arrives earlier now than that of fifty years ago.

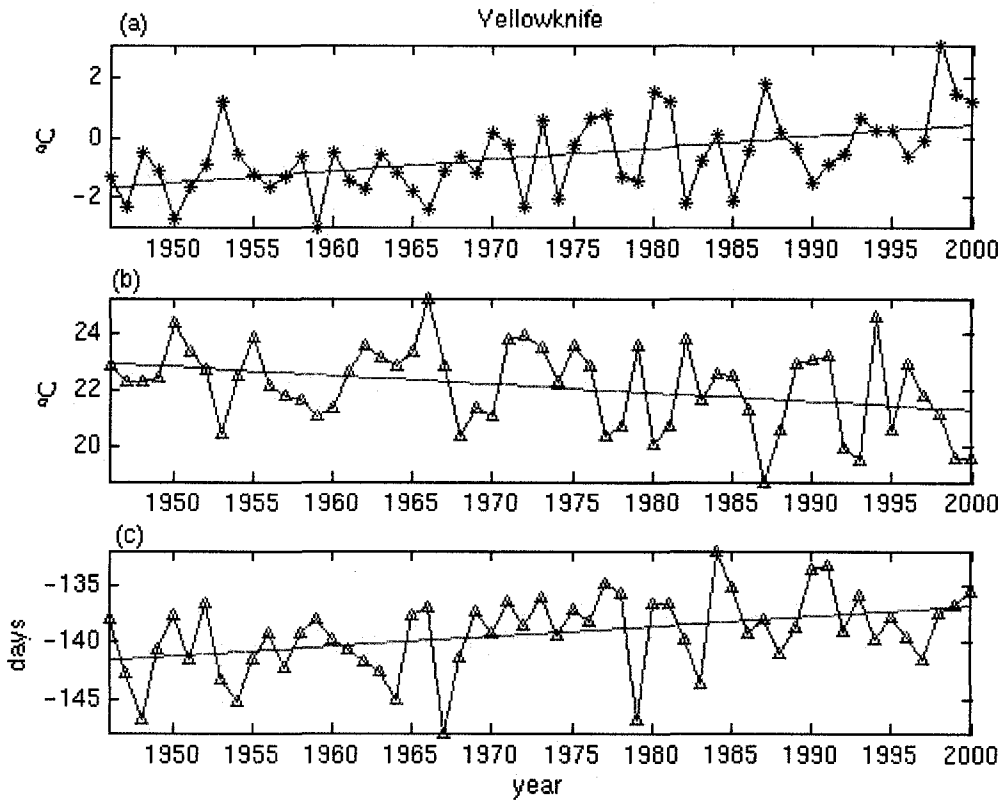

Figure 3.7.The mean temperature (a), the amplitude of annual cycles (b), the phase of the annual cycle (c) of the non-stationary annual cycle of daily temperature data at Yellowknife station and their linear trends (red lines).

For comparison, we also calculated the slopes of the linear trends in the mean temperature, and the amplitude of the annual cycle in the non-stationary annual cycle from monthly data. The results are shown in Table 3.2. The slopes calculated from the daily and monthly data are close to each other. The negative trend in the mean temperature at the Roscoe station may be due to excessive sulfates in the air (Yu et al., 2001) and the North Atlantic Oscillation (Hurrell and Loon, 1997; Ostermeier and

Wallace, 2003). The slope of the mean temperature data is more pronounced in the northern stations than in the southern stations. The trends in the amplitudes of the annual cycles are negative for all stations except the Priest River station. Also the trends in the phases of the annual cycles are positive except at the Medford station. This finding indicates an earlier arrival of the warm season at most of these stations. These results show that the climate change in daily data is reflected not only in the mean annual temperature but also in the amplitude and phase of the annual cycle.

Table 3.2. The slopes of linear trends in mean temperature, the amplitude of the annual cycle in the non-stationary annual cycle in daily data and monthly data, and the slopes of the phase of the annual cycle in the non-stationary annual cycle.

Station	mean temperature (°C/century)		amplitude of annual cycle (°C/century)		phase of annual cycle (days/century)
	Daily data	Monthly data	Daily data	Monthly data	
Roscoe	-1.47	-1.48	-1.53	-1.55	7.65
Shreveport	0.16	1.17	-0.71	-0.74	3.62
San Diego	-0.04	-0.04	-0.59	-0.63	7.89
Elko	0.45	0.44	-1.33	-1.35	4.98
Cheyenne	0.34	0.32	-0.85	-0.78	10.36
Medford	2.40	2.39	-0.26	-0.31	-2.59
Priest River	-0.35	-0.36	0.48	0.47	5.26
Victoria	1.76	1.76	-0.62	-0.66	2.42
Regina	3.07	3.10	-3.57	-3.42	12.12
Yellowknife	3.89	3.94	-3.23	-3.05	8.78

3.4.2 Persistency or anti-persistency in climate noise

The temporal variations of the anomalies from non-stationary annual cycles are analyzed in this section. We fit the non-linear AR model to the anomalies and estimated coefficients at all ten stations, as shown in Table 3.3. The large AR(1) coefficients in the residuals at all stations indicate the strong dependency of the temperatures on two consecutive days. The stations located near the ocean, such as the San Diego, Medford, and Victoria stations, display weaker seasonal and nonlinear effects in terms of residual variations than other stations at the similar latitude.

Table 3.3. Coefficients of nonlinear stochastic model of temperature anomaly

Station	AR coefficients				Non-linear coefficients			
	ρ_1	ρ_2	ρ_3	σ_0^2	γ_1	$\tilde{\gamma}_1$	γ_2	$\tilde{\gamma}_2$
Roscoe	0.72	-0.17	0.05	16.04	10.39	7.18	0.04	-0.11
Shreveport	0.67	-0.12	0.03	12.93	8.40	7.67	1.24	-0.45
San Diego	0.74	-0.13	0.00	4.05	0.95	1.25	-0.66	-0.14
Elko	0.79	-0.17	0.06	11.73	2.29	-0.47	-3.08	1.21
Cheyenne	0.64	-0.14	0.05	23.31	5.86	5.45	-4.43	0.43
Medford	0.73	-0.10	0.02	11.23	0.30	-1.54	-1.52	1.01
Priest River	0.86	-0.17	0.01	7.87	-0.34	-1.76	-0.54	0.72
Victoria	0.61	-0.01	0.00	5.36	-0.98	-0.79	0.58	0.17
Regina	0.70	-0.10	0.04	23.02	3.62	7.47	1.05	1.10
Yellowknife	0.79	-0.15	0.05	15.95	7.36	4.50	2.55	1.94

We next examine the dependency in the anomalies from the fixed annual cycle, the EMD annual cycle, and the non-stationary annual cycle by using DFA analysis. Here, we use the sum of the intrinsic mode functions after the annual cycle mode as the annual cycle from the EMD method. An example of DFA analysis using the daily SAT at the

Yellowknife station is shown in Figure 3.8. The slope of the DFA coefficients over the time scales from one month to four years in the temperature anomaly from the fixed annual cycle is 0.65, which indicates long-range dependence in the anomaly from the fixed annual cycle. The slope is close to the slope of DFA coefficients in the previous studies of daily SATs at other weather stations (Eichner et al., 2003; Király and Jánosi, 2002 and 2005). The DFA coefficients of the anomalies from the EMD annual cycle and the non-stationary annual cycle at scales of less than three months are close to that of the fixed annual cycle. This finding shows that the EMD annual cycle and the non-stationary cycle do not affect the short-scale dependencies. However, crossover points occur around the time scale of three months in the DFA coefficients of the anomalies from the EMD annual cycle, and the non-stationary annual cycle and the DFA coefficients deviate significantly from that of the fixed annual cycle from then on (circled lines in Figure 3.8). The slopes of the DFA coefficients over time scales larger than three months are 0.25 and 0.18, respectively. This finding indicates the strong antipersistency in the anomalies from the EMD annual cycle and the nonlinear cycle at time scales longer than months. The long-range dependencies at that time scale are removed by using the EMD and non-stationary cycles.

The DFA exponents over time scales from 4 days to 4801 days are also calculated for the time-dependency properties in the residuals after the short-range dependency is removed by using the AR(3) model, and in the final residuals ε_t in equation(4). The DFA coefficients of the residuals from the AR(3) model and the final residuals after

incorporating the heteroscedasticity are parallel to each other except for a vertical shift. This finding confirms the previous finding that the signals with different local standard deviations do not affect the results of the DFA components (Chen et al., 2002). The slopes of the DFA coefficients of the final residuals from the EMD annual cycle and the nonlinear annual cycle within three-month time scales are 0.54 and 0.55, respectively. The slopes of the residuals from the non-stationary annual cycles at scales of from 115 to 4801 days are consistently slightly smaller than those of EMD annual cycles at all stations.

The results show that both the EMD annual cycle and the non-stationary annual cycle explain the long-range dependency over time scales of more than three months. The climate noise driving the anomalies from these two annual cycles displays almost no long-range dependency over time scales of less than three months after the short-range dependencies are removed. On time scales of more than three months, the climate noise shows anti-persistency instead. This finding indicates the negative feedback from the Earth's climate system.

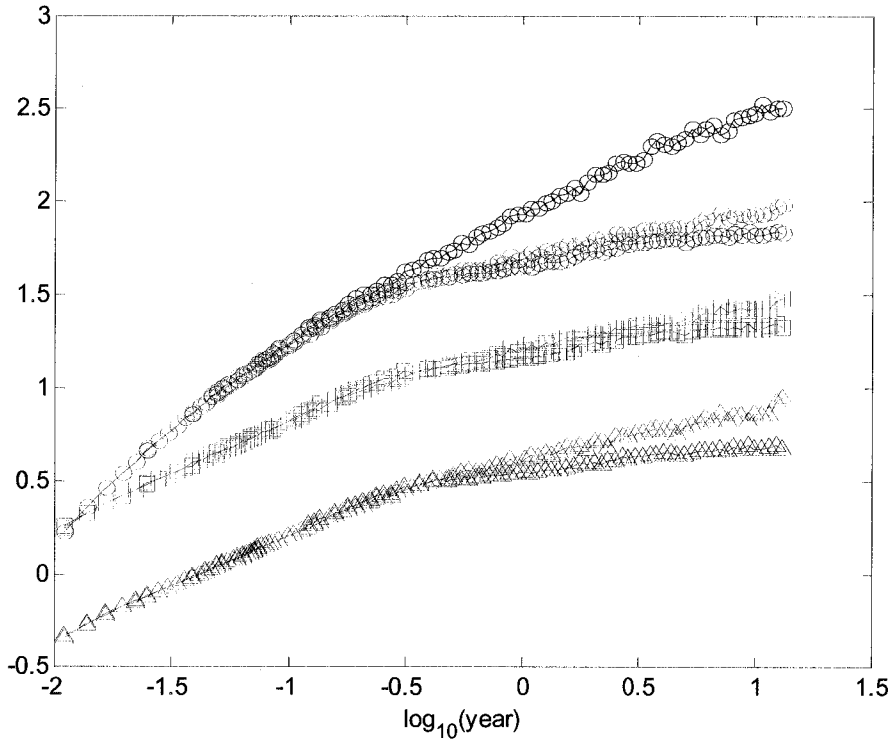

Figure 3.8. The DFA analysis of residuals from the fixed annual cycle (black line), EMD annual cycle (red lines), and the non-stationary annual cycle (blue lines). The direct DFA analyses of the anomalies from the three annual cycles are plotted in circled lines. The DFA analyses of the residuals of the EMD annual cycle (red) and the non-stationary annual cycle (blue) after the AR(3) components have been removed from the anomalies are plotted in squared lines. The DFA analyses of the final residuals, ε_t, after non-linear effects are removed, are plotted in triangled lines. The station is the Yellowknife station.

3.5 Conclusions

In our analysis, we have shown that the long-memory properties over time scales from 30 days to a decade in daily SAT anomalies occur because of the varying annual cycles. The removal of the fixed annual cycle from the observed SAT data may generate a slow-varying component in the anomalies and, thus, cause the long-memory phenomenon over time scales longer than three months. The time scales suitable for detecting climate change should be longer than the decadal scale. By using the non-stationary annual cycle proposed in this section, our results have shown that during the past fifty years, the amplitudes of the non-stationary annual cycles have been decreasing and that the phases have been increasing with time at most of the stations, especially those at the high latitudes.

Our DFA analysis have shown that the EMD annual cycle and the non-stationary annual cycle remove the long-range dependency from the daily SATs over time scales of more than three months from the daily SATs. The stochastic properties of the anomalies from the fixed annual cycle, the EMD annual cycle, and the non-stationary piecewise trigonometric annual cycle have been compared in this study. The anomalies from the nonlinear annual cycle display strong short-range dependency and nonlinearity. The nonlinear AR(3) model is adequate for modeling such phenomenon in the daily SATs at the ten stations we studied. The climate noise has been shown to be independent or of very weak dependence over time scales of less than three months. For time scales of over three months, the climate noise displays anti-persistency for both the EMD anomaly and

the anomaly from the non-stationary annual cycle. While this anti-persistency may point to the negative feedback from the Earth's climate system, the climate change can still be detected from the mean, amplitude, and the phase of the non-stationary annual cycle.

Chapter 4

Stochastic Trends in Surface Air Temperature Data in the Contiguous United States

4.1 Introduction

This chapter uses the dynamic factor analysis technique to study the long-term trend in the observed temperature data over the contiguous United States region. Dynamic factor analysis is an econometric method developed recently as a synthesizing and forecasting tool to analyze a large number of time series (Stock and Watson, 1989; Bai, 2004). Folland et al. (2001) noticed that although the data for the temperature reveal a consistent warming trend over most continental regions, these data also reveal a cooling trend in the some scattered regions including the southeastern US region. Figure 4.1 shows the area-weighted SAT anomaly time series for the southeast US and other US regions. The southeast US SAT time series shows a gradual warming from 1900 to the mid-twentieth century, followed by a pronounced cooling into the 1970s, and then a weak warming since the 1980s. In contrast, the time series for the rest of the contiguous US region shows very weak inter-decadal variations. The climate change detection and attribution in this region has been confounded by the striking disagreement between the

model-simulated temperature data and the observed data (Karoly et al., 2003; Knutson et al., 2006).

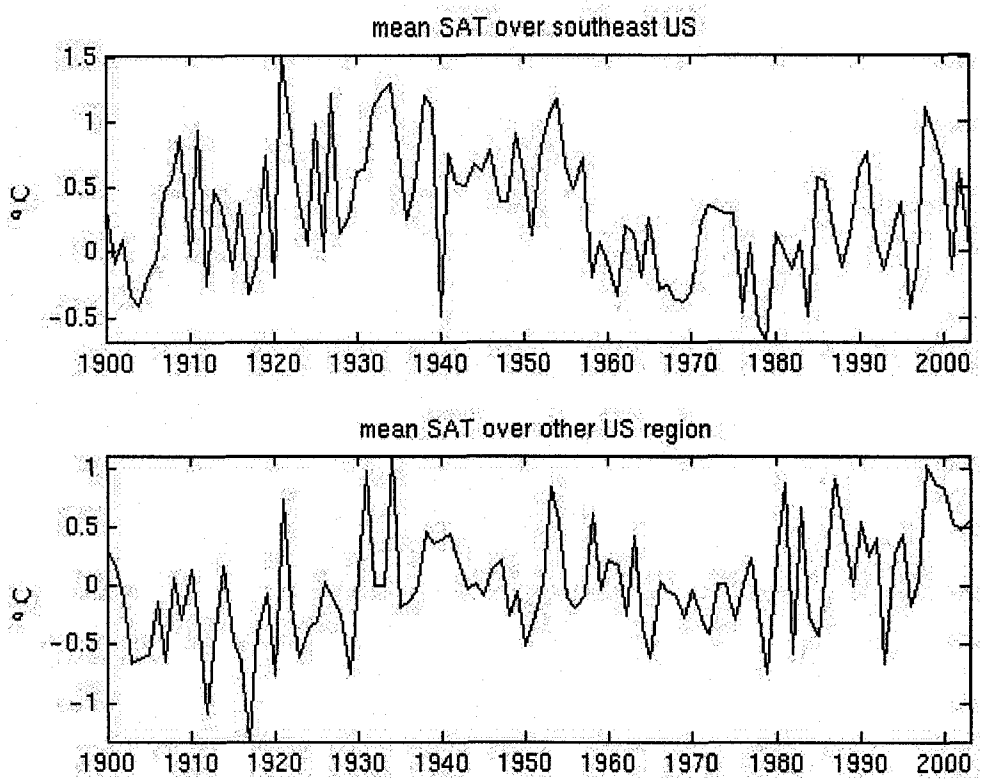

Figure 4.1. The area-weighted mean SAT anomalies over the southeastern US region and other regions except for the southeastern region from 1900 to 2003. See Figure 4.2 for the location of the southeastern US region.

The model simulations of the climate noise and climate response to external forcings have been the basis of most of the existing climate-change detection and attribution research. The multiple linear regression method regresses fingerprints of external forcings onto the observed surface temperature data (North and Wu, 2001; Stott,

2001; Stott et al., 2003; Zwiers and Zhang, 2003). Both anthropologically forced fingerprint signals and the natural variability are obtained from simulations of dynamic models, and it is assumed that climate models generate the climate change signals and the covariance matrix of climate noise correctly. Many studies also used the linear trend as the indication of the presence of anthropogenically forced climatic change in regional climate change detection (Karoly et al., 2003; Karoly and Wu, 2005). Karoly et al. (2003) compared the linear trend in some simple indices in the North American region with those in the model-simulated data forced by human and natural external influences to detect the human influence on climate in this region. These researchers noticed that the time series of the low-pass filtered ensemble mean temperature anomalies for this region from simulations with five global coupled ocean-atmosphere climate models do not agree with the observed warming between 1900 and 1949. In their attempt to assess the model's ability to interpret past climate variations, Knutson et al., (2006) found discrepancies in the observed temperature data in the southeastern United States region and the model simulations from the Geophysical Fluid Dynamics Laboratory global climate models.

The purpose of the present study is to discriminate signals of different spatial-temporal patterns from the observed data, as this could allow us to identify the source of the climatic changes in this region. This method does not hinge on the model-simulated climatic responses to external forcings. To date, Schneider and Held (2001) have been the only researchers who attempted this type of study. In their study, they isolated a spatial-

temporal pattern over the 20th century. This pattern is similar to the model-simulated greenhouse gas and sulphate aerosol fingerprints in the January and July surface temperatures. However, all other patterns they obtained were unstable and depended on the algorithm's parameters.

The dynamic factor analysis developed recently in econometrics allows for extracting the dynamic factors from large dimensional time series (Stock and Watson, 1988 and 1999; Bai, 2004). The purpose of this analysis is usually to model the long-term co-movement among many variables, to synthesize information in a large dimension factor model where dozens or hundreds of time series are to be analyzed, and to improve forecast accuracy (Bai, 2004). The co-movements among many variables can be extracted by using the vector error correction model (Engle and Granger, 1987), the structural model (Harvey, 1989), and the principal component method (Stock and Watson, 1999). The vector error correction model has been used to estimate the long-term relations between the hemispheric temperatures and the radioactive forcings (Kauffman and Stern, 2002). The structural model approach has been used to extract common trends in the northeast Atlantic squid time series (Zuur and Pierce, 2004). However, in these approaches, the number of the common trends needs to be assumed, and the estimation can be unstable when the dimension of the time series is high. In a number of studies, observed temperature data have been modeled as non-stationary time series (Kauffman and Stern, 2002; Stern and Kaufmann, 2000; Lenten and Moosa, 2003; Mills, 2006). The theory of the non-stationary factor analysis of the large-dimensional

data by using the principal component method has been established recently in econometrics (Bai, 2004). In this study, we use this approach to extract non-stationary factors from the grid box surface temperature data in the contiguous United States.

This chapter estimates the stochastic trends in the grid box data in the contiguous United States region and extracts the non-stationary factors and their associated spatial patterns. Section 4.2 describes the data we used in the analysis. In section 4.3, we review the Kalman filter and smoother method used to extract the non-stationary stochastic trends and the principal component method in the dynamic factor analysis. The dynamic factors extracted from the annual and seasonal surface air temperature data (SAT) over the contiguous United States region are presented in section 4.4. The conclusions are presented in section 4.5.

4.2 Data

This study uses the gridded Global Historical Climatology Network (GHCN) data (base period 1961-90) on $5^{\circ} \times 5^{\circ}$ grid-box basis datasets from 1900-2003 (Peterson and Vose, 1997). The GHCN V2 monthly surface air temperature (SAT) station data set is the source of the gridded dataset. The station anomalies are obtained primarily from the homogeneity adjusted station data having at least 25 years of data in the 1961-1990 base period by using the anomaly method. The station anomalies are then averaged within the $5^{\circ} \times 5^{\circ}$ grid box. In this study, the annual mean is based on the year from every December to the next November since the meteorological winter roughly begins in

December over much of the continental United States, The four seasons are winter (December to February), spring (March to May), summer (June to August), and fall (September to November). We calculate the seasonal mean of the monthly anomalies by allowing at most one missing data point in each season. The annual-mean anomaly temperature data are then computed through the average of the seasonal mean. We use only those grids with complete annual and seasonal mean anomaly data in this study (Figure 4.2). Forty-four grid boxes are used to cover the contiguous United States.

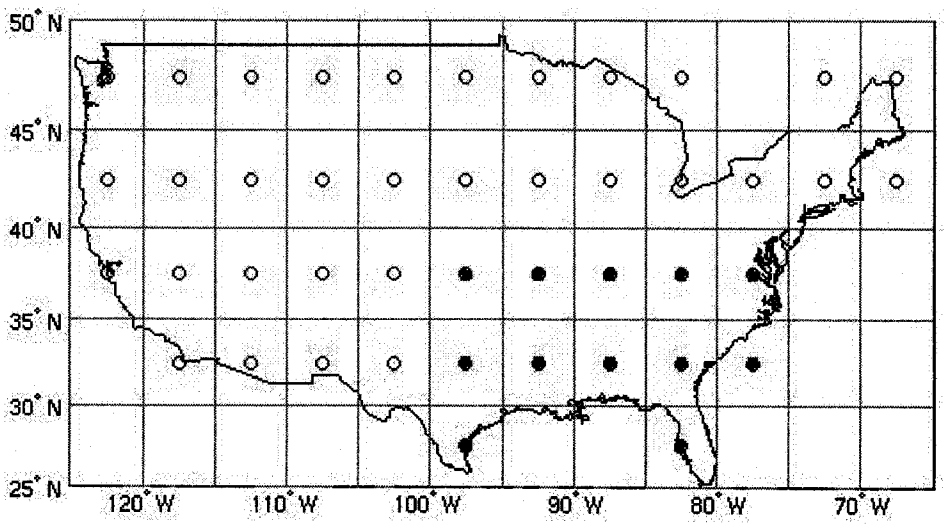

Figure 4.2. The grid boxes over the continental US region. The grid boxes with complete data from 1900 to 2003 are marked with circles. The southeastern US region is marked with filled circles.

4.3 Methodology

4.3.1 Stochastic trends

In statistical climatic change detection, the annual SAT data may be modeled as a trend plus random noise. Linear or other forms of deterministic trends have been used in most of the published studies (Folland, et al., 2001; Zhen and Basher, 1999; Seidel and Lanzante, 2004; Mills, 2006). However, such a deterministic model does not adapt to the evolvement of data with time and space. The stochastic trend model is a more flexible trend model in the sense that it is related to various forms of parametric and non-parametric trends (Koopman, 1997; Dubin and Koopman, 2001). The simplest stochastic trend is the random walk process, also called the local level trend. Although this model has a very simple form, it represents the development of a system over time and is related to the exponential smoothing and the autoregressive integrated moving average (ARIMA) model. The state-space approach is very general and covers the ARIMA model and many widely used filtering approaches. The advantage of the state-space approach is that it explicitly models the different components that make up the time series, and the desired feature can be easily identified from the results.

The observed SAT time series at the i-th grid point is modeled in terms of a non-stationary trend and another component:

$$T_{it} = \mu_{it} + \varepsilon_{it},\ t = 1, \cdots, K,$$

where μ_{it} is the trend component, and ε_{it} is Gaussian white noise. Here, μ_{it} is assumed to follow the random walk process or the local level trend

$$\mu_{it} = \mu_{i,t-1} + \omega_{it},$$

where ω_{it} is assumed to be Gaussian white noise uncorrelated with ε_{it}. We estimate the random walk trend independently from each grid box data. The non-stationary components are estimated by using the exact Kalman filtering and smoothing algorithm (Koopman, 1997, Durbin and Koopman, 2001). The exact Kalman filtering and smoothing algorithm is designed to deal with the diffusive initial condition in the case of the non-stationary trend component. Although the initial covariance of the state variable can be infinity, the one-step-ahead prediction error converges to a finite number after a limited number of steps, and the exact Kalman filter then transforms into the usual Kalman filter. The maximum likelihood estimators of the system parameters can be implemented by using the Newton-Raphson or EM-algorithms (Shumway and Stoffer, 2000, and Durbin and Koopman, 2001). In this step, the diffusive log-likelihood is used to account for the infinite initial variation in the non-stationary component. To maximize this log-likelihood, we use the constrained EM algorithm since some parameters or some elements of the parameters may be fixed (Wu et al., 1996).

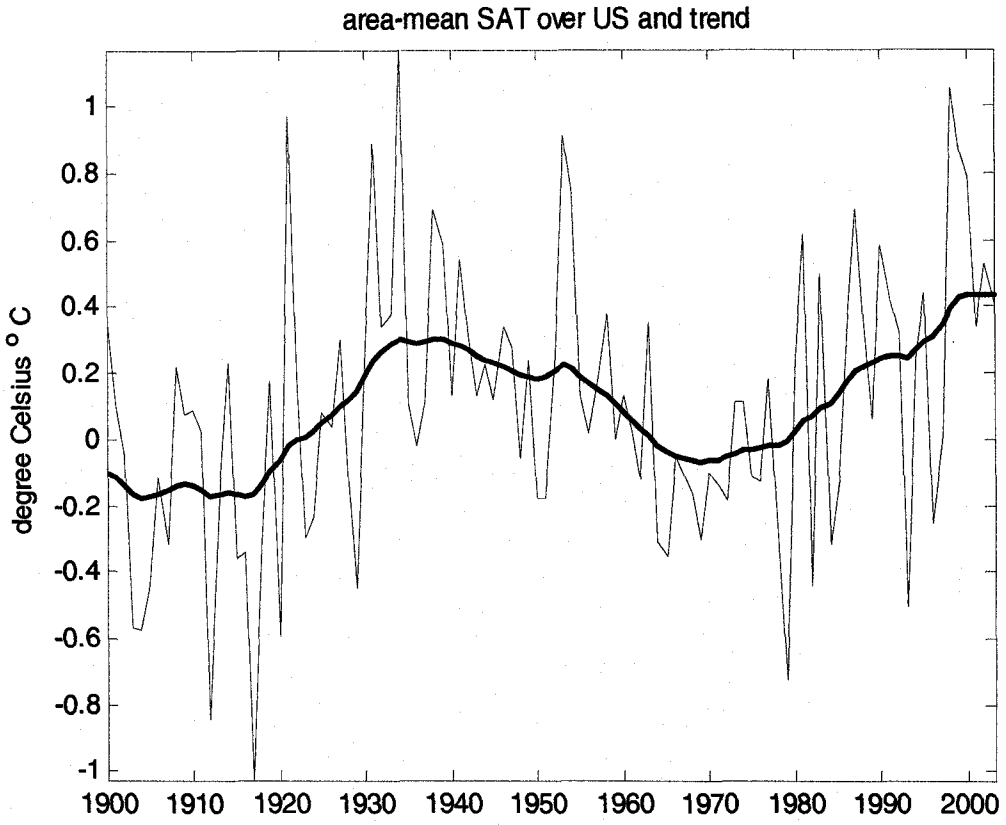

Figure 4.3. The stochastic trend (thick line) and the area-averaged surface temperature time series (thin line) over the contiguous US.

An example of the local level trend of area-averaged SATs over the US region is shown in Figure 4.3. The parameters are estimated as $\sqrt{\sigma_\omega^2} = 0.065$ °C and $\sqrt{\sigma_\varepsilon^2} = 0.35$ °C by using the constrained EM algorithm. This random walk trend shows a stable period between 1900 to the late 1910s (Figure 4.3). It starts to increase from 1920, reaches a peak in 1930s and then starts to decrease until the 1970s. The trend starts to increase again from around 1980 to 2003.

Other forms of the structural model can be used for the SAT anomaly data. For example, the trend can be modeled as the local level model

$$\mu_{it} = \mu_{i,t-1} + v_{i,t-1} + \omega_{it},$$
$$v_{it} = v_{i,t-1} + \xi_{i,t-1},$$

where both ω_{it} and ξ_{it} represent Gaussian white noise. As well, the observed SAT time series could be modeled by a trend, a cycle, and a noise component. Different structural models are compared by using the Akaike information criterion (AIC) and the Bayesian information criterion (BIC). With diffusive initialization in non-stationary trends, the AIC and BIC are given as follows:

$$AIC = \frac{1}{K}\left[-2\log L_d(T \mid \hat{\psi}) + 2(q+w)\right],$$
$$BIC = \frac{1}{K}\left[-2\log L_d(T \mid \hat{\psi}) + (q+w)\log K\right],$$

where $\hat{\psi}$ is the estimated model parameter, $\log L_d(T \mid \hat{\psi})$ is the diffusive log-likelihood function, q is the dimension of the non-stationary components, and w is the dimension of the model parameters ψ. This modified AIC and BIC means that the models with more parameters or more non-stationary components have a larger penalty.

The diagnostics of such a structural model are performed on the standardized one-step forecast error. The Ljung-box Q statistic is used for serial correlation, and the simple nonparametric H test is used for the presence of heteroscedasticity. Nyblom and Harvey (2001) provided a locally best invariant test of the deterministic linear trend against the smooth stochastic trendsy. However, the signal-to-noise ratio in the grid box

temperature data is extremely small, and even the locally best invariant test is difficult to use in this application.

4.3.2 Dynamic factor analysis

Dynamic factor models have been widely used in economic analysis to capture the co-movement of many variables in the form of common shocks and common stationary factors (Stock and Watson, 1999). Following the work of Bai and Ng (2004), the dynamic factor models are extended to study the cross-section co-integration among non-stationary time series.

A non-stationary time series is an *I(d)* process if it is stationary after differencing *d* times. If some linear combination of two or more *I(d)* processes is *I(d-b)* with $b>0$, these processes are said to be co-integrated of order *d*, *b*. The reduction in the order of integration implies some common long-run components exist among the series. For example, consider two *I(1)* variables x_t and y_t, and

$$\begin{pmatrix} x_t \\ y_t \end{pmatrix} = \begin{pmatrix} 1 \\ \theta \end{pmatrix} f_t + \begin{pmatrix} e_{1t} \\ e_{2t} \end{pmatrix}, \quad \theta \neq 0,$$
$$f_t = f_{t-1} + u_t,$$

where e_{1t}, e_{2t}, and u_t represent mutually uncorrelated Gaussian white noise. The fact that the variables x_t and y_t follow *I(1)* processes implies that (i) the spectrum of an *I(1)* process follows approximately the shape $f(\omega) \sim A\omega^{-2}$ for small ω, and due to the contribution of the low frequencies, the variances of x_t and y_t go to infinity as *t* goes to infinity; (ii) the variables do not tend to return to a mean or deterministic trend, and the

perturbations to the variables have a permanent effect. In this case, $z_t = (-\theta \quad 1)\begin{pmatrix} x_t \\ y_t \end{pmatrix}$, the equilibrium error is $I(0)$. The two variables x_t and y_t share a common stochastic trend f_t that drives the long-run co-movement of the two variables.

In general, consider the model

$$X_{it} = (\mathrm{A}_{i1}\mathrm{A}_{i2} \cdots \mathrm{A}_{ir})\,\vec{F}_t + e_{it},$$

(i =1, 2, ···, N, t = 1, 2, ···,K), where e_{it} is an $I(0)$ process that can be serially correlated for each I, and $\vec{F}_t = (F_{1t}, \cdots, F_{rt})'$ is a vector of dynamic factors which follows

$$\vec{F}_t = \vec{F}_{t-1} + \vec{u}_t,$$

where $\vec{u}_t$ is the vector of $I(0)$ processes that drive the stochastic trends $\vec{F}_t$, and the $N \times r$ matrix $A = \left(\vec{A}_1, \vec{A}_2, \cdots, \vec{A}_r\right)$ is called the factor loadings where A_{ij} is the weight of the j-th factor in the i-th variable, and $\vec{A}_j$ is interpreted as the weight of the j-th non-stationary factor. In this application, $\vec{A}_j$ is the spatial pattern associated with the j-th non-stationary factor. Several methods to estimate co-integrating vectors have been proposed in the literature. Among them are the ordinary least squares estimation (Engle and Granger, 1987), structural modeling (Harvey, 1989), and the principal component method (Stock and Watson, 1988). The principal component approach has been found to provide consistent estimates for stationary and stochastic common trends (Stock and Watson, 1999; Stock and Watson, 2002; Bai, 2004; Bai and Ng, 2004). The procedure for estimating common stochastic trends by using the principal component method is outlined as follows.

Denote $X = (X_{it}), (i = 1,2,\cdots,N,\ t = 1,2,\cdots,K)$, and $F = (\vec{F}_1, \vec{F}_2, \cdots; \vec{F}_T)_{r\times K}$. The principal component approach estimates common stochastic trends by solving the optimization problem

$$v(r) = \min_{A,F} (NT)^{-1} \sum_{i=1}^{N} \sum_{t=1}^{K} \left(X_{it} - (\mathrm{A}_{i1}\mathrm{A}_{i2} \cdots \mathrm{A}_{ir}) \vec{F}_t \right)^2,$$

subject to the normalization condition of either $FF' = I_{r\times r}$ or $A'\times A = I_{r\times r}$. In the case of $K < N$, to find F is equivalent to finding the first r eigenvectors corresponding to the largest r eigenvalues of the $K \times K$ dimensional matrix $X'X$, and $A = XF'(FF')^{-1} = XF'$. If $K > N$, the factor loadings $A = \left(\vec{A}_1, \vec{A}_2, \cdots, \vec{A}_r\right)$ is constructed from the first r eigenvectors of the $N \times N$ dimensional matrix XX', and $F = (A'A)^{-1}A'X = A'X$. Bai (2004) showed that the true common stochastic trends could be identified up to a linear transform.

In our analysis, the principal component approach cannot be performed on the gridded SAT anomalies directly since the non-stationary trend is contaminated by strong spatially correlated noise. Direct application of the principal component approach would give the mixed Empirical Orthogonal Functions (EOFs) of the noise e_{it} and the non-stationary common trends. Therefore, we extract the random walk trend from each grid box SAT before applying the factor analysis. The co-movement among the non-stationary time series is characterized by the common factors.

4.4 Results

4.4.1 Dynamic factors in annual SATs

In this analysis, we use the structural model with a local level trend to model the observed grid SAT data and to study the dynamic factors affecting the long-term co-movements among the extracted trends. The structural model of a local level model, a local linear trend model, and a trend-cycle model are compared at all grid data. The AIC and BIC criteria select the local level model for its simplicity and good performance. We calculate the random walk trends from the grid box SATs by using Kalman smoother iteration. The Ljung-box Q statistic for serial correlation and the simple nonparametric H test for the presence of heteroscedasticity are performed and the results show the estimated trend model performs well in terms of the goodness of fit at all grid box data. The random walk trends in annual SATs $\mu = (\mu_{i,t})$, $i = 1,2,\cdots,44$, $t = 1900,1901,\cdots,2003$, over all 44 grid boxes are used to compute the common stochastic trends by using the principal component approach. In this case, T=104 and is greater than N=44. Therefore, we calculate the eigenvectors and eigenvalues of $\mu\mu'$. The largest two eigenvalues for each dataset are listed in Table 4.1 The first two eigenvectors explain 89 percent of the variances in $\mu\mu'$. We rescale each of the factor loadings such that the element with the largest absolute value is 1, and the non-stationary dynamic factors are rescaled accordingly.

Table 4.1 The ratio of the first two eigenvalues with respect to the sum of all eigenvalues in principal component analysis of stochastic trends in winter, spring, summer, fall, annual SATs, and the annual SATs after interdecadal oscillations are removed.

	Winter	Spring	Summer	Fall	Annual	Annual-interdecadal
1	0.82	0.62	0.58	0.74	0.63	0.75
2	0.13	0.34	0.27	0.19	0.29	0.14

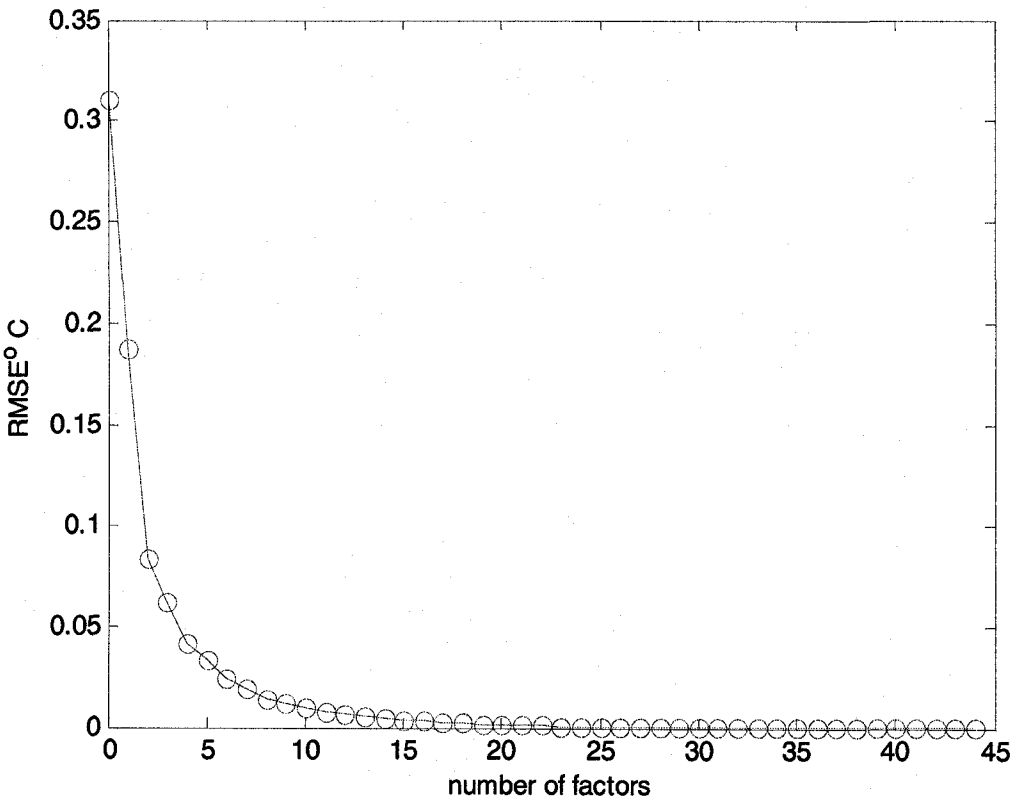

Figure 4.4. The root mean squared error of stochastic trends over all 44 grids, explained by an increasing number of factors.

First, we examine the power of the first two non-stationary dynamic factors to synthesize the information in 44 non-stationary trends. Figure 4.4 shows the root mean squared error of stochastic trends over all 44 grids, explained by an increasing number of factors for the stochastic trends in annual SATs. The root mean squared error decreases to

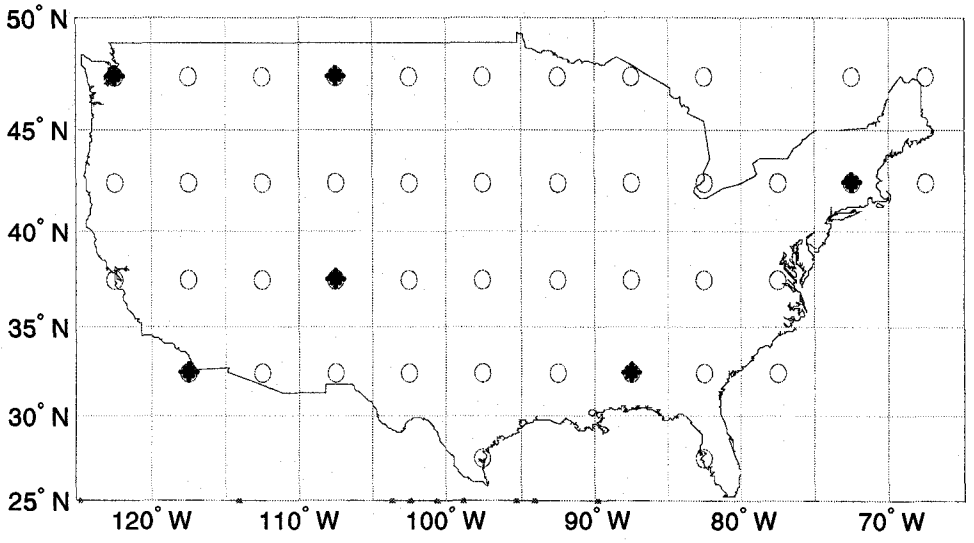

Figure 4.5. The location of the selected grid boxes in Figure 4.6

below 0.1°C after including the first two dynamic factors. We selected six grid boxes located across the region (Figure 4.5) and plotted the stochastic and reconstructed trend by using the first dynamic factor and the first two dynamic factors, respectively (Figure 4.6). In some grid boxes, such as the one located at (42.5°W, 72.5°W), the second factor

alone approximates the original random walk trend well; while in some grid boxes, such as the one located at (32.5°W, 87.5°W), the first factor alone approximates the original random walk trend.

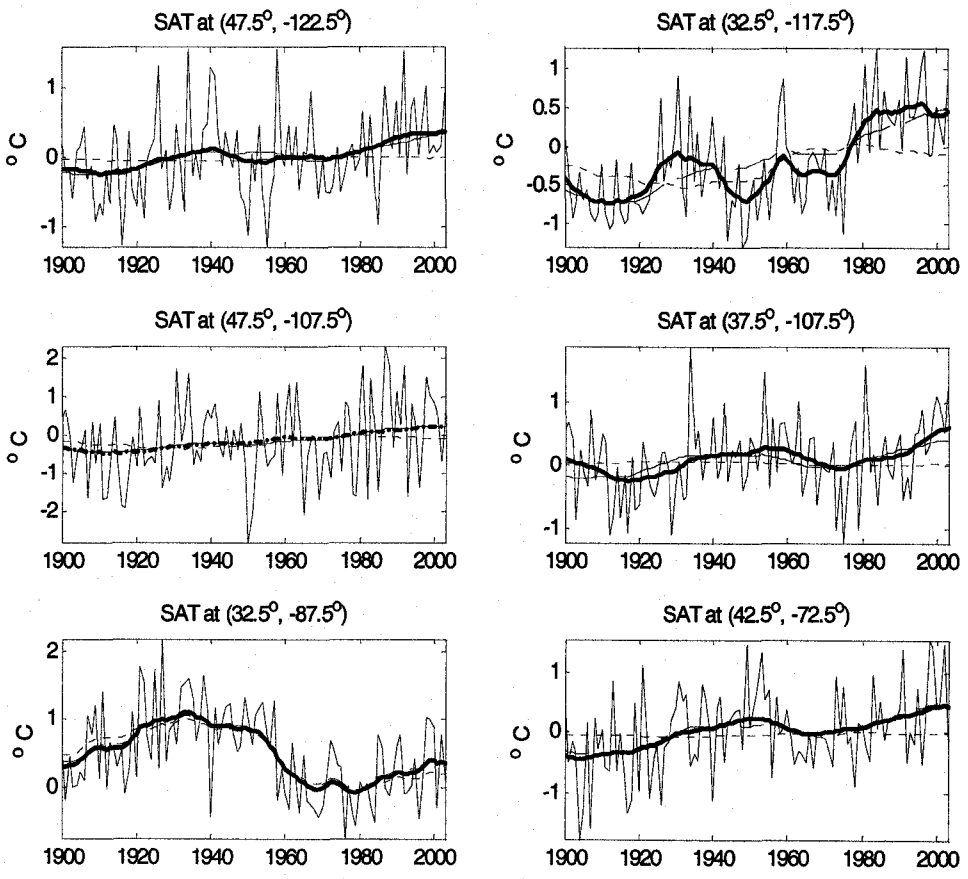

Figure 4.6. Trend components of the surface temperature data at some selected grid boxes indicated in Figure 4.4. The solid line in the middle is the stochastic trend. The dotted line is the trend component explained by the first non-stationary dynamic factor. The dash-dot line is the trend component explained by the first two non-stationary dynamic factors.

The first two rescaled non-stationary dynamic factors and the corresponding spatial patterns in annual SATs are plotted in Figure 4.7. The first dynamic factor is strong in the southeastern United States region and the time series indicates a warming period from 1900 to 1940s followed by a long cooling period from 1940s to the late1970s, and then a weak recovery from 1980. These findings are consistent with the previous observations that much of Northern hemisphere regions show a cooling trend from 1946 to 1975 and a warming trend from 1910 to 1945 (Folland et al., 2001). The second factor represents a warming trend over most of the contiguous US region, especially in the southwestern and northeastern regions, except for a slight cooling period from the 1960s to the 1970s. This phenomenon could be caused by the mixture of the inter-decadal variation with the monotonic trends.

The inter-decadal variation of the first dynamic factor and the associated spatial pattern are also consistent with the features of the inter-decadal signal in this region (Livezey and Smith, 1999). The second dynamic factor, however, is contaminated by an inter-decadal oscillation in the first half-century. To separate the inter-decadal oscillation signal from the monotonically increasing signal and to explore the source of these changes, we study the dynamic factors in the seasonal data.

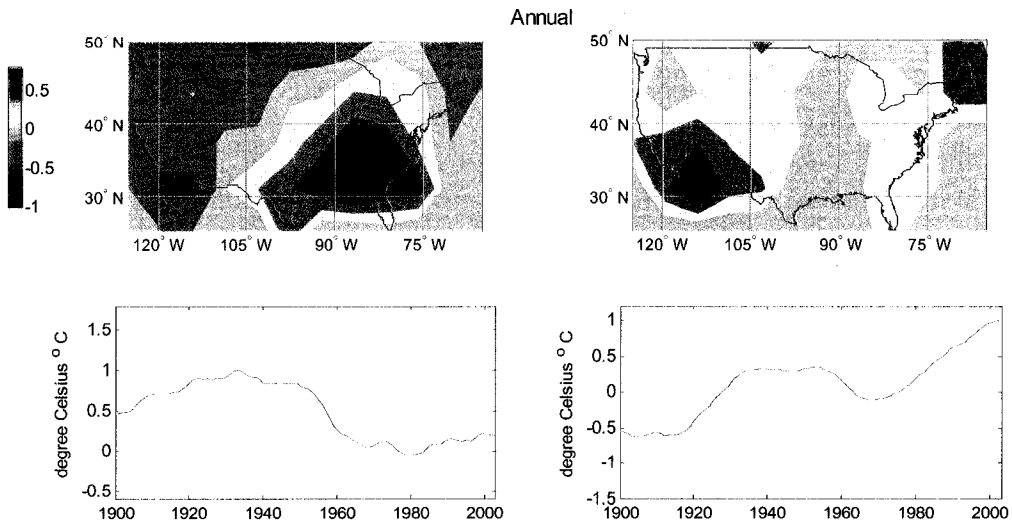

Figure 4.7. The principal spatial and temporal patterns of trends. Left column: the first dynamic factor (lower left panel) and the associated factor loading (upper left panel); right column: the second dynamic factor (lower right panel) and the associated factor loading (upper right panel).

4.4.2 Dynamic factors in seasonal SATs

The first two rescaled non-stationary dynamic factors for the stochastic trends consist of a nearly monotonic stochastic factor and an oscillatory factor for all four seasons' temperature data (Figure 4.8). The two largest eigenvalues for each seasonal dataset are listed in Table 4.1. The inter-decadal factors are separated well from the nearly monotonically increasing trend in the winter and summer temperature data. The leading factor for the winter temperature data is the inter-decadal oscillation representing the dynamics in the southeastern United States region. This factor explains 82 percent of the variations in the stochastic trends alone. In the summer season, the inter-decadal

oscillation is the second largest factor, whose associated spatial pattern shows it is more pervasive across the continent and stronger in the south than in the north. The spatial patterns of the inter-decadal factors suggest that this factor may be associated with the inter-decadal oscillation of North Atlantic oscillation (Hurrell and Loon, 1997; Ostermeier and Wallace, 2003).

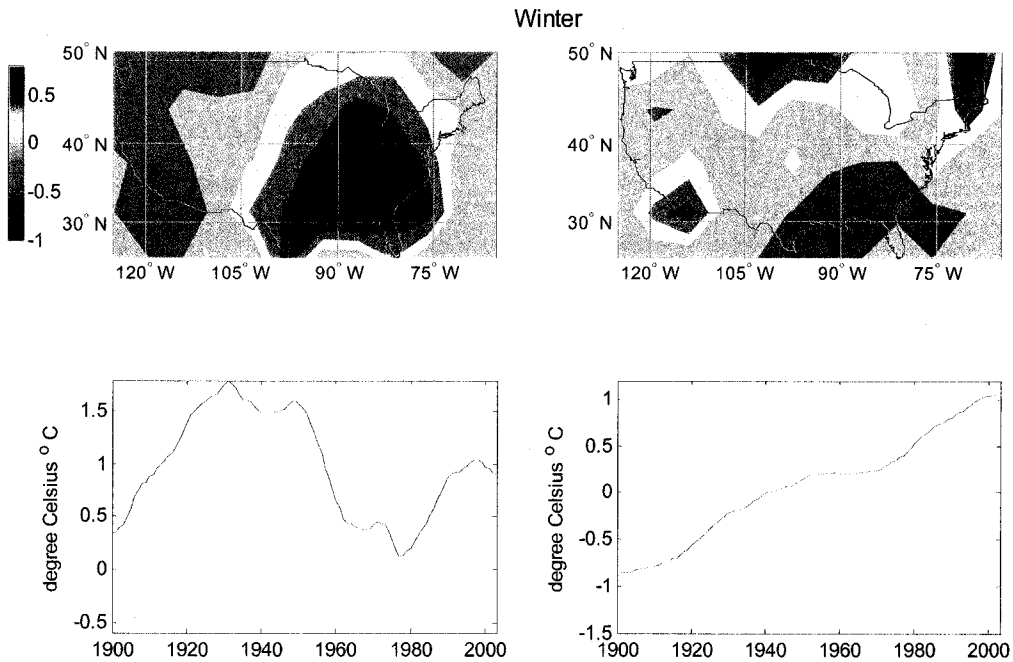

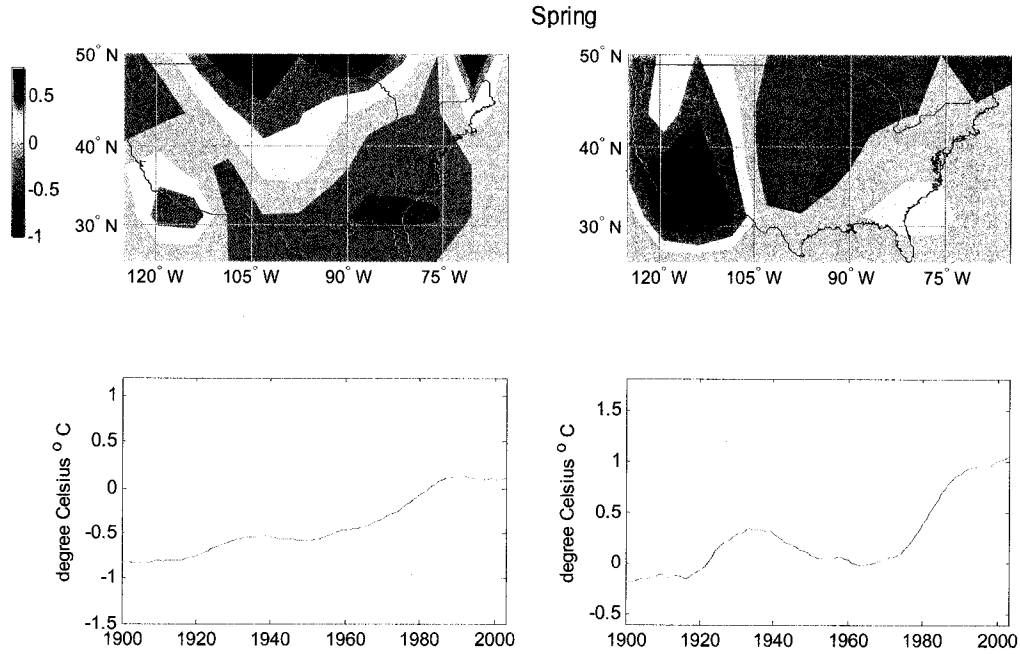

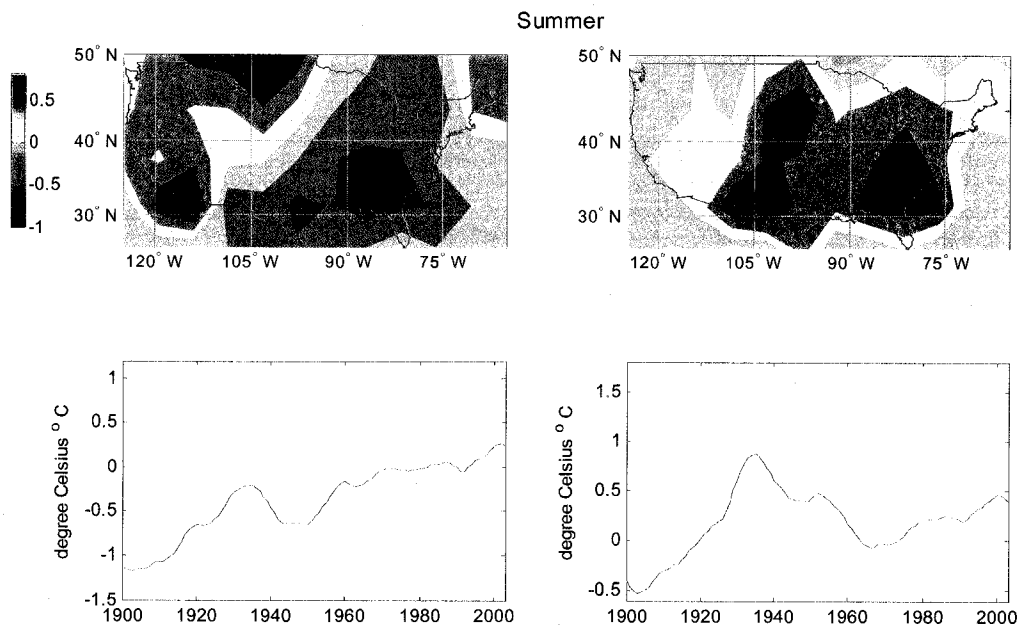

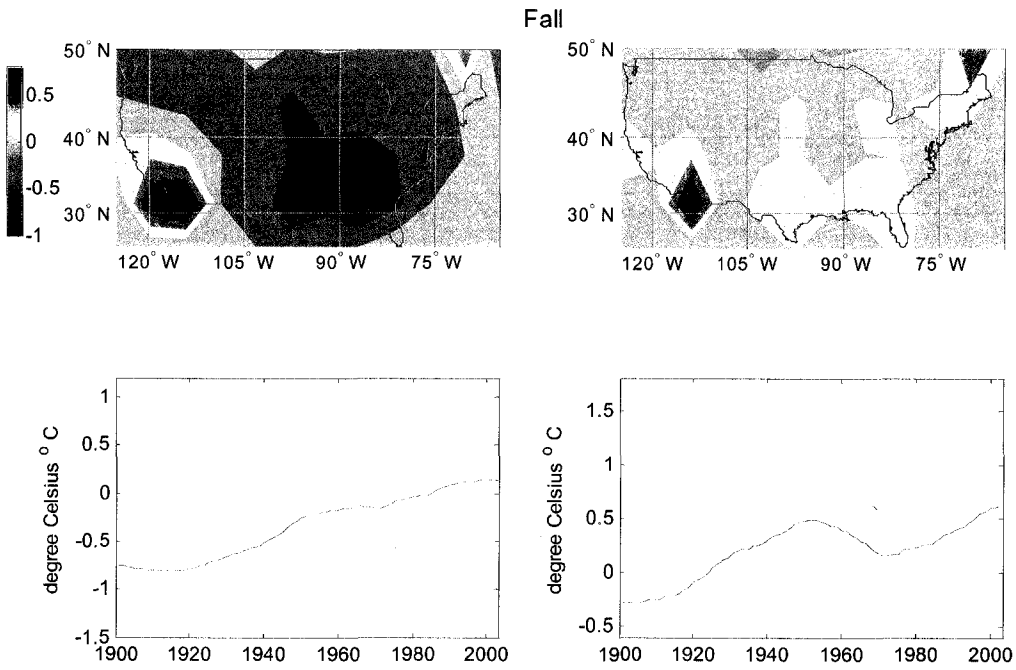

Figure 4.8. The principal spatial and temporal patterns of trends of all four seasons. Left column: the first dynamic factor (lower left panel) and the associated factor loading (upper left panel); right column: the second dynamic factor (lower right panel) and the associated factor loading (upper right panel).

The nearly monotonic factor is the strongest factor in all other seasons except winter. This factor is strong in the far northern US region in the winter season although the variations in this season are dominated by an interdecadal oscillation. This factor is confined to the Northern regions along the border of the US and Canada and a small region in the south California region in winter, spreads southward during spring, and turns into the strongest signal in the summer season in the northern and western part of

the US region. The cooling trends are very weak in winter and spring; they appear only at the southeastern corner of the region in both seasons. These trends become stronger in summer at the southeastern region and appear to be strongest in the fall in most of the central and eastern regions.

To study the impact of the inter-decadal factors found in the winter and summer seasons, we remove these two factors from these two seasons of data and combine the remaining data with the spring and fall seasonal data to form new annual temperature data. We perform dynamic factor analysis on this new annual data. The first two stochastic factors and the associated pattern are displayed in Figure 4.9. The first dynamic factor is the monotonic increasing trend, which explains 75% of the total variation in the stochastic trends alone. This trend does not contain the inter-decadal oscillation, as did the second dynamic trends in the study of the original SATs. The associated spatial pattern shows this factor is strong in the northern and western regions (the yellow-to-red-shaded regions in the upper left panel of Figure 4.9), while the southeastern region displays a cooling trend (the blue-shaded regions in the upper left panel of Figure 4.9). The cooling trend in the southeastern region may be due to the excessive sulfates in the air (Yu et al., 2001). Sulfates can scatter the sun's light before it reaches the Earth's surface. Without the reduced irradiance from the sun, the Earth's surface will cool off. Therefore, this trend can be viewed as the fingerprint of anthropologically-induced climate change in this region since the effect of the inter-decadal oscillation is removed from this factor.

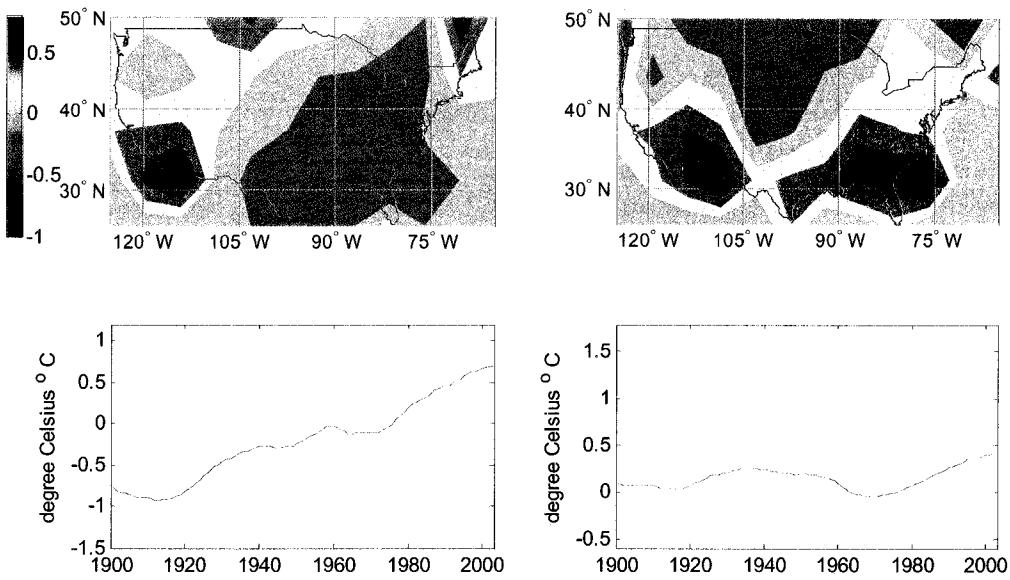

Figure 4.9. The principal spatial and temporal patterns of the stochastic trends of the SAT after the inter-decadal oscillation in the winter and summer seasons being removed. Left column: the first dynamic factor (lower left panel) and the associated factor loading (upper left panel); right column: the second dynamic factor (lower right panel) and the associated factor loading (upper right panel).

To discover the effect of the inter-decadal factors on the area-averaged SATs, we add the inter-decadal factors in the winter and summer seasons and form these annual and area mean. The result is plotted in Figure 4.10 with the area-averaged SATs and the area-

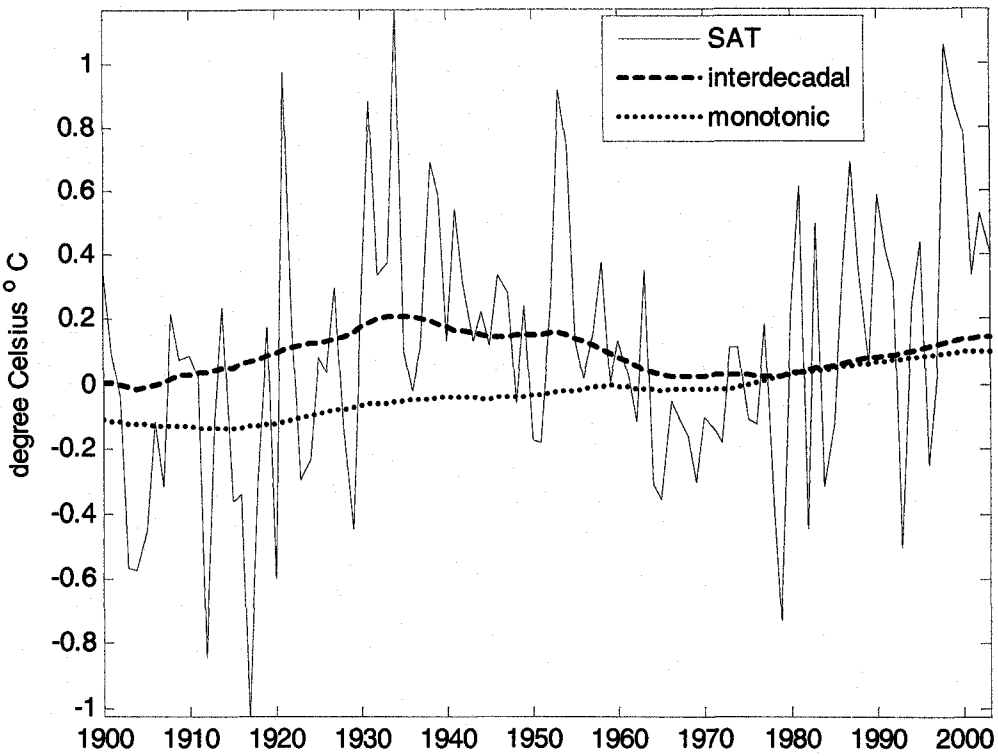

Figure 4.10. The area-averaged surface temperature time series (thin line) over the US region, the area-averaged inter-decadal factors in the winter and summer seasons (thick dash line), and the area-averaged monotonic stochastic factor from the annual temperature data with the inter-decadal oscillation removed (thick dot line).

averaged monotonic trends from the new annual data. The inter-decadal factors in the winter and summer seasons explain most of the inter-decadal oscillations in the first part of the twentieth century. This result suggests that the long-term oscillations in the area-averaged temperature time series during that period are associated mainly with inter-decadal oscillations in the southeastern part and may be attributed to natural forcing.

Although the monotonic trend appears to be a decreasing trend in the southeastern part of this region, the area-weighted spatial average increases consistently over the past century. This finding suggests the monotonic trend also contributes to the warming trend in the first half of the twentieth century in the area-weighted SATs. This warming trend may be associated with an anthropogenic source. Therefore, the warming trend during the first half-twentieth century may have different origins in different parts of this region.

4.5 Conclusions

The regional climate change detection and attribution in the contiguous US region is problematic because the behavior of the observed SATs in the southeast region is unusual and the model simulations of the temperature time series have a large discrepancy with the observed data in this region. In this chapter, we have applied the dynamic factor analysis to the observed monthly and seasonal temperature data in the contiguous United States region from the years 1900 to 2003. In each case, we have obtained two major common stochastic trends and their associated spatial patterns. For annual temperature data, the two stochastic trends agree with the results from previous studies; however, the monotonic factor and the inter-decadal factor are not well separated. The dynamic factor analysis of the seasonal data provides a clean separation of the monotonic trend and the inter-decadal factor in the winter and summer seasons. The inter-decadal factor is the strongest factor in winter and explains 82 percent of the

variances in the long-term trends alone. This factor is also strong and pervasive in the summer season.

After the inter-decadal factors are removed from the winter and summer data, the new annual temperature data has a strong nearly-monotonic stochastic factor, which alone explains 75 percent of variations in the stochastic trends of the new annual time series. After the inter-decadal factors are removed from the data, the area-averaged stochastic factor still shows an increasing trend during the first half of the twentieth century. This result indicates the warming in this region during the first part of the twentieth century may have more than one source of origin. The warming trend during this period in the southeastern region may be attributed to the inter-decadal oscillations mainly in the winter and summer seasons, while the monotonic increasing trend is the major factor in the northern and western regions where the inter-decadal oscillations have little effect. The inter-decadal factor is likely to originate from natural forcing such as the North Atlantic Oscillation. This result suggests that for model developers, the effect of natural forcings at the southeastern US regions in the winter and summer seasons are crucial for simulating the temperature time series and attributing the source of warming in the first part of the twentieth century.

Chapter 5

Area-integrated Standardized Precipitation Index Analysis and its Application to Southern Africa Drought Monitoring

5.1 Introduction

For the last fifteen years (1990-2005), many countries in southern Africa have experienced erratic rainfall that has threatened millions of people with famine. For most of these countries, agriculture is rain-fed, and food productivity depends on the intra-seasonal variability of rainfall. The predominance of rain-fed agriculture and the regions over-dependency on maize, a crop with a high water demand, makes southern Africa particularly vulnerable to changes in inter-annual and intra-seasonal rainfall. To minimize the impacts of inter-annual rainfall variability on agriculture, considerable efforts have been made to improve the accuracy of the predicted seasonal rainfall (Mwale et al., 2004). However, intra-seasonal atmospheric variations are very unpredictable, and the heterogeneity of rainfall statistics in space and time makes it difficult to disaggregate accurately seasonal rainfall into intra-seasonal quantities. Nevertheless, the gap between seasonal and intra-seasonal rainfall variability needs to be closed so that the progression of the rainy season at various time scales can be monitored. Doing so would help enhance the resiliency of agriculture to intra-seasonal rainfall variability. For example, Maphosa

(1994) observed that, although low rainfall caused the 1991/92 droughts in Zimbabwe, the progressive but less severe droughts of the previous two years had exacerbated the effects of the 1991/92 droughts. The Zimbabwe experience clearly calls for the progressive or incremental adaptation of agriculture to inter- and intra-seasonal rainfall variations. Adaptation options may include planting different crops or crop varieties or starting irrigation projects. Hulme (1994) has also emphasized the need to monitor continuously rainfall variability on the regional scale in southern Africa, showing that during the periods 1930-1960 and 1960-1990, a decrease of 10% in the mid-summer (January-February) rainfall occurred in Botswana, Zimbabwe, South Africa and southern Zambia. That study has recently been indirectly confirmed by Fanta et al. (2001), who showed that after 1974, the runoff for the majority of rivers in the region declined. Mwale et al. (2004) showed that the decreases in seasonal rainfall are consistent with large-scale changes in the sea surface temperature (SST) of the surrounding Indian and Atlantic Oceans.

The widespread famines culminating from a combination of interannual rainfall decreases and erratic intra-seasonal rainfall variability could mean that agricultural droughts (short-term low precipitation), meteorological droughts (prolonged low precipitation) and hydrological droughts (prolonged low streamflow and groundwater levels) are a dominant and widespread feature of countries in this part of Africa. Therefore, the magnitude of these droughts over the last fifty years must be quantified to determine if they are increasing in magnitude. Their geographical distribution must also

be determined so that the regions most vulnerable to droughts can be mapped. Mapping areas vulnerable to drought could help shift regional priorities.

The monitoring and quantifying of droughts can be accomplished by using one of the many available drought indices, among which the Palmer drought index (PDI) (Palmer, 1965) and the standardized precipitation index (SPI) (McKee et al., 1993) are the most widely used modern drought indices. The calculation of the PDI can be difficult since this calculation requires an empirical water balance model where it accounts for factors including the precipitation, evapotranspiration, soil-moisture loss and recharge, and runoff. Concerns have been raised about the model's assumptions and the regional factors. Compared to the PDI, the SPI is a probability index based solely on the precipitation data and can be interpreted easily. Like the PDI, the SPI has the ability to address simultaneously the drought phenomena at different time scales and can therefore be used to identify emerging and persistent droughts. The SPI has been shown to be better than the PDI for comparing droughts from region to region (Heim, 2002). SPI has been successfully used in various parts of the world including southern Africa to analyze and monitor various forms of droughts (Guttman 1998; Sonmeze et al., 2005; Rouault and Richard, 2005), while the PDI has been mainly used in the United States. The SPI is therefore used in this study.

Using the SPI, Rouault and Richard (2005) analyzed the intensity and spatial extent of droughts in southern Africa and noted that the southern Africa rainfall regime is complex. Instead of using individual index values to identify the drought magnitudes

throughout southern Africa, this present study uses the empirical orthogonal functions (EOF) of gridded areally integrated standardized precipitation index (ASPI) to establish the spatial patterns of the droughts. Due to the complexity of the rainfall regime, the occurrences of droughts are not expected to be the same everywhere. Hence, the above analyses have the advantage of establishing not only the temporal and frequency patterns of the droughts' variation, but also their spatial patterns or sub-regions. Although it is difficult to identify precisely the initiation and termination of droughts, this study attempts to establish the actual rainfall quantities, transformed from the SPI values, at which point a drought could be considered to have occurred. Drought is considered to have occurred for each month when the rainfall quantities at each time scale fell below that month's "reference" rainfall. The reference rainfall is the average cumulative rainfall for each time scale established by using the 1900-1995 data. To provide an idea of the cumulative effects of the droughts at various time scales in the region, this study further established the amounts of rainfall that would be required to offset these droughts. The time scales used in the analyses ranges from 3 to 24 months.

This chapter is organized as follows. The data used in the analysis are presented in section 5.2. The methodology is presented in section 5.3. Section 5.4 presents the results and discussion. The conclusions are presented in section 5.5.

5.2 Data

Monthly rainfall data (1900-1995) from 60 grid boxes at a resolution of 2.5° ×3.75° latitude and longitude were extracted for southern Africa from 10°S-35°S, 15°E-40°E (Figure 5.1). The rainfall data are part of a monthly precipitation dataset constructed by using the Thiessen polygon for global land areas from 1900 to 1998 and provided by the UK meteorological office. This data set was constructed from station data and interpolated onto 2.5°×3.75° grids. Thiessen Polygon weights were used to average the gauge data within each gridbox. Although the rainfall data between 1901 and 1945 are scarce for some countries in this part of the world, the analysis results obtained by using the 1901-1995 data are very similar to the results from using the 1950-1995 data. Hence, in this study, the 1901-1995 period is used for analysis.

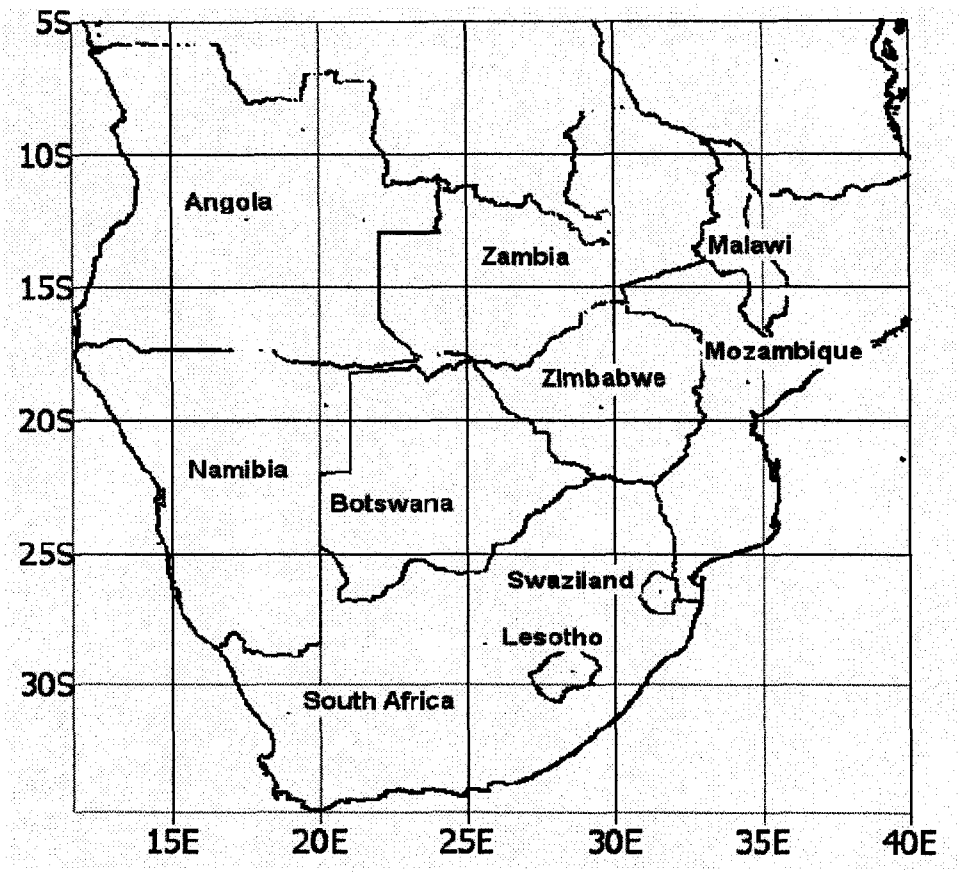

Figure 5.1. The study location consisting of ten countries in southern Africa

5.3. Methodology

5.3.1 Standardized Precipitation Index

The SPI is calculated by using long records of precipitation (Guttman, 1999), so that the index is computed over a climatologically long-term mean. According to McKee et al., (1993), the SPI index is less than –2 for extremely dry conditions, between -1.50 and -1.99 for severely dry conditions, -1.0 and -1.49 for moderately dry conditions, and –0.99 and 0.99 for near normal conditions. A drought begins when the SPI is below the normal rainfall conditions, i.e., at -1 or less. Based on the normal distribution, each of

these categories can be associated with cumulative frequencies of less than 2.3%, 2.3-6.7%, 6.8-15.9% and 16-50%, respectively (McKee et al., 1993). The wet conditions are described similarly. Hence, the SPI can also be used to monitor wet conditions, providing early warning for impending above-normal rainfall conditions.

The SPI values are obtained from the probability distribution function (PDF) of the rainfall at a given time scale and the PDF of the standard normal distribution. Variance probability functions can be used for precipitation data. In our study, the rainfall data are fitted to the gamma distribution, as it has been found to fit the precipitation distribution quite well for Alberta precipitation data (Yin, 2006), and it provides a good approximation of the southern Africa rainfall distribution in our calculation. The fitted gamma distribution is then transformed into a standard normal distribution according to the principle of equal probability.

To compute the SPI, monthly rainfall data are first accumulated by using a moving window of 3 months or more. The range of time scales considered in this study is 3 to 24 months. Then the cumulated rainfall data are fitted to a 2-parameter-gamma distribution whose parameters are estimated by using the maximum likelihood method (Thom, 1958). The probability density function of the gamma distribution is

$$f(x \mid a,b) = \frac{1}{b^a \Gamma(a)} x^{a-1} e^{-\frac{x}{b}} \quad \text{for } x > 0,$$

where $a > 0$ is the shape parameter, b>0 is a scale parameter, and

$$\Gamma(a) = \int_0^\infty y^{\alpha-1} e^{-y} dy$$

is the gamma function. There are no closed-form solutions to the maximum likelihood function for the two-parameter gamma distribution. The numerical optimization using the moment estimators as the initial values is used to obtain the maximum likelihood estimators. After estimating the parameters, the probability of each rainfall observation is calculated by using the gamma cumulative distribution function as follows:

$$F(x \mid a,b) = \int_0^x f(x)dx = \frac{1}{b^a \Gamma(a)} \int_0^x t^{a-1} e^{\frac{t}{b}} dt .$$

Since the monthly rainfall in some regions has many zero values, the gamma function is revised according to the following mixture model,

$$H(x) = q + (1-q)F(x),$$

where q is the probability of a zero and is calculated by using the ratio of the number of zeros to the total number of observations. In this step, the precipitation at a certain location is described as a cumulative probability function, and the probability of the amount of the precipitation at this location can be identified by using this function.

Since the mean and variation of the fitted gamma distribution can differ from place to place, it is inconvenient to compare the drought events at different places. To compare the rainfall events in different areas, the precipitation X in the cumulative probability gamma function is mapped into a new variable Y with a standard normal distribution with mean, $\mu = 0$ and variance $\sigma = 1$ by using the following criterion:

$$P(x \le X) = P(y \le Y);$$

i.e., the probability of the precipitation under or equal to a certain amount X equals the probability of the new normally-distributed variable under or equal to a certain amount Y. The resulting values Y are the standardized precipitation indices or SPI.

The magnitude of the drought at a point is defined as the integration of the SPI in a drought period, I_D, which starts from the second negative SPI less than or equal to –1.0 and ends at the first positive SPI. The drought magnitude at one location over the period I_D is defined as

$$M_D(\vec{r}) = -\int_{I_D} SPI(\vec{r},t)dt \approx -\sum_{m \in I_D} SPI(\vec{r},m) \text{ if } M_D(\vec{r}) \ge 1; \text{ otherwise, } M_D(\vec{r}) = 0.$$

The drought magnitude over a region, i.e., the area-integrated SPI (ASPI), is defined as

$$S_D = \int_{\Omega} M_D(\vec{r})d\Omega,$$

where Ω denotes the investigation region. If the spatial integration is done for the gridded data, then

$$S_D = \int_{\Omega} M_D(\vec{r})d\Omega \approx \sum_{j \in \Omega} M_D(j)\cos(\phi_j),$$

where ϕ_j is the latitude (in radians) of a grid point j or the centroid of a grid box j.

By using the 1900-1995 monthly data, the rainfall quantities corresponding to an SPI of 0 (i.e., the mean rainfall) and SPI of -1 for each month and each grid box are computed. In this analysis, the rainfalls corresponding to an SPI of -1 are called the threshold rainfall. The threshold rainfall is the amount of rainfall, below which drought is considered to occur. For each grid box and month, the difference between the rainfall quantity corresponding to the threshold SPI and the SPI for that month is taken as the

rainfall deficit. The amount of rainfall greater than the deficit is required to offset the drought for that month. The total rainfall deficit for the period I_D is computed as follows:

$$TDef(r,t) = \int_D Def(r,t)dt \approx \sum_{m \in I_D} Def(\vec{r},m),$$

where *TDef(r,t)* is the total rainfall deficit for the grid box.

5.4 Results and discussion

5.4.1 Fitting the Gamma distribution function to the rainfall data

The rainfall data for each grid location are fitted to the gamma distribution. Figure 5.2 shows an example of the fitted cumulative gamma distribution with an empirical cumulative probability for the rainfall during the 3-months time scale for the months of October to March (i.e., the summer rainfall season), using the rainfall data obtained from Angola (i.e., 15°E, 10°S). The smooth curve is the cumulative probability of the fitted gamma distribution, while the solid circles are the empirical cumulative distribution. This figure clearly shows that the gamma distribution reliably represents the rainfall distribution of Angola. Data from other locations within the region are similarly fitted with the Gamma distribution.

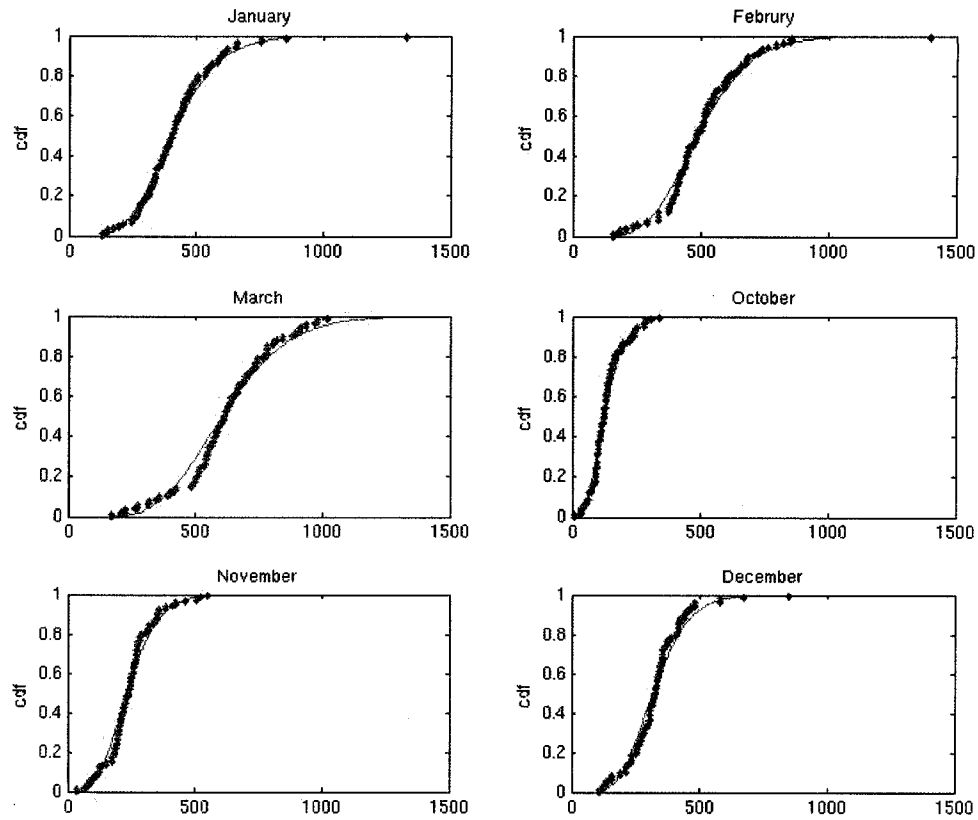

Figure 5.2. An example of fitted Gamma distribution to 3-month rainfall totals obtained from Angola (i.e., 15°E, 10°S). The smooth red curve is the cumulative probability of the fitted Gamma distribution, and the blue solid circles are the empirical cumulative distribution.

5.4.2 Geographical distribution of drought occurrence

Figure 5.3 shows the percentage of drought occurrence in each category, throughout southern Africa, by using the 3-month SPI values. The occurrence of droughts in each category is computed by taking the ratio of droughts in each category to the total number of droughts. This figure shows that more near normal rainfall events (i.e., 40% of

the time) occurred in the northwestern areas of the region (i.e., Angola, northern Namibia and northern Zambia) than in other areas in this region. Elsewhere in the region, near normal events occurred 36% of the time. This finding shows that northwestern areas of the region experienced fewer droughts than the rest of the region for the same period. Southern Africa experiences moderate drought magnitudes 7 to 10% of the time. Figure 5.3 (b) shows that Angola, Botswana, Namibia and the northern sections of Zambia experience moderate droughts 7% of the time, while southern Zambia, South Africa, Zimbabwe, Malawi and Mozambique experience moderate droughts 9 to 10% of the time. The spatial pattern of the occurrence of moderate droughts is the same as that for the occurrence of severe droughts in the region. Finally, except in Swaziland and Lesotho, where extreme droughts are experienced up to 3% of the time, the rest of southern Africa experiences extreme droughts 2% of the time. Figure 5.3 shows that the geographical distribution of drought occurrence in southern Africa is that expected from a normalized gamma distribution, i.e., less than 2.3%, 2.3-6.7%, 6.8-15.9% and 16-50% for extreme, severe, moderate and normal droughts, respectively.

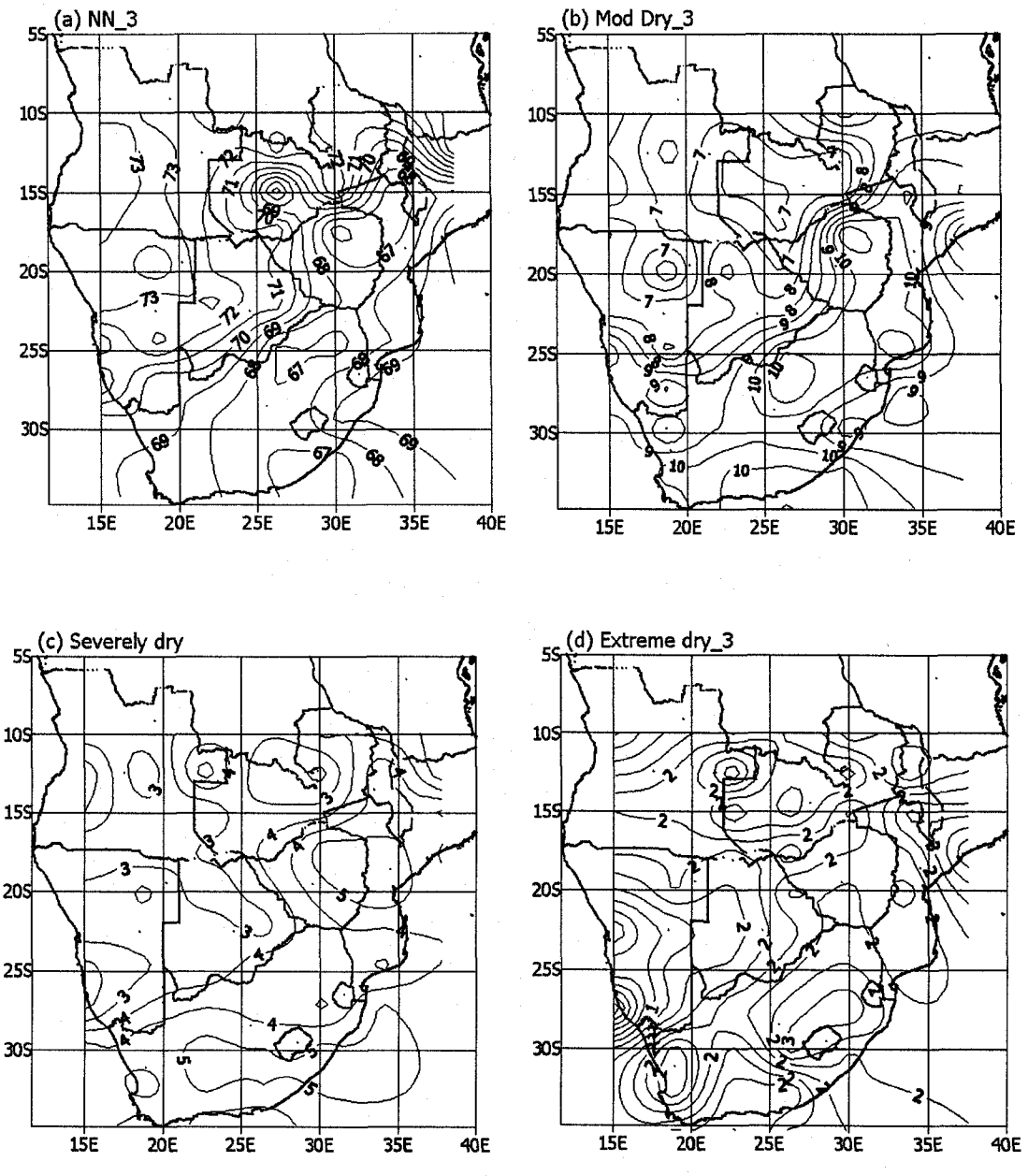

Figure 5.3. The percentage occurrence of droughts over the southern Africa region, (a) near normal, (b) moderately drought, (c) severe drought and (d) extreme drought.

5.4.3 Magnitudes of the droughts

5.4.3.1 Temporal patterns

Figure 5.4 shows the temporal patterns of the regionally integrated drought magnitudes, or the area-integrated SPI (i.e., ASPI) computed by using the 3-, 6-, 12-, and 24-month time scales. This figure shows that the drought magnitudes are smaller during the periods 1934-1942, 1950-1963 and 1974-1980 than during the periods 1922-1924, 1943-1950, 1964-1974, 1980-1984 and 1990-1995. During the latter periods, southern Africa experienced the largest drought events in 1933, 1946, 1949, 1964, 1970, 1973, 1984, 1992 and 1995.

Figure 5.4(b) shows that between 1980 and 1995, the magnitude of droughts at the 12- and 24-month time scales generally increased, compared to the droughts at the 3- and 6-month time scales. This finding shows that after 1980, long-term droughts (i.e. meteorological droughts) became much more dominant.

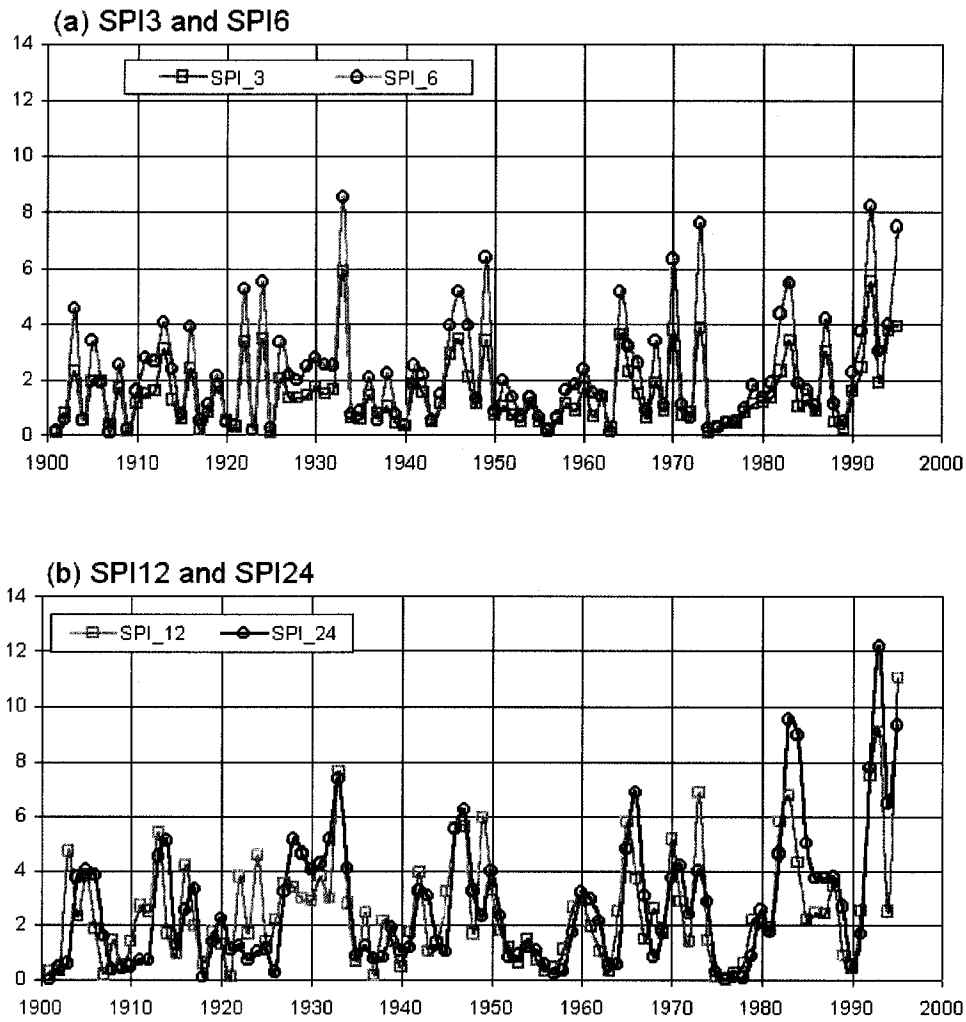

Figure 5.4. The temporal pattern of the regionally averaged SPI (ASPI) (a) 3 and 6 months, (b) 12 and 24 months.

5.4.3.2 Spatial Patterns

The geographical distributions of drought magnitudes are made by correlating the time series of the ASPI at each of the four time scales with the drought magnitudes at each of the 60 grid locations. The correlations are made to show how representative the

ASPI is to the individual drought magnitudes in the region. At all the time scales, the spatial patterns of the drought magnitudes look similar to one other. An example of drought magnitudes, using the 3-month time scale, is shown in Figure 5.5, which shows that the ASPI accounted for between 1 and 36% (i.e., correlations of 0.1 - 0.60) of the gridded drought magnitude variance. The correlation is the highest in the centre of the region and decreases outwards in a circular fashion. The correlation decreases most rapidly towards the north, northwest and the southern portions of the subcontinent.

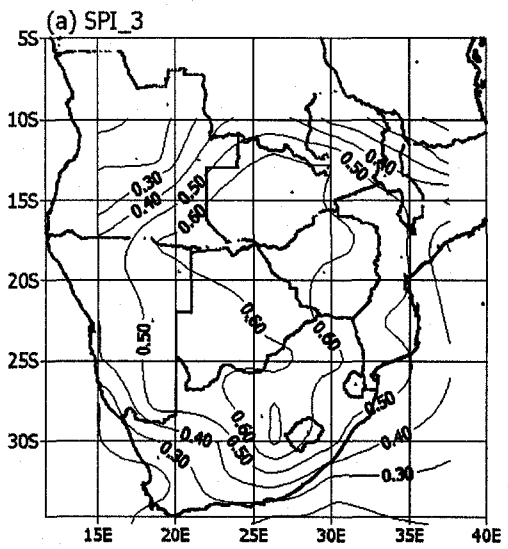

Figure 5.5. The correlation between the integrated SPI and the gridded SPI over southern Africa, obtained by using the 3-month SPI.

The decrease in the explained variance of the drought magnitudes from the centre of southern Africa means that some variations of the drought magnitudes cannot be

explained by the ASPI. Hence, the patterns of the drought magnitudes are further explored by using the empirical orthogonal function analysis (EOF). EOF analysis (or the principal component analysis) is used to summarize the variance information among several random variables. In this study, this analysis is performed on the N-by-T matrix of the drought magnitude anomalies,

$$X = \begin{bmatrix} x_1(1) & x_1(2) & \cdots & x_1(T) \\ x_2(1) & x_2(2) & \cdots & x_2(T) \\ \cdots & \cdots & \cdots & \cdots \\ x_N(1) & x_N(2) & \cdots & x_N(T) \end{bmatrix},$$

where the entries are calculated through $x_i(t) = M_D(r_i,t) - \mu_i$ for the location $i = 1,\cdots,N$ and the time $t = 1,\cdots,T$. Here, $M_D(r_i,t)$ is the drought magnitude at location i and time t and μ_i is the mean drought magnitude for the location i. The eigenvectors $\vec{e}_k$ of the covariance matrix

$$C = XX',$$

$k = 1,\cdots,N$, sorted according the descending value of eigenvalues are the EOFs. The principal components P are then calculated as

$$P = [\vec{e}_1,\vec{e}_2,\cdots,\vec{e}_N]^T X,$$

where the l-th principal component is

$$P_l(t) = \sum_{k=1}^{N} x_k(t) e_l(k).$$

The principal components can also be projected in space through correlation with the gridded drought magnitudes, so that their spatial distribution can be analyzed.

At the four time scales, the first three PCs accounted for a total of 40%, 43%, 40% and 42% of the spatial variations of regional drought, for the 3, 6, 12 and 24-month time scales, respectively. All the patterns at different time scales look similar, and for brevity, only the patterns associated with the 3-month time scale are shown in Figure 5.6. For the 3-month time scale, the leading mode (i.e., PC1) accounts for about 24.1% of the total drought variance and depicts a pattern of drought similar to that of Figure 5.5. This PC accounts for up to 49% (i.e., a correlation of 0.7) of the drought variation in the region. PC2 accounts for 9.4% of the total drought variation and identified two regions, the Lake Malawi/eastern Zambia and western Namibia/Angola regions that exhibit an out-of-phase relationship. PC2 explains up to 25% of the gridded drought variation in the Lake Malawi area and up to 36% of the drought variation in the Namibia area. PC3 accounts for 7.0% of the total drought variation and identified northern southern Africa as being out of phase with the entire southern region of South Africa. PC3 is positively correlated to northern southern Africa (up to 25%) and negatively correlated to southern South Africa, (up to 16%).

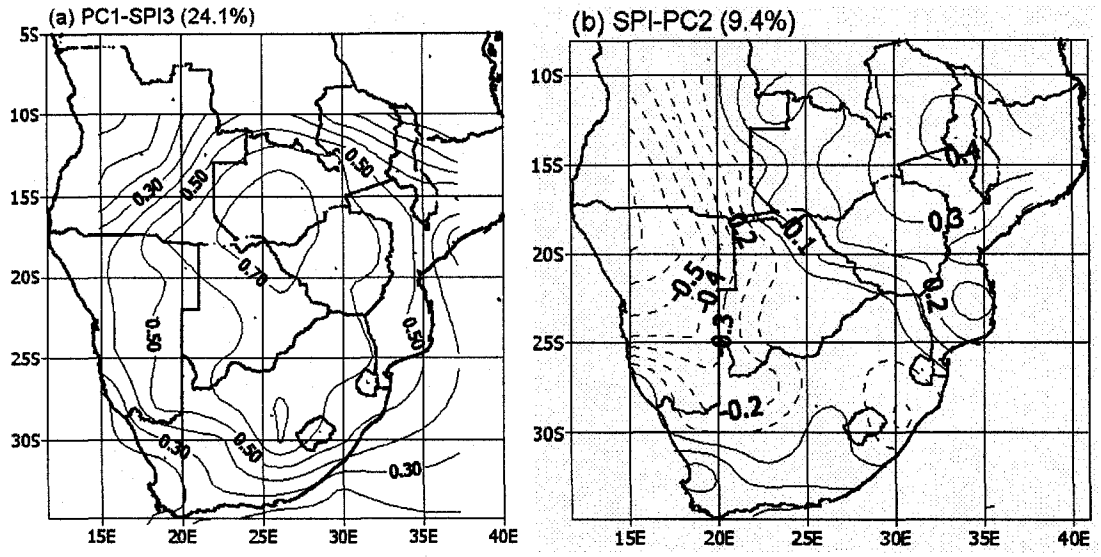

Figure 5.6. The spatial pattern of the PC1 and PC2 of the drought magnitudes computed by using the 3-month SPI. The percentages shown in brackets are the variances explained by each of the PCs.

The temporal patterns of the drought magnitude PCs at the 3- and 24-month time scales are shown in Figure 5.7. The temporal PC1 (see Figure 5.7(a)) shows a similarity to the regionally averaged drought pattern (the ASPI of Figure 5.4(a)) and hence is not discussed further. PC2, Figure 5.7(b), shows that the Malawi/eastern Zambia region experienced no drought in 1933, 1949, the mid-1960's, 1970 and 1984, when the rest of the southern Africa region experienced extreme droughts. However, during the period 1990-1995, the drought magnitude increased for the Malawi/eastern Zambia region. Hence, PC2 emphasizes that although the earlier droughts did not affect the Malawi/eastern Zambia region, the scenario changed after 1990 as droughts become

dominant in this region as well. At both the 3- and 24- month time scale, PC3 shows that the drought magnitudes generally decreased between 1900 and 1970 and increased after 1970 for the northern sections of southern Africa and vice versa for areas located south of southern Africa. This PC also shows that largest drought occurred in 1982. These PCs emphasize the fact that after 1970, the areas in northern southern Africa became drier compared to the areas south of South Africa, especially in the coastal areas.

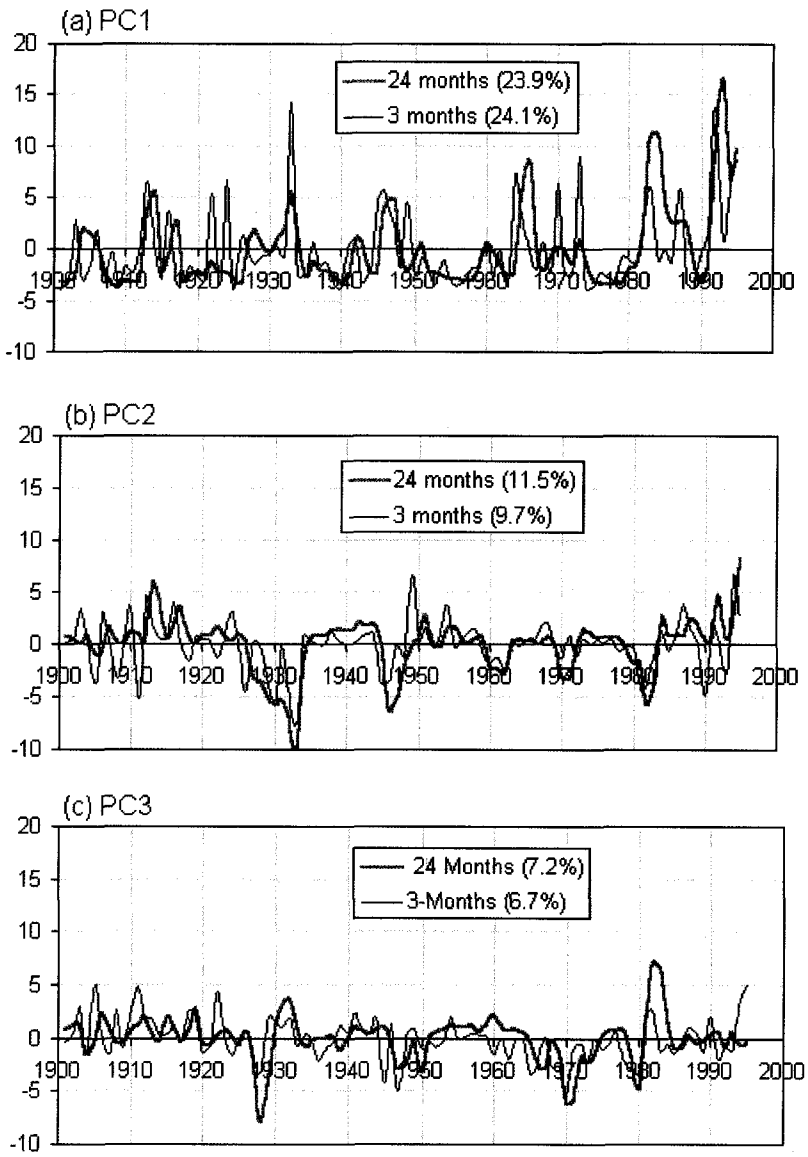

Figure 5.7. The temporal patterns of PC1, PC2 and PC3 computed by using the 3- and 24- month time scales. The percentages shown in brackets are the variances explained by each of the PCs.

5.4.4 Rainfall deficits

5.4.4.1 Temporal patterns

The regionally averaged amount of rainfall required to offset droughts (i.e., rainfall deficits) for the 3- and 6-month time scales is shown in Figure 5.8, which shows that, overall, rainfall is always needed to offset droughts somewhere in the region and that rainfall deficits have increased since 1980 (see Figure 5.8(b)). Figure 5.8(b), shows that the rainfall deficits at the 6-month time scale have increased after 1980. Similar increase is observed at the 12- and 24-months time scales (figures not shown), reaffirming that long-term droughts have been dominant after 1980.

Figure 5.9 shows a close up view of the 3-month rainfall deficits for some selected areas within southern Africa from October 1994 to November 1995 (i.e., one summer season). This figure shows that rainfall deficits of 70, 160, 60, 10 mm would be required to offset droughts in November, December, January and February, respectively, for the Angola/Zambia region, while in the Zimbabwe/Zambia region, rainfall deficits of 10 and 5 mm occurred in November and December. In the Botswana/Zimbabwe area, 55, 25, 40 and 40 mm of rainfall would be required to offset droughts from November through February, while in the northern South Africa/Swaziland region, 15, 85, 60 and 30 mm of rainfall would be required to offset droughts from December through April.

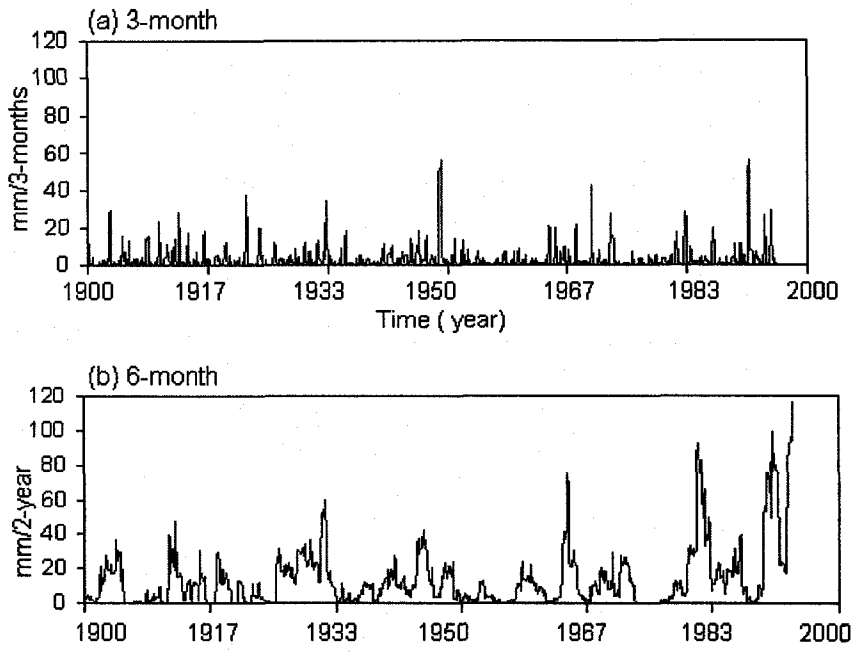

Figure 5.8. The regionally averaged rainfall deficits computed as the difference between the rainfall thresholds and the corresponding values of the SPI at each given time.

Figure 5.9 confirms that the magnitude and timing of these rainfall deficits differed from one location to the other. However, the effects of rainfall deficits are the same everywhere, because agriculture is rain-fed. A lack of rainfall in October-December means that either maize planting begins late or maize planted in anticipation of the rainfall season will be destroyed due to a lack of moisture and presence of the intense heat. A lack of the rain during the critical part of the rainfall season, i.e., January and February, means that crops planted in either October or November will die due to lack of moisture.

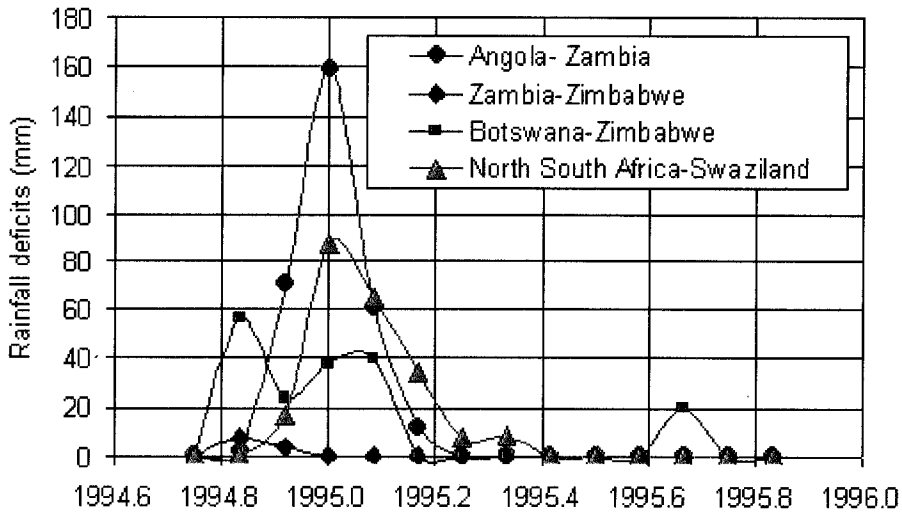

Figure 5.9. An example of the 3-month rainfall deficits from October 1994 to November 1995 for some selected areas of southern Africa.

Figure 5.10 shows the rainfall required to offset droughts at the 24-month time scale, from 1980 to 1995, for the same locations shown in Figure 5.9. This figure shows that meteorological droughts were dominant in most of southern Africa in the 1980's and 1990s. The largest of these droughts occurred in the northern half of the subcontinent (Figures 5.10(a)-(c)). The rainfall required to offset droughts averaged about 200-300mm, but up to 400mm was required during certain times. Figure 5.10 clearly shows that the persistency of the meteorological droughts during this period contributed to the hydrological droughts. The reduction of river levels, especially for catchments in the northern half of southern Africa (Fanta et al., 2001), supports this finding.

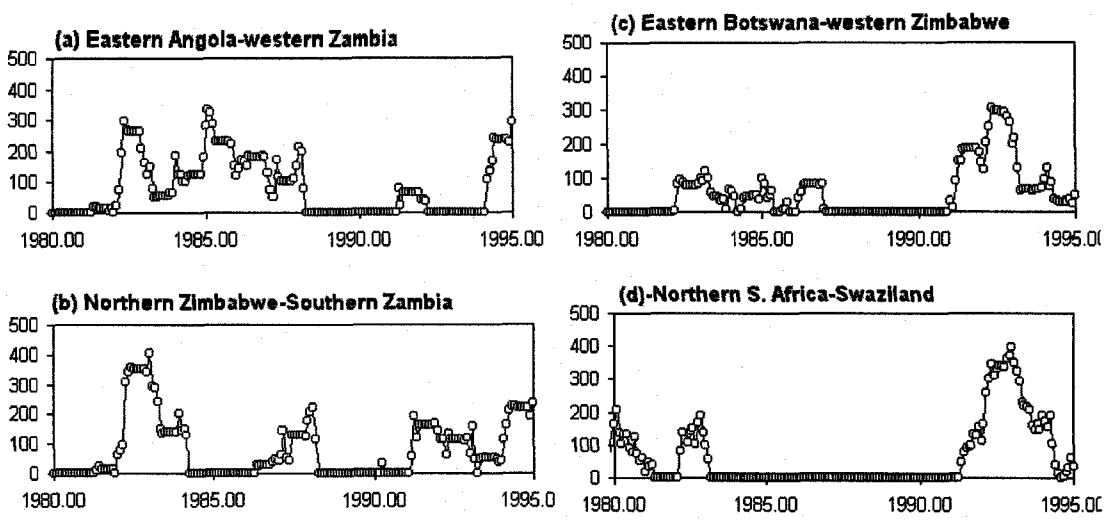

Figure 5.10. Examples of 24-month rainfall deficits for the selected areas of southern Africa as shown in Figure 5.9.

5.4.4.2 Spatial patterns

The correlation between the regional averaged rainfall deficits and each grid's rainfall deficit is shown in Figure 5.11. This figure appears the same whether rainfall deficits at the 3-month or 24-month time scales are used. The figure shows that the largest rainfall deficits occurred in the northern half of South Africa, Zimbabwe, Zambia and Botswana, northern Namibia and Mozambique. In these countries, the regional averaged rainfall deficits explained between 4 and 49% (significant correlations of 0.2-0.7) of the individual gridded rainfall deficits. The explained variance decreased towards the coastal areas and northern southern Africa. The largest explained variances of rainfall required to offset droughts are in the area between southern Zambia and Zimbabwe,

followed by northern South Africa, Botswana, Mozambique, eastern Angola and the southern half of Malawi.

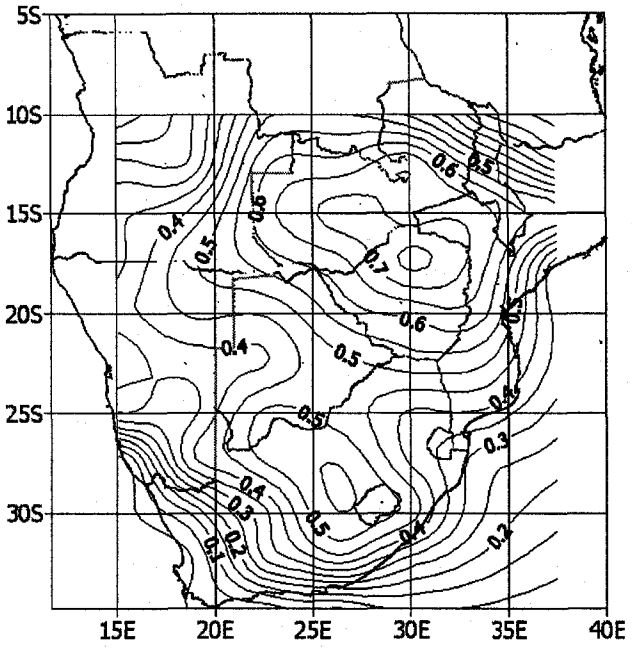

Figure 5.11. The spatial pattern of the regionally averaged rainfall deficits. The most intense deficits are found in the regions with correlations above 0.2 (statistically significant correlation with $n = 93$).

As Figure 5.11 shows, the areas most vulnerable to droughts may not necessarily follow the spatial distribution of rainfall deficits. Vulnerability to drought depends on many factors, such as the state of local economies, agricultural practices, and types of crops and crop varieties planted. Hence, although the magnitudes of the rainfall deficits are greater in northern South Africa, than in Zimbabwe and Malawi, the economies of the

latter countries are fragile, and the impacts of these droughts are felt more in these countries than in South Africa. Similarly, Botswana's economy is strong and hence more resilient to the effects of droughts. In recent years, large-scale famines occurred in Zimbabwe, Zambia, Malawi and Angola, countries with struggling economies. Since droughts are creeping phenomena, agriculture practices in these poor economies could be progressively adapted to the changing climate.

5.4.5 Spatial pattern of rainfall thresholds

Rainfall thresholds correspond to SPI values of -1, considered to be the point at which drought begins. This section determines the actual values of rainfall corresponding to the SPI reaches of -1 for the entire summer rainfall season. Hence, the rainfall values could be used to monitor the beginning or progression of drought at any given time and scale. For monitoring short-term droughts important for agriculture, rainfall values corresponding to the 3-months time scale are given.

Figure 5.12 shows the rainfall thresholds for each of the 60 grids at the 3-months time scale. This figure clearly shows that droughts begin at different rainfall thresholds over southern Africa. For the 3 months leading up to October, the threshold rainfall is highest along the eastern coast of South Africa (60-100 mm). This threshold is followed by that in the northern sections of the region (20-40 mm), and the threshold is lowest in the interior (5 mm). In contrast, the mean rainfall is 120-160 mm for the eastern coast of South Africa, 40-70 mm for northern sections, and between 10 and 20 mm for the

interior. By November, the regional rainfall thresholds are the same for the coastal regions of South Africa and the northern sections of South Africa (i.e. 60-160 mm), while in the central regions, the rainfall thresholds increase to 20 mm in the west and 80 mm in the northeast. The mean rainfall ranges from 80 to 260 mm for the eastern coast of South Africa, 100-220 mm for the northern sections, and 20 to 80 mm for the interior. In all of southern Africa the threshold rainfall is highest in January through March. During this time, the rainfall thresholds are between 250 and 750 mm in the northern sections of the region. On the other hand, in the southern portions of the region, the rainfall thresholds are between 100 and 350 mm. The largest rainfall thresholds are found in the eastern half of South Africa, Lesotho and Swaziland and smaller threshold are found in the western half of South Africa, Namibia and Botswana (Figure 5.3).

Although our dataset is averaged over 300 by 400 km, the threshold values may be used as a guide to evaluate the progression of any rainy season, especially for the northern areas of southern Africa that are most vulnerable to droughts. If these rainfall values are typical, crops that can survive rainfall for SPI values of between 0 and -0.99 cam be grown during times periods with below average rainfall. If these values are not typical, the threshold values may be re-computed by using station or observed data. Above all, this study has shown that the SPI or the area-integrated SPI could be used to monitor intra-seasonal rainfall variability and to supplement the seasonally predicted rainfall.

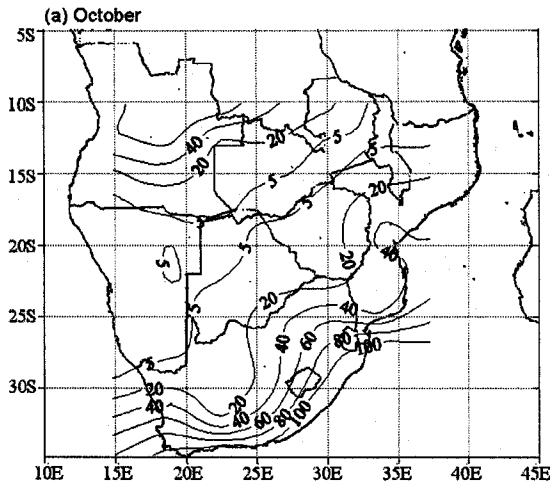

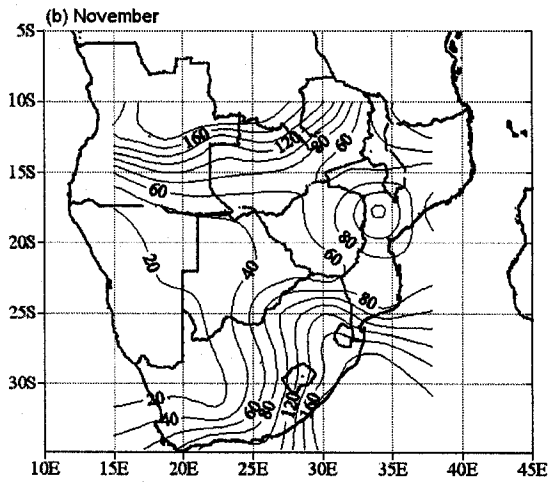

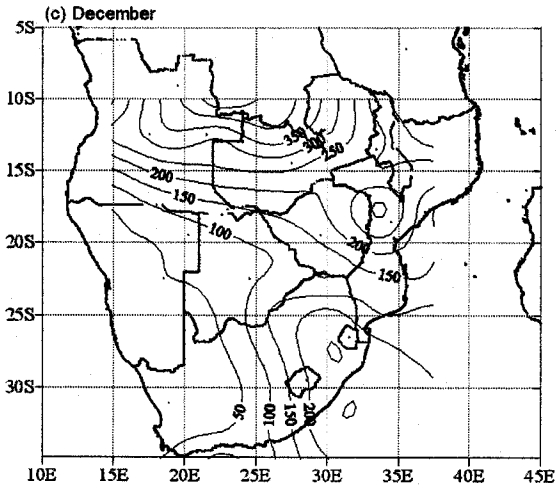

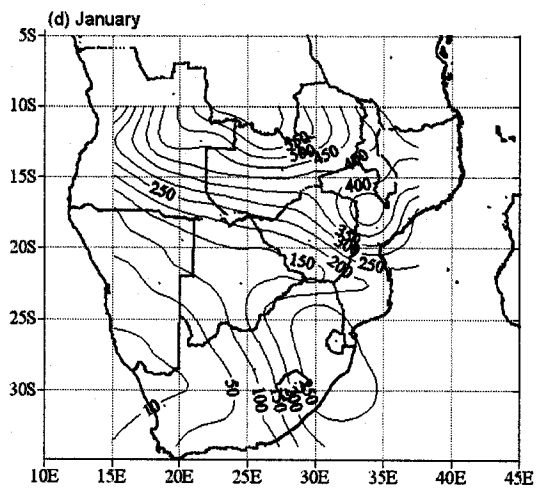

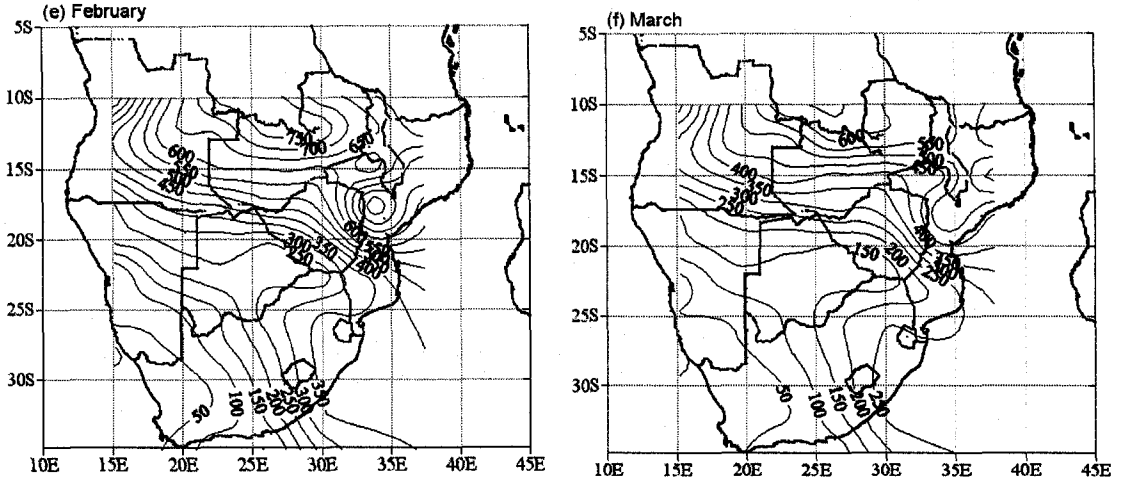

Figure 5.12. The 3-month rainfall totals that should occur up to (a) October, (b) November (c) December, (d) January, (e), February, and (f) March, to avoid the beginning of a drought anywhere in southern Africa. This amount of rainfall corresponds to an SPI of -1, called the "threshold rainfall."

5.5 Conclusions

By using between 3- and 24-month time scales, the standardized precipitation indices (SPI) have been computed from the monthly southern Africa precipitation data. The area integrated standardized precipitation index and empirical orthogonal functions of the gridded drought magnitudes have revealed three leading modes of spatial and temporal variability of droughts in southern Africa. The leading PC mode has shown that at all time steps, droughts and water deficits after 1980 were most intense in the southern half of Zambia, Zimbabwe, northern South Africa, Angola, northern Namibia and

Mozambique but generally decreased in the southern half of South Africa. The second PC mode has shown that before 1980, Malawi (Namibia/Angola) experienced wet years when the whole region experienced droughts, while after the 1980s, Malawi experienced droughts like those in every other country in the region. This mode also emphasized the fact that the droughts of the 1990-1995 period were more intense for the Malawi region than for the Namibia/Angola region. The third PC has shown generally that northern southern Africa became drier after 1970 than in the southern portions of the subcontinent.

Between 1990 and 2005, the magnitude of droughts and rainfall deficits at the 12- and 24-month time scales increased considerably compared to the drought magnitudes at the 3- and 6-month time scales, showing that after 1990, meteorological and hydrological droughts became dominant.

It has also been observed that the January-March rainfall was found to be the most critical part of the rainy season. However, due to the agriculture practices in the region, a lack of rainfall in other months such as November and December can also cause crop failures and famines in the region.

Effective drought-monitoring systems and reliable drought-monitoring schemes such as the use of ASPI are required in most countries in southern Africa to supplement seasonal rainfall predictions, properly assess drought severity and predict future drought events and the duration of current events. The use of agriculture practices such as changes in crops or crop varieties is also recommended for most areas of this region.

Chapter 6
Conclusions and Future Work

6.1 Summary and conclusions

The temporal variability of measurable time series (e.g., SAT and precipitation) contains valuable information about the past and present climate. These time series contain a complicated structure over different time scales in connection to different sources of weather systems and dynamics. Non-stationarity and stationarity are concepts in random processes characterizing the stability of the mean of time series. In general, the stationary time series is associated with a physical system dominated by negative feedbacks, and thus, the mean of the time series does not deviate much from a constant value. On the contrary, the mean of a non-stationary process will not revert to the initial value. This thesis analyzed daily and monthly SATs for the degree of stationarity from monthly to decadal temporal scales by using novel concepts of the non-stationary annual cycle. The non-stationary trends and the associated spatial patterns in monthly and annual SATs have also been studied for evidence of anthropogenically induced climatic change. This thesis has also derived the spatial patterns associated with the SPI index in precipitation data.

Chapter 2 used the EMD method to filter a non-stationary annual cycle (NAC) from daily SAT data from January 1, 1946 to December 31, 2000 at ten land stations in

North America. The sifting process is robust with respect to the length of the observed data and the end conditions of the EMD method. The NAC was compared with the commonly used fixed annual cycle (e.g., the thirty-year-mean annual cycle). The comparison of the NAC and TAC in spectral space indicated that the NAC is a cleaner filter for the annual cycle than the TAC.

Chapter 3 studied the degree of stationarity in the anomalies of fixed and non-stationary annual cycle in daily SATs at ten land stations from December 1, 1945 to November 30, 2000. Many methods can be used to obtain non-stationary annual cycles with time-varying amplitudes and phases, among which the EMD NAC and the piecewise trigonometric functions were studied in this chapter. The new findings in Chapter 3 included the following:

1. The amplitude of the non-stationary annual cycles is decreasing, and the phase of the annual cycle is increasing at most stations during the time period we studied, especially for those at the high-latitude. This finding shows that climate change occurs not only in the commonly studied mean level, but also in the amplitude and phase of the annual cycle.
2. The long-memory properties at time scales from months to a decade in daily SAT anomalies were found to occur because of the varying annual cycles. The removal of a fixed annual cycle from data may generate a slow-varying component in the anomalies and thus induce a long-memory in the time scales longer than three months. DFA analysis showed the EMD annual cycle and

the non-stationary annual cycle removed the long-range dependency of scale of more than three months from the daily SATs.

3. The statistical properties of the anomalies from the fixed annual cycle, EMD annual cycle, and the non-stationary piecewise trigonometric annual cycle were compared in this study. The anomalies from the annual cycles displayed strong short-range dependency and nonlinearity. The nonlinear AR(3) model was used to model such phenomenon in the daily SATs at the ten stations we studied. The climate noise was shown to be independent or to have very weak dependence over the time scale of less than three months. For the time scale of over three months, the climate noise displayed anti-persistency for both the EMD anomaly and the anomaly from the non-stationary piecewise trigonometric annual cycle.

Therefore, while the anomalies of the non-stationary annual cycles displayed strong anti-persistency at time scales of less than a decade, the climatic change could still be detected from the mean, amplitude, and the phase of the non-stationary annual cycle. The time scales used for detecting climatic change should be longer than a decadal scale.

Chapter 4 aimed at separating the climate change signal directly from data. The problem of regional climate change detection and attribution in the contiguous US region was attempted since the unusual behavior of the observed SATs in the southeast part of this region and that the model simulations of the temperature time series have large discrepancies with the observed data in this region. Unlike the previous studies which

used linear trends or model generated signals as climate change signals, the non-stationary stochastic trend was used in this study. The dynamic factor analysis was then applied to the stochastic trends in the gridded seasonal and annual temperature data in the contiguous United States region from 1900 to 2003. The results showed that the strong inter-decadal factor exits in the winter and summer season and it is associated mainly with the southeastern part of this region. After this inter-decadal signal was removed from the annual data, a strong nearly monotonic stochastic factor was found across this region. This factor was displayed as an increasing trend in the northern and western parts and as a decreasing trend in the southeastern parts of this region. The inter-decadal factor is likely to originate from natural forcings such as the north Atlantic oscillation. The cooling trend in the southeastern region may be due to the excessive sulfates in the air. The area-averaged monotonic stochastic factors still showed an increasing trend during the first half-twentieth century. Therefore, the warming in this region during the first part of the twentieth century may be attributed to both anthropogenically forced change and internal variations. The effects of natural forcings at the southeastern US regions in winter and summer seasons are crucial for simulating the temperature time series and for attributing the source of warming in the first part of the twentieth century in this region.

Chapter 5 analyzed the monthly southern Africa precipitation data from the United Kingdom Meteorological Office for the period of 1900-2005. The area integrated standardized precipitation index and empirical orthogonal functions of the gridded drought magnitudes were used to characterize the drought events and to establish their

spatial patterns. The EOFs revealed three leading modes of spatial and temporal variability of droughts in southern Africa. Between 1990 and 2005, the magnitude of droughts and rainfall deficits at the 12- and 24-month time scales increased considerably compared to the drought magnitudes at the 3- and 6-month time scales, showing that after 1990, meteorological and hydrological droughts became dominant. The January-March rainfall was found to be the most critical part of the rainy season. However, due to the agriculture practices in the region, the failure of rainfall in other months such as November and December caused crop failures and famines in the region. The ASPI is an effective and precise index for monitoring regional droughts and assessing drought severities in an integrated way and, hence, is a convenient decision-making tool for governments.

6.2 Future work

The work in this thesis can be extended in several directions. Improvements to the methodologies include the following.

The wavelet transform is an important tool for analyzing stochastic processes. The discrete wavelet transform has been used to estimate smooth nonstochastic trends in a long memory dependence process model (Craigmail et al., 2004). The non-decimated wavelet transform has been used to extract major variability components from solar and temperature data, and common characteristics were identified at the corresponding scales (Oh et al., 2003). The wavelet spectrum has been shown to be the characterization

function of stationary and long-memory processes (Li and Oh, 2002). A number of wavelet-based estimators for long-range dependent processes have been proposed in past studies (Jones et al., 1996). Therefore, wavelet transforms can help to identify structures in daily temperature data and to provide estimates of the stochastic characteristics. Various choices of mother wavelets and the form of the transformations, and the comparison of their results with those obtained by using the EMD method will strengthen the identification of stochastic properties in daily temperature data.

Dynamic factor analysis can be applied to large cross-sectional data. In this thesis, we applied it to the gridded temperature data. Further improvement of the analysis can be made by incorporating other data such as precipitation and wind-speed data. Generalized dynamic factor models can include the lags of non-stationary factors (Bai, 2004). This type of analysis would be more flexible than the static dynamic factor analysis we used in this thesis. To test whether an observed climate variable is the true factor, a comparison can be made by regressing it on the dynamic factors. A cointegration analysis can be carried out to examine the relationship between the dynamic factors and radioactive forcings to determine the source of climatic change.

Statistical analysis of the observed data is complementary to the climate model simulations. Improvements in methodology will contribute to our understanding of the climate variability in both the regional and global scales. The following are possible topics worth studying.

The stochastic properties of daily SAT data from stations from around the world can be analyzed. By comparing the different orders of stationarity of daily SAT data at different time scales among land stations, island stations, the stations at different latitudes, and urban stations, we could obtain information about the persistency in the temperature data related to the local climate systems.

The detection and attribution of climate change at the regional scale has attracted much attention since the release of the third Intergovernmental Panel on Climate Change in 2001. Despite the effects to improve model accuracy, estimates of the contribution of anthropogenic and natural forcings vary from model to model. Dynamical factor analysis can be carried out on the observed data over regions of interest to help identify the factors affecting the local climate.

The attribution of climate change to human and natural sources has been made by comparing the observed climate data with those from the model simulations. The relationship among the averaged SAT in the northern and southern hemisphere and the radioactive forcings of solar irradiance, greenhouse gases, and tropospheric sulfates has been tested by using the vector error correction model. This approach does not involve model simulations. This method could be extended by incorporating spatial dependence into the model. The spatial dependence may take the form of spatial autocorrelation. Space-time cointegration can also be applied if long observations are available.

In Chapter 5, the area integrated standardized precipitation index and empirical orthogonal functions of the gridded drought magnitudes were applied to the precipitation

in the southern Africa region. The same method can be applied to other regions such as the Alberta region where the recently developed Alberta daily gridded precipitation dataset is available for the period from January 1, 1901 to December 31, 2003 (Shen et al., 2001).

Bibliography

Bai, J., 2004: Estimating cross-section common stochastic trends in non-stationary panel data, *J. Econometrics*, **122**, 137-183.

Bai, J., and S. Ng, 2004: A PANIC attack on unit roots and cointegration, *Econometrica*, **72**, 1127-1177.

Bloomfield, P., and D. Nychka, 1992: Climate spectra and detecting climate change, *Clim. Change*, **21**, 1-16.

Boashash, B., 1992a: Estimating and interpreting the instantaneous frequency of a signal-Part 1: Fundamentals, *Proc. IEEE,* **80**, 520-538.

Boashash, B., 1992b: Estimating and interpreting the instantaneous frequency of a signal-Part 2: Algorithms and applications, *Proc. IEEE,* **80**, 539-568.

Campell, S.D., and F.X. Diebold, 2005: Weather forecasting for weather derivatives, *J. Amer. Statist. Assoc.*, **100,** 6-16.

Chen, Z., P.C. Ivanov, K. Hu, and S.E. Stanley, 2002: Effect of nonstationarities on detrended fluctuation analysis, *Phys. Rev. E.*, **65**, 041107.

Coughlin, K.T., and K.K. Tung, 2004: 11-year solar cycle in the lower stratosphere extracted by the Empirical Mode Decomposition method, *Adv. Space Res.*, **34**, 323-329.

Craigmail, P.F., P. Guttorp, and D.B. Percival, 2004: Trend assessment in a long memory dependence model using the discrete wavelet transform, *Environmetrics*, **15**, 313-335.

Durbin J, and S.J. Koopman, 2001: *Time series analysis by state space methods*, Oxford university press: Oxford.

Eichner, J.F., E. Koscielny-Bunde, A.Bunde, S. Havlin, and H.-J. Schellnhuber, 2003: Power-law persistence and trends in the atmosphere: A detailed study of long temperature records, *Phys. Rev. E.*, **68**, 046133.

Engle, R.F., 1982: Autoregressive conditional heteroscedasticity with estimates of the variance of United Kingdom inflation, Econometrica, **50**, 987-1006.

Engle, R.F., and C.W.J. Granger, 1987: Co-integration and Error correction: representation, estimation, and testing, *Econometrica,* **55**, 251-276.

Fanta, B., B.T. Zaake, and R.K. Kachroo, 2001: A study of the variability of the river flow of the southern Africa region, *Hydro. Sci.*, 46, 513-524.

Feldman, M., 1997: Non-linear free vibration identification via the Hilbert transform, *J. Sound and Vibration,* **208**, 475-489.

Flandrin, P., G.. Rilling, and P. Goncalves, 2004: Empirical Mode Decomposition as a Filter Bank, *IEEE Signal Process. Lett.*, **11**, 112-114.

Folland, C.K., Coauthors, 2001: Observed climate variability and change, *Climate Chang 2001: The Scientific Basis,* edited by J.T. Houghton et al., Cambridge University Press, pp99-181.

Fomby, T.B., and T.J. Vogelsang, 2002: The application of size-robust trend statistics to global warming temperature series, *J. Climate*, **15**, 117-123.

Gil-Alana, L.A., 2003: An application of fractional integration to a long temperature series, *Int. J. Climatol*, **23**, 1699-1710.

Gil-Alana, L.A., 2006: Nonstationary, long-memory and anti-persistence in several climatological time series data, *Environ. Model. Assess.*, **11**, 19-29.

Giorgi, F., et al., 2001: Regional clmate information-Evaluation and projections, *Climate Chang 2001: The Scientific Basis*, edited by J.T. Houghton et al., Cambridge University Press, pp583-638.

Gloersen, P., and N.E. Huang, 2003: Comparison of interannual intrinsic modes in hemispheric sea ice covers and other geophysical parameters, *IEEE Trans. Geosci. Remote Sens.*, **41**, 1062-1074.

Guttman, N.B., 1998: Comparing the Palmer drought index and the standardized precipitation index, *J. Amer. Water Resour. Assoc.*, **34**, 113-121.

Guttman, N.B., 1999: Accepting the standardized precipitation index: a calculation algorithm, *J. Amer. Water Resour. Assoc.*, **35**, 311-322.

Harvey, A.C., 1985: Trends and cycles in Macroeconomic time series, *J. Bus. and Econ. Stat*, **3**, 216-227.

Harvey, A.C., 1989: Forecasting, structual time series models and the Kalman filter, Cambridge University press: Cambridge.

Harvey, D.I., and T.C. Mills, 2003: Modelling trends in central England temperatures, *J. Forecast*, **22**, 35-47.

Heim, R.R. Jr., 2002: A review of twentieth-century drought indices used in the United States, *Bull. Amer. Meteor. Soc.*, **83**, 1149-1165.

Hosking, J.R.M., 1981: Fractional differencing, *Biometrika*, **68**, 165-176.

Hu, K., P.C. Ivanov, Z. Chen, P. Carpena, and H.E. Stanley, 2001: Effect of trends on detrended fluctuation analysis, *Phys. Rev. E,* **64**, 011114.

Huang, 2005: Introduction to the Hilbert-Huang transform and its related mathematical problems, *Hilbert-Huang transform and its applications*, edited by N.E. Huang, and S.S.P. Shen, World Scientific, Singapore, pp1-26.

Huang, N.E., Z. Shen, and S.R. Long, 1999: A new view of nonlinear water waves: the Hilbert spectrum, *Ann. Rev. Fluid Mech.*, **31**, 417-457.

Huang, N.E., Z. Shen, S.R. Long, M.C. Wu, H.H. Shih, Q. Zheng, N-C. Yen, C.C. Tung, and H.H. Liu, 1998: The empirical mode decomposition and the Hilbert spectrum for nonlinear and non-stationary time series analysis, *Proc. R. Soc. London Ser. A,* **454**, 903-995.

Huang, N.E., M.C. Wu, S.R. Long, S.S.P. Shen, N.H. Hsu, D. Xiong, W. Qu, P. Gloersen, and K.L. Fan, 2003: A confidence limit for the empirical mode decomposition and Hilbert spectral analysis, *Proc. R. Soc. London Ser. A,* **459**, 2317-2345.

Huang, N.E., M-L Wu, W. Qu, S.R. Long, and S.S.P. Shen, 2003: Applications of Hilbert-Huang transform to non-stationary financial time series analysis, *Appl. Stoch. Models Business Ind.*, **19**, 245 – 268.

Hulme, M., 1994: Validation of large-scale precipitation fields in general circulation models, *Global precipitations and climate change*, edited by Desbois, M and F. Desalmand, NATO ASI Series, Springer-verlag Press, Berlin: 387-406.

Hurrell, J.W., and H.V. Loon, 1997: decadal variations in climate associated with the north atlantic oscillation, *Clim. Change*, **36**, 301-326.

Jones, C.L., G.T.Lonergan, and D.E. Mainwaring, 1996: Wavelet packet computation of Hurst exponent, *J.Phys.A: Math.Gen.*, **29**, 2509-2527.

Kärner, O., 2002: On nonstationary and antipersistency in global temperature, *J. Geophys.Res.*, **107**, 1-11.

Kärner, O., 2005: Some examples of negative feedback in the Earth climate system, *Central European Journal of Physics*, **3**, 190-208.

Karoly, D.J., and K. Braganza, 2005: Attribution of recent temperature changes in the Australian region, *J. Climate*, 18, 457-464.

Karoly, D.J., K. Braganza, P.A. Stott, J.M Arblaster, G.A. Meehl, A.J .Broccoli, and K.W.Dixon, 2003: Detection of a human influence on North American climate, *Science,* **302**, 1200-1203.

Karoly, D.J., and Q. Wu, 2005: Detection of regional surface temperature trends, *J. Climate,* **18**, 4337-4343.

Kauffman, R.K., and D.I. Stern, 2002: Cointegration analysis of hemispheric temperature relations, *J. Geophys. Res.*, **107(D2)**, 4012. doi:10.1029/2000JD000174.

Király, A., and I.M. Jánosi, 2002: Stochastic modeling of daily temperature fluctuations, *Phys. Rev. E,* **65**, 051102.

Király, A., and I.M. Jánosi, 2005: Detrended fluction analysis of daily temperature records: Geographic dependence over Australia, *Metero. Atmos. Phys.*, **88**,119-128.

Knutson, T.R., T.L. Delworth, K.W. Dixon, I.M. Held, J. Lu, V. Ramaswamy, M.D. Schwarzkopf, G. Stenchikov, and R.J. Stouffer, 2006: Assessment of twentieth-century regional surface temperature trends using GFDL CM2 coupled models, *J. Climate,* **19**, 1624-1651.

Koopman, S.J., 1997: Exact initial Kalman filtering and smoothing for non-stationary time series models, *J. Am. Stat. Assoc.,* **92**, 1630-1638.

Lenten, L.J.A., and I.A. Moosa, 2003: An empirical investigation into long-term climate change in Australia, *Environ. Modell. Software*, **18**, 59-70.

Lewis, P.A.W., and B.K. Ray, 1997: Modeling long-range dependence, nonlinearity, and periodic phenomena in sea surface temperature using TSMARS, *J. Am. Stat. Assoc.,* **92,** 881-893.

Li, T.H., and H.S. Oh, 2002: Wavelet spectrum and its characterization property for random processes, *IEEE Trans. Inform. Theory,* **48**, 2922-2937.

Livezey, R.E., and T.M. Smith, 1999: Covariability if aspects of North American with global sea surface temperatures on interannual to interdecadal timescales, *J. Climate*, **12**, 289-302.

Loh, C-H, T-C. Wu, and N.E. Huang, 2001: Application of the Empirical Mode Decomposition-Hilbert Spectrum Method to Identify Near-Fault Ground-Motion Characteristics and Structural Responses, *Bull. Seismol. Soc. Am.,* **91**, 1339-1357.

Mckee, T.B., N.J. Doesken, and J. Kleist, 1993: The relationship of drought frequency and duration of time scales, In *Proceedings of the 8th Conference on Applied Climatology*, Anahielm, CA, *Amer. Meterol. Soc.*: Boston, MA: 179-184.

Mallat, S., 1998: A Wavelet Tour of Signal Processing, Academic Press, London, pp.91-110.

Maphosa, B., 1994: Lessons from the 1992 droughts in Zimbabwe: The quest for alternative food policies, *Nordic J. African Studies.,* **3**, 53-58

Marple, S.L., 1999: Computing the discrete-time analytic signal via FFT, *IEEE Trans. Signal Processing*, **47**, 2600-2603.

Mandelbrot, B.B., and J.W.V. Ness, 1968: Fractional Brownian motions, fractional noises and applications, *SIAM Review*, **10**, 422-437.

Mills, T.C., 2006: Modelling current trends in Northern Hemisphere temperatures, *Int. J. Climatol.,* **26,** 867-884.

Mitchell, J.F.B., and Coauthors, 2001: Detection of climate change and attribution of causes, *Climate Chang 2001: The Scientific Basis,* edited by J.T. Houghton et al., Cambridge University Press, pp697-738.

Mwale, D., T.Y. Gan, and S.S.P. Shen, 2004: A new analysis of the variability, teleconnectivity, and predictability of central southern Africa rainfall for the period

1950-97, *Int. J. Climatol.*, **24**, 1509-1530.

Negri, A F-I., 2002: Nonlinear statistical modeling of high frequency ground ozone data, *Evironmetrics*, **13**, 225-241.

North, G.R., and Q. Wu, 2005: Detecting climate signal using space-time EOFs, *J. Climate*, **14**, 1839-1863.

Nyblom, J., and A.C. Harvey, 2001: Tests against smooth stochastic trends, *J. Appl. Econom.*, **16**, 415-429.

Oh, H.S., C. Ammann, P.D. Naveau, D. Nychka, and B. Otto-Bliesner, 2003: Multi-resolution time series analysis applied to solar irradiance and climate reconstructions, *J.Atm. Solar-terr. Phys.*, **65**, 191-201.

Ostermeier, G.M., and J. M. Wallace, 2003: Trends in the North Atlantic Oscillation–Northern Hemisphere Annular Mode during the Twentieth Century, *J. Climate*, **16**,336-341.

Palmer, W.C., 1965: Meteorological drought, Research paper No. 45, U.S. Department of commerce Weather Bureau, Washington D. C.

Peng, C.-K., S. Havlin, H.E. Stanley, and A.L. Goldberger, 1995: Quantification of scaling exponents and crossover phenomena in nonstationary heartbeat time series, *Chaos*, **5**, 82-87.

Peterson, T.C., and R.S. Vose, 1997: An overview of the global historical climatology network temperature database, *Bull. Amer. Meteor. Soc.*, **78**, 2837-4179.

Rouault, M., and Y. Richard, 2005: Intensity and spatial extent of droughts in southern Africa, *Geophys. Res. Lett.* **32**, L15702, doi:10.1029/2005GL022436.

Schneider, T., and I. Held, 2001: Discriminants of twentieth-century changes in Earth surface temperatures, *J. Climate,* **14**, 249-254.

Seidel, D.J., and J.R. Lanzante, 2004: An assessment of three alternatives to linear trends for characterizing global atmospheric temperature changes, *J. Geophys. Res.*, **109**, 109, D14108, doi:10.1029/2003JD004414.

Shen, S.S.P., P. Dzikowski, G. Li, and D. Griffith, 2001: Interpolation of 1961–97 daily temperature and precipitation data onto Alberta polygons of ecodistrict and soil landscapes of Canada, *J. Appl. Meteor.*, **40**, 2162-2177.

Shen, S.S.P., T. Shu, N.E. Huang, Z. Wu, T.R. Karl, and D.R. Easterling, 2005: HHT analysis of the nonlinear and non-stationary annual cycle of daily surface air temperature data, *Hilbert-Huang Transform and Its Applications*, edited by N.E. Huang and S.S.P. Shen, World Scientific, Singapore, pp.187-209.

Shumway, R.H., and D.S. Stoffer, 2000: *Time series analysis*, Springer-Verlag, New York.

Sonmaze, F. K., A.U. Komuscu, A. Erkan, and E. Turgu, 2005: An analysis of the spatial and temporal dimensions of drought vulnerability in Turkey using the standardized precipitation index, *Natural Hazards*, **35**, 243-264.

Stern, D.I., and R.K. Kaufmann, 2000: Detecting a global warming in hemispheric temperature series: a structural time series analysis, *Clim. Change,* **47**, 411-438.

Stock, J.H., and M.W. Watson, 1988: Testing for common trends, *J. Am. Stat. Assoc.*, **83**, 1097-1107.

Stock, J.H., and M.W. Watson, 1999: Diffusion indexes, NBER Working Paper 6702.

Stock, J.H., and M.W.Watson, 2002: Forecasting using principal components from a large number of predictors, *J. Am. Sta. Assoc.*, **97**, 1167-1179.

Stott, P.A., 2003: Attribution of regional-scale temperature changes to anthropogenic and natural causes, *Geophys. Res. Lett.,* **30**, 1728. DOI: 10.1029/2003GL017324.

Stott, P.A., S.F.B. Tett, G.S. Jones, M.R. Allen, W.J. Ingram, and J.F.B. Mitchell, 2001: Attribution of twentieth century temperature change to natural and anthropogenic causes, *Clim. Change,* **17**, 1-21.

Mills, T.C., 2006: Modelling current trends in northern hemisphere temperatures, *Int. J. Climatol.*, **26**, 867-884.

Talker, P., and P.O. Weber, 2000: Power spectrum and detrended fluctuation analysis: Application to daily temperatures, *Phys. Rev. E,* **62,** 150-160.

Thom, H.C.S. 1958: A note on the gamma distribution, *Mon. Wea. Rev.*, **86**, 117-122.

Trenberth, K.E., 1997: The definition of El Niño, *Bull. Amer. Meteor. Soc.*, **78**, 2771-2777.

Wang, B., and Y. Wang, 1996: Temporal structure of the Southern Oscillation as revealed by waveform and wavelet analysis, *J. Clim*ate, **9**, 1586-1598.

Wang, B., 1994: On the annual cycle in the tropical eastern-central Pacific, *J. Climate*, **7**, 1926-1942.

Wood, A.T.A., and G. Chan, 1994: Simulation of Stationary Gaussian Processes in $[0,1]^d$, *J. Comp. Graph. Stat.*, **3**, 409-432.

Wu, L S-Y, J.S. Pai, and J.R.M. Hosking, 1996: An algorithm for estimating parameters of state-space models, *Stat. Prob. Lett.*, **28**, 99-106.

Wu, Z., and N.E. Huang, 2004: A study of the characteristics of white noise using the Empirical Mode Decomposition Method, *Proc. R. Soc. London Ser. A,* **460**, 1597-1611.

Xu, Y.L., M., ASCE, and J. Chen, 2004: Characterizing nonstationary wind speed using Empirical Mode Decomposition, *J. Struct. Engrg.*, **130**, 912-920.

Yin, H., 2006: Statistical data analysis of Alberta agroclimate and global surface air temperature, Ph.D. Thesis, University of Alberta.

Yu, S., V.K., Saxena, and Z. Zhao, 2001: A comparison of signals of regional aerosol-induced forcing in eastern China and the southeastern United States, *Geophys.l Res. Letts.*, **28**, 713–716, 2001

Zhen, X, and R.E. Basher, 1999: Structural time series models and trend detection in global and regional temperature series, *J. Climate*, **12**, 2347-2358.

Zuur, A.F., and G.J. Pierce, 2004: Common trends in northeast Atlantic squid time series, *J. Sea Res.*, **52**, 57-72.

Zwiers, F.W., and X. Zhang, 2003: Toward regional-scale climate change detection, *J. Climate*, **16**,793-797.